

## AN ABSTRACT OF THE THESIS OF

Silvino A. Balderrama Prieto for the degree of Master of Science in Nuclear Engineering presented on August 16, 2019.

Title: Computational Fluid Dynamics Modeling of the Density Evolution Inside of the Helium-3 Enhanced Negative Reactivity Insertion (HENRI) System.

Abstract approved: \_\_\_\_\_

Wade R. Marcum

The testing of nuclear fuel under reactivity-initiated accident (RIA) conditions is paramount for the better understanding of the fuel's behavior during this transient accident events. The Transient Reactor Test (TREAT) facility is a nuclear reactor that will be capable of recreating the thermal-hydraulic and neutronic boundary conditions representative of RIA events for light water reactors (LWRs). However, one of the engineering challenges to perform such fuel tests is to increase the energy deposition on the fuel sample by reducing the current TREAT's pulse width of 89 down to 40 ms. Idaho National Laboratory (INL) proposed to clip the pulse by inserting helium-3, a strong neutron absorber, into an annular control rod using a gas injection system known as the Helium-3 Enhanced Negative Reactivity (HENRI) facility.

The purpose of this study is to pave the path towards the development of a computational fluid dynamics (CFD) model capable of confidently simulate the density evolution inside of the HENRI facility using the commercial CFD software STAR-CCM+. The development of a CFD model is essential since existing instrumentation is unable to obtain a direct measurement of the helium density, and indirect methods are unable to measure it with high accuracy. For better analysis of the system's performance inside of the TREAT facility, the CFD model will be coupled with a

reactor physics modeling software so a more representative analysis of the transient pulse of the TREAT can be obtained.

©Copyright by Silvino A. Balderrama Prieto

August 16, 2019

All Rights Reserved

Computational Fluid Dynamics Modeling of the Density Evolution Inside of the  
Helium-3 Enhanced Negative Reactivity Insertion (HENRI) System

by

Silvino A. Balderrama Prieto

A THESIS

Submitted to

Oregon State University

in partial fulfillment of  
the requirements for the  
degree of

Master of Science

Presented: August 16, 2019

Commencement: June 2020

Master of Science thesis of Silvino A. Balderrama Prieto presented on August 16, 2019.

APPROVED:

---

Major Professor, representing Nuclear Engineering

---

Head of the School of Nuclear Science and Engineering

---

Dean of the Graduate School

I understand that my thesis will become part of the permanent collection of Oregon State University libraries. My signature below authorizes release of my thesis to any reader upon request.

---

Silvino A. Balderrama Prieto, Author

## ACKNOWLEDGEMENTS

I would first like to express my deepest appreciation to my faculty advisor, Dr. Wade R. Marcum, for the guidance he provided me through the 2 years I worked for him. It was an honor to be part of his research group, and I would not be where I am today without his help.

I am particularly grateful for the constant support I received from Dr. Guillaume Mignot, who was always available to help me in every aspect of this project. Additionally, I would like to thank my committee members, the Radiation Center staff, and various people from my research group who, in one way or another, played a crucial role in my research experience here at Oregon State University.

Finally, I would like to acknowledge with gratitude my parents, Silvino M. Balderrama and Tomasa Prieto, for helping me to reach my goals and dreams. I am also very thankful for the devotion and the unwavering support I received from Marwah Alzabidi.

## TABLE OF CONTENTS

<u>Contents</u>	<u>Page</u>
1 INTRODUCTION .....	1
1.1 Motivation.....	3
1.2 Objective .....	4
1.3 Document Overview .....	5
2 THEORETICAL BACKGROUND.....	6
2.1 Compressible Flow.....	7
2.2 Principles Behind Shock Tubes.....	8
2.3 Existential Helium-3 Control Rod System.....	12
2.4 STAR-CCM+ Governing Equations .....	16
2.5 Boundary Layer and Wall Treatment.....	18
2.6 Turbulence Models.....	22
2.7 CFD simulation of the CABRI transient rods .....	26
3 FACILITY DESCRIPTION .....	29
3.1 Overview .....	29
3.2 Design.....	32
3.3 Instrumentation.....	38
3.4 Matrix Test .....	39
4 CFD MODELING AND METHODOLOGY .....	41
4.1 Geometry Development .....	43
4.2 Mesh Generation and Refinement Process.....	46
4.2.1 Grid Independence Study.....	52

4.3	Initial Conditions.....	55
4.4	Boundary Conditions.....	57
4.5	Physics Models.....	62
4.5.1	Flow Solver.....	62
4.5.2	Time Solver.....	64
4.5.3	Material Selection .....	65
4.5.4	Turbulence Model.....	66
4.6	Stopping Criteria .....	66
4.7	Post processing Setup.....	67
5	EXPERIMENTAL BENCHMARK .....	68
6	RESULTS AND DISCUSSION .....	69
6.1	Verification: Shock Tube Analysis .....	70
6.2	Grid Independence Study .....	75
6.3	Validation: Experimental Benchmark.....	79
6.4	Parametric Study: Annular Test Section .....	97
6.4.1	Geometry Analysis: Intermediate Section .....	98
6.4.2	Driver Tank Pressure Analysis .....	100
7	CONCLUSION.....	110
7.1	Observations.....	110
7.2	Relevance of Work.....	112
7.3	Assumptions and Limitations.....	113
7.4	Future Work .....	113
8	REFERENCES .....	114
9	APPENDIX A: Out-of-pile HENRI test facility drawings .....	118

10 APPENDIX B: Out-of-pile HENRI test facility matrix test.....	123
11 APPENDIX C: GCI MATLAB Code.....	124

## LIST OF FIGURES

<u>Figure</u>	<u>Page</u>
Figure 1. Comparison of contemporary nuclear reactor transient pulses [5].....	3
Figure 2. Initial pressure profile in a shock tube [7].....	9
Figure 3. Pressure profile in a shock tube after time, $\Delta t$ [7]. .....	10
Figure 4. Schematic of CABRI helium-3 transient rod system [11].....	14
Figure 5. CABRI power transient [11]. .....	15
Figure 6. Velocity distribution for laminar and turbulent flows [15]. .....	18
Figure 7. Law of wall for horizontal velocity near a solid surface [13]. .....	20
Figure 8. K-omega Menter SST blending function. ....	25
Figure 9. Comparison of CFD vs experimental data [19]......	29
Figure 10. TREAT's assembly cross-sectional view [20]. .....	32
Figure 11 . HENRI test facility driver tank.....	33
Figure 12. Out-of-pile HENRI test facility intermediate section [20]. .....	34
Figure 13. Schematic of shock wave interaction with extension (right) and without extension (left). .....	36
Figure 14. Out-of-pile HENRI test facility test and extension sections [20].....	37
Figure 16. Pressure and temperature sensors location [20]. .....	39
Figure 17. Simplified CFD methodology. .....	43
Figure 18. Schematic of a shock tube. .....	44

Figure 19. 3D-CAD and rendering of the out-of-pile HENRI test facility.....	45
Figure 20. 3D-CAD of annular test section. ....	45
Figure 21. Mesh refinement of out-of-pile HENRI test facility 3D CAD.....	48
Figure 22. Schematic of prism layer.....	49
Figure 23. Example of a good and bad face validity [13]......	51
Figure 24. Example of good and bad cells [13]......	52
Figure 25. Temperature distribution across walls.....	59
Figure 26. Temperature distribution for different Biot numbers in transient events [24]. .....	60
Figure 27. Biot number from cylindrical test section of the out-of-pile HENRI test facility. ....	61
Figure 28. Probe points in shock tube.....	67
Figure 29. Position of probe points in test facility with cylindrical test section.....	68
Figure 30. Position of probe points in test facility with annular test section.....	68
Figure 31. x-t diagram of shock tube with initial pressures of 1000 and 0.01 psi.....	71
Figure 32. x-t diagram of shock tube (1000/0.1 psi).....	72
Figure 33. x-t diagram of shock tube with initial pressures of 1000 and 0.25 psi.....	72
Figure 34. x-t diagram of shock tube with initial pressures of 1000 and 0.5 psi.....	73
Figure 35. x-t diagram of shock tube with initial pressures of 1000 and 1 psi.....	73
Figure 36. Pressure and temperature recorded in the test section at time 1 ms. using 3 different grid sizes.....	77

Figure 37. Extrapolated solutions for the pressure (left) and temperature (right) of the annular test section.....	78
Figure 38. Pressure evolution for probe point TS00 using different low pressures. ..	80
Figure 39. Pressure evolution for probe point TS01 using different low pressures. ..	81
Figure 40. Pressure evolution for probe point TS02 using different low pressures. ..	81
Figure 41. Pressure evolution for probe point TS03 using different low pressures. ..	82
Figure 42. Pressure evolution for probe point TS05 using different low pressures. ..	82
Figure 43. Pressure evolution inside of the cylindrical test section of the experiment and CFD model using an intermediate section tube diameter of 0.75". .....	84
Figure 44. Pressure evolution at the top (TS4) and bottom (TS1) of the cylindrical test section of the out-of-pile HENRI test facility using an intermediate section tube diameter of 0.75".....	85
Figure 45. Comparison of measured vs. calculated maximum pressure for the out-of-pile HENRI test facility with intermediate section tube diameter of 0.75". .....	86
Figure 46. Comparison of measured vs. calculated time to maximum pressure for the out-of-pile HENRI test facility with intermediate section tube diameter of 0.75"....	86
Figure 47. Pressure evolution inside of the driver tank of the experiment and CFD model using an intermediate section tube diameter of 0.75".....	87
Figure 48. Temperature evolution inside of the cylindrical test section obtained through the HENRI test facility using an intermediate section tube diameter of 0.75" .....	89
Figure 49. Temperature evolution inside of the cylindrical test section obtained through the HENRI test facility using an intermediate section tube diameter of 0.75" .....	89
Figure 50. Pressure evolution inside of the cylindrical test section of the experiment and CFD data using an intermediate section tube diameter of 1".....	91

Figure 51. Pressure evolution at the top (TS4) and bottom (TS1) of the cylindrical test section of the out-of-pile HENRI test facility using an intermediate section tube diameter of 1".....	92
Figure 52. Comparison of pressure evolution inside of the driver tank between experimental and CFD data using an intermediate section tube diameter of 1".....	93
Figure 53. Temperature evolution inside of the cylindrical test section obtained through the HENRI test facility using an intermediate section tube diameter of 1".....	94
Figure 54. Temperature evolution inside of the cylindrical test section obtained through the HENRI test facility using an intermediate section tube diameter of 1".....	94
Figure 55. Comparison of measured vs. calculated maximum pressure for the out-of-pile HENRI test facility with intermediate section tube diameter of 1".....	95
Figure 56. Comparison of measured vs. calculated time to maximum pressure for the out-of-pile HENRI test facility with intermediate section tube diameter of 1".....	96
Figure 57. Pressure evolution of the out-of-pile HENRI test facility using different tube sizes for the intermediate section.....	99
Figure 58. Density evolution inside of the cylindrical test section for the out-of-pile HENRI test facility with different intermediate tube sizes.....	100
Figure 59. Calculated pressure evolution within annular test section. ....	102
Figure 60. Calculated temperature evolution within annular test section.....	103
Figure 61. Normalized pressure evolution of the annular test section for the different driver tank pressure scenarios.....	104
Figure 62. Depressurization of the driver tank at different initial pressures. ....	105
Figure 63. Temperature evolution along the annular test section with different driver tank pressures.....	106

Figure 64. Calculated density evolution within the annular test section. .... 107

Figure 65. Overall density evolution along annular test section for different initial pressures..... 108

## LIST OF TABLES

<u>Table</u>	<u>Page</u>
Table 1. Wall treatment recommendations retrieved from reference [13].....	21
Table 2. Closure coefficients for k-omega Menter SST [18].....	26
Table 3. CABRI's CFD model setup .....	28
Table 4. Atomic and molecular density of helium-3. ....	31
Table 5. Rupture disk description .....	35
Table 6. Cell-type options for 2D simulations.....	47
Table 7. Description of prism layer setting options.....	48
Table 8. Average $y^+$ parameters.....	50
Table 9 . Initial pressure and temperature conditions. ....	56
Table 10. Wall physics conditions. ....	58
Table 11. Average pressure, temperature and velocity of incident shock waves. ....	74
Table 12. Statistics for coarse, medium, and fine meshes. ....	76
Table 13. GCI pressure results from grid independence study.....	78
Table 14. GCI temperature results from grid independence study .....	79
Table 15. Initial conditions for three simulations used for the low-pressure analysis.	80
Table 16. Initial and boundary conditions of the of the parametric study done on the HENRI facility with different tube diameters for the intermediate section.....	98

# **Computational Fluid Dynamics Modeling of the Density Evolution Inside of the Helium-3 Enhanced Negative Reactivity Insertion (HENRI) System**

## **1 INTRODUCTION**

Reactivity Initiated Accidents (RIA) are scenarios where a nuclear reactor experiences a sudden increase of fission rate and reactor power that leads to possible failure of fuel rods through cladding breach. The failure of fuel rods often results in the release of fragmented fuel directly into the coolant, which can contribute to the abrupt increase of water steam and pressure pulses. These undesired behaviors can cause damages to the reactor vessel, adjacent assemblies, and components located in the primary loop. Because of this, the comprehensive understanding of nuclear fuel's performance under RIA conditions are paramount in ensuring the safe operations of nuclear power plants during normal and off-normal conditions.

While there presently exists a relatively thorough database of empirical evidence to support the currently deployed nuclear fuel—uranium dioxide fuel—technology within the United States, it is necessary to further understand the response of prototypical and currently deployed nuclear fuel concepts under RIA conditions prior to their use in nuclear power plants. This need is presently being fulfilled at Idaho National Laboratory (INL) which operates the TREAT facility. The TREAT facility is a nuclear reactor located at the Materials and Fuels Complex west of Idaho Falls, Idaho. This facility's main purpose is to provide representative nuclear boundary conditions for fuel concepts that would be experienced in a nuclear reactor under transient conditions. It reached criticality in 1959. Throughout its 35 years of operation, it went through several changes and upgrades until 1994 [1]. The reactor was placed in standby in 1994; however, in November 2017 the TREAT reached criticality again due to the Department of Energy's request to restore operations in this facility. The first testing campaign following the reopening of this facility is focused on the support of the

Accident Tolerant Fuel (ATF) program. The emphasis on the ATF program arose after the incident that took place at the Japanese Fukushima Daiichi plant in 2011 [2] [1]. Some of the tests that are envisioned to be performed are the exposure of nuclear fuels in environments analogous to RIA accident scenarios. The TREAT facility has the capability to perform power bursts which can mimic a RIA event in light water reactors; however, the duration of these power bursts that the TREAT is presently capable of producing are longer than desired. If the RIA-type pulse in the TREAT facility has a long duration, it will exceed its maximum allowed energy deposition threshold, which is 2500 MJ. On the contrary, a short power excursion without exceeding its energy deposition threshold, the maximum energy deposited into the experiment is insufficient to meet the desired absorbed enthalpy goals needed. In order to reach higher energy peaks, a smaller transient excursion pulse width with a higher maximum power has to be achieved.

Currently, the pulse generated by the TREAT has a Full-Width at Half Maximum (FWHM) of 89 milliseconds [3], and it is desired to reduce this figure of merit to 40 milliseconds. Presently, the pulses of the TREAT are achieved through control rod scram or natural reactivity feedback, also known as temperature-limited transient, as the primary mechanism for driving the transient's duration. Alternatively, the inclusion of additional mechanical devices that synchronize with the pulse could be implemented to shorten or ‘clip’ the pulse or reduce its power faster after initiation to reach the desired FWHM. There are several mechanical concepts that have been proposed and are presently implemented on similar reactors throughout the world.

The sections covered in this chapter consist of providing more in-depth information regarding the motivation behind the development of a gas injection system and a CFD model of the system in support of the shortening of the pulse, the objectives that need to be achieved in order to develop the CFD model of the system, and an overview of this document is provided at the end of this chapter.

## 1.1 Motivation

Idaho National Laboratory identified that the pulse of the TREAT may be shortened by implementing a gas injection system to the reactor core, where helium-3 gas may be used as the absorbing medium to ‘clip’ the pulse. Helium-3 has been identified as a potential candidate for the enhancement of negative reactivity due to its high neutron absorption cross section. If this inert gas is injected sufficiently fast, an insertion of 5% negative reactivity can be achieved, leading ultimately to the desired power and pulse width. Preliminary calculations performed by INL, using the multi-purpose Monte Carlo N-Particle (MCNP) code, has shown that the relative power of the TREAT’s pulse can reach a higher power with a shorter FWHM [4]. Figure 1 compares the pulse FWHM of different contemporary reactors including the TREAT’s pulse clipped through the natural reactivity feedback of the reactor, using control rods and helium-3.

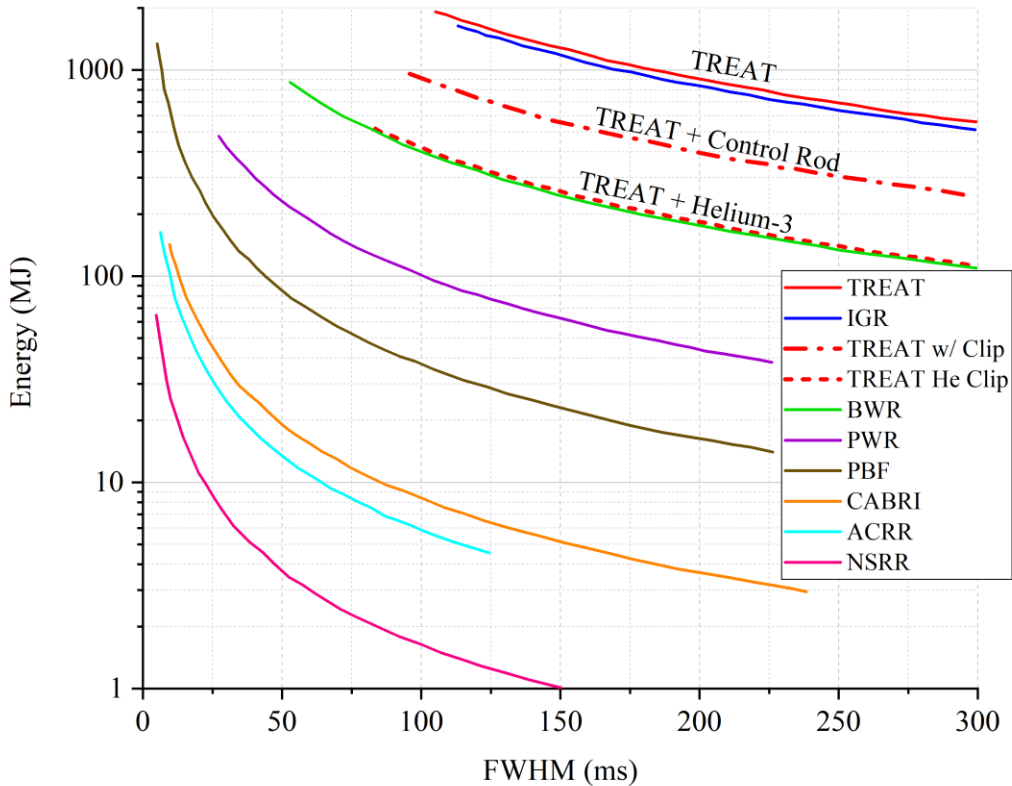


Figure 1. Comparison of contemporary nuclear reactor transient pulses [5].

From Figure 1, the pulse width of the TREAT facility is further reduced to near boiling water reactor (BWR) conditions if helium-3 is used to clip the pulse.

Oregon State University (OSU) was tasked to design and build a gas injection system, known as the out-of-pile Helium-3 Enhanced Negative Reactivity Insertion or HENRI test facility, with the ultimate goal of assessing the feasibility, repeatability and control of the system. The tests performed in HENRI consisted of evaluating the initial and boundary conditions, and the geometry of the system. Ultimately, these tests provided the information necessary to delimit the operating conditions of the system by identifying the optimal conditions to insert the necessary amount of helium within the desired timeframe.

The motivation behind this work was to develop a computational fluid dynamics (CFD) model capable of confidently characterizing the gas behavior inside of the HENRI facility through the use of a CFD simulation. The development of a CFD model is essential since it can corroborate the findings identified in the experimental data obtained from the test facility developed at OSU, and it can better capture the density evolution inside of the system than measuring the pressure and temperature to indirectly calculate the density using the ideal gas law equation. It is anticipated to couple the CFD model with a reactor physics model so the insertion of negative reactivity due to helium-3 in the TREAT can be better simulated. The information presented in this document will pave the path towards the development of a CFD model for the gas injection system for the TREAT reactor.

## 1.2 Objective

For better characterization of the insertion of negative reactivity in the TREAT reactor due to helium-3, a CFD model of the HENRI system is needed. Thus, the objective of this study is to develop a CFD model that can simulate the spatial and temporal density evolution inside of the HENRI system with high confidence. This objective is accomplished by performing the following tasks:

- obtain relevant information regarding past research done on CFD modeling of supersonic flows and shock tubes,
- develop a CFD model of a shock tube and compare its results against analytical results to verify the differential equations are being solved properly using the chosen numerical solver settings, and perform an assessment of whether or not STAR-CCM+ is capable of confidently characterizing the gas dynamics of the HENRI system,
- perform a grid independence study to quantify the numerical error introduced by the mesh,
- develop a CFD model of the out-of-pile HENRI test facility with a cylindrical test section and benchmark it using experimental data to quantify the model's capability to recreate real-world phenomena, and
- develop a CFD model of the HENRI facility with an annular test section to assess whether or not the HENRI system is able to reach the desired atomic density level within the timeframe of interest.

### 1.3 Document Overview

The development and completion of this document was achieved by following a systematic process which aligns with the organization of this document. The following chapters of this document begin by providing a theoretical background section, where the physics that surround the phenomena of supersonic flows in closed systems are reviewed in greater detail. This survey of literature continues by providing information about the principles behind shock tubes, an overview of the governing equations employed in the software STAR-CCM+, and concepts that help to better understand boundary layers and wall treatment. This section concludes with an overview of past CFD modeling of systems similar to HENRI. Following the theoretical background, a description of the out-of-pile HENRI test facility is provided, where a description of the equipment and instrumentation used to perform experimental work is provided.

The section that proceeds after the facility description focuses entirely on the methodology followed for the development of the CFD models used in this study. This

section explores in greater detail the geometry, mesh, physics models, initial and boundary conditions, stopping criteria, and the post-processing setup used for the CFD models. Thereafter, the section that follows provides information about the validation or benchmark process, which is employed to determine the degree to which the CFD model is capable of recreating real-world phenomena. This process is based on the procedure provided in ASME V&V 20-2009 [6].

The last sections of this document showcase the results, conclusion, and future work of this study. The results obtained from the verification, validation, and parametric study done on the shock tube, out-of-pile HENRI test facility with cylindrical test section, and the HENRI facility with annular test section are presented along with an interpretation of the results. Then, a conclusion or summary section is included at the end of this document where it mentions the results obtained from this study, future work that needs to be done after the completion of this study, limitations encountered through this study, suggestions about what could have been improved in this study, and recommendations for the HENRI system design.

## 2 THEORETICAL BACKGROUND

The sections covered in this chapter are meant to support the assumptions and decisions made towards the development of the CFD model. The first section consists of the theoretical background behind compressible flows in order to have a better understanding of how the relative volume of a fluid changes as a result of a pressure change. The second section of this chapter covers the basic principles behind shock tubes since an analytical solution can be developed and compared against a CFD model in order to verify if the physics models are the appropriate ones to solve this type of transient problem, and determine if the simulation is able to solve the differential equations properly. In addition, some sections cover crucial information regarding an existent helium-3 gas system used for the control of reactivity of a nuclear reactor and the CFD model developed for the simulation of the gas dynamics of the system. Further

sections of this chapter are meant to provide a better understanding of the physics and meshing models integrated in STAR-CCM+.

## 2.1 Compressible Flow

Compressibility is an important factor that determines the relative change of a fluid's volume as a result of a pressure change. At some degree, all existent fluids are compressible. This means that the density of a fluid cannot be considered constant, but for some fluids it can be assumed to be constant since the change of density is considerably small [7]. Let's consider a fluid with volume,  $V$ , and the pressure around this volume is  $P$ . If the pressure around it is increased by an infinitesimal amount,  $dP$ , the result of it would be the change of volume of the fluid. Based on this, the compressibility of this fluid,  $\tau$ , can be described using the following equation:

$$\tau = -\frac{1}{V} \frac{dV}{dP}. \quad (1)$$

It is important to note that the right hand side of Equation (1) has a negative sign in front of it because as the pressure is increased, the decrease of volume shall be represented in a negative quantity [7]. Equation (1) can be rewritten in terms of density by using the following relationship:

$$\rho = \frac{1}{v}, \quad (2)$$

where  $v$  represents the specific volume. By combining Equations (1) and (2), it yields the following:

$$\tau = \frac{1}{\rho} \frac{d\rho}{dP}, \quad (3)$$

and by rewriting Equation (3), it yields,

$$d\rho = \rho \tau dP. \quad (4)$$

The equation presented above shows the relationship between pressure, density and compressibility. For liquids, the compressibility term is considerably smaller compared to gases. For instance, the compressibility of water at 1 atmosphere is  $5 \times 10^{-10} \text{ m}^2 / \text{N}$ , whereas the compressibility of air at the same pressure, is considerably greater,  $10^{-5} \text{ m}^2 / \text{N}$  [7] [8]. If the density of water and air were to be calculated after the surrounding pressure is increased, the density of water will change a little bit. However, the density of air will change significantly due to its large compressibility value.

For the purpose of this study, the fluid of interest, helium-3, is expected to have kinetic energy during the timeframe of interest. When a fluid is in motion, changes of pressure are present. As stated earlier, when a fluid with small compressibility (e.g., water) is subjected to a change of pressure, the density of the fluid does not change considerably. Therefore, a fluid with a relatively constant density that is in motion is considered to be incompressible. On the other hand, a fluid that has large compressibility (e.g., air) and is subjected to a pressure change, its density could change considerably. Thus, a fluid with non-constant density that is in motion is considered to be compressible. Based on this, the compressibility of a fluid shall be studied and taken into account since it can have substantial influence on the density of the fluid. Special attention shall be given to gases in systems that involve large pressure changes, such as the HENRI system, since their compressibility is larger, and the density of the gas can change drastically.

## 2.2 Principles Behind Shock Tubes

Shock tubes are devices that have the ability to create shock waves, caused by a pressure or density discontinuity on a fluid due to molecular collision [7], with preselected initial conditions. These devices are widely used in many research areas, including but not limited to aerodynamics, plasma physics investigations to explore shock wave structures, and chemical reaction analysis. An example of a shock tube is

provided in Figure 2, where a constant-area tube with both ends enclosed is divided into two sections. On the left side of the tube is filled with a gas at high pressure,  $P_4$ , and the right side of the tube is filled with a gas but at a considerably lower pressure,  $P_1$ . These two sections are divided by a diaphragm/rupture disk.

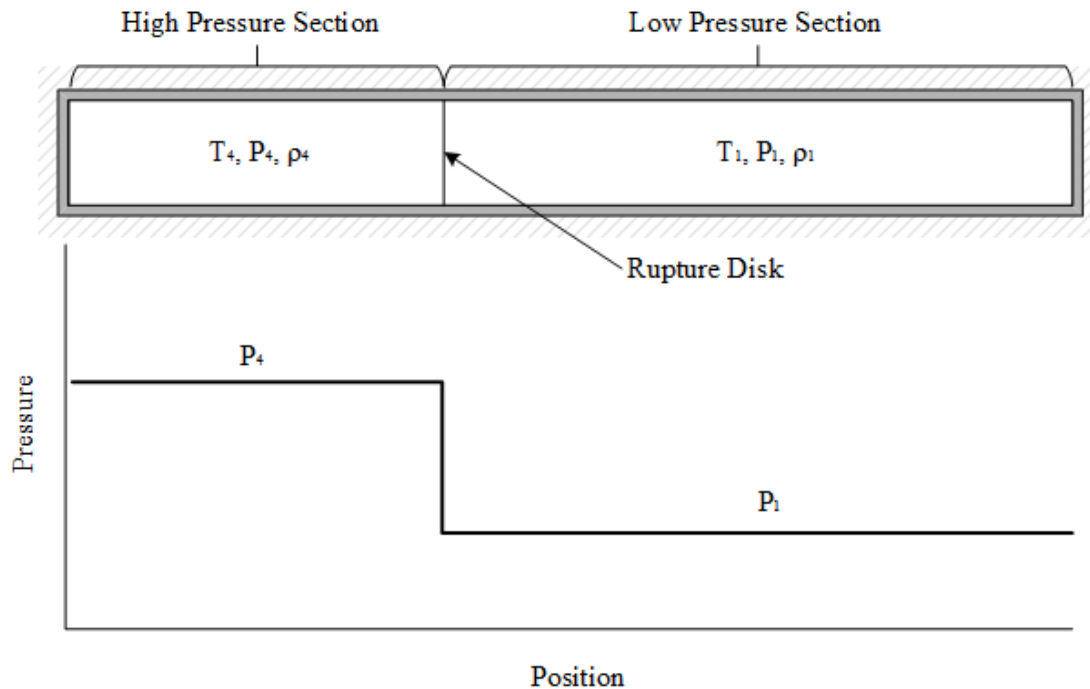


Figure 2. Initial pressure profile in a shock tube [7].

When the rupture disk bursts, a large pressure and density discontinuity is created in the shock tube. Thereafter, gas molecules from the high-pressure section move towards the low-pressure section by colliding. The collision of molecules results in a pressure wave also known as normal shock wave, with velocity  $v_s$ , moving to the right side as shown in Figure 3. On the left side of the shock tube, a different phenomenon takes place, an expansion wave, which is moving towards the left end side with velocity  $v_e$ .

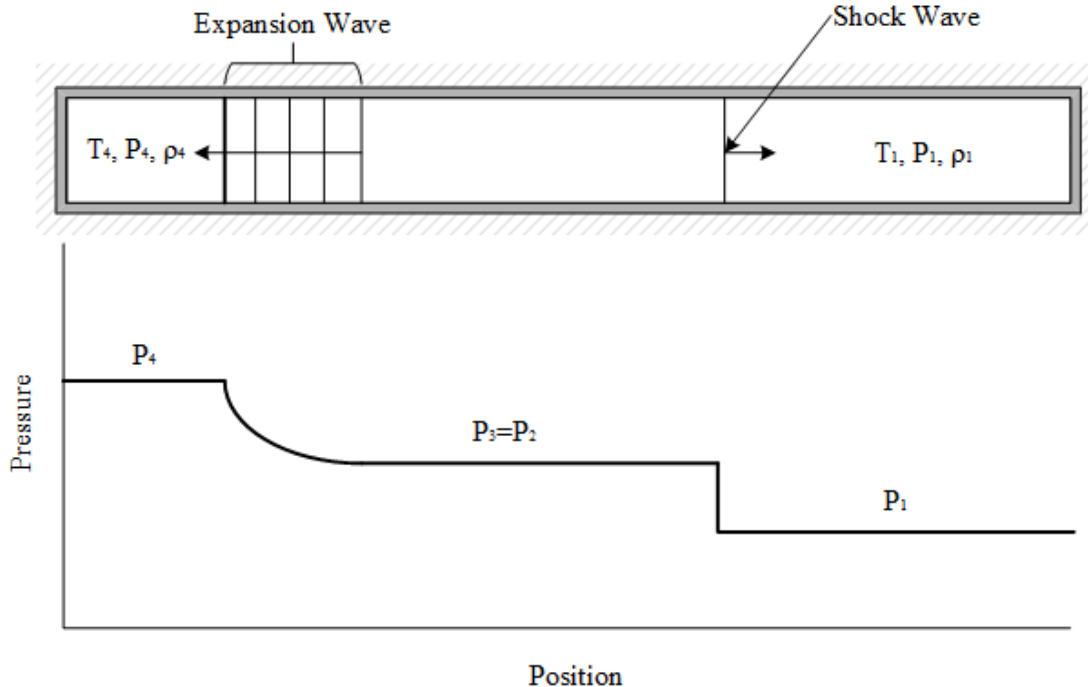


Figure 3. Pressure profile in a shock tube after time,  $\Delta t$  [7].

Even though the pressure gradient across the shock wave after a time,  $\Delta t$ , is not as large as it was at the beginning, the pressure gradient between regions 1 and 2/3 after  $\Delta t$  is still considerably large enough to create a shock wave. It is estimated that the mean free path (thickness) of a shock wave is in the order of magnitude of  $10^{-5}$  cm [9].

The pressure, temperature, and density profile along the shock tube can be obtained analytically if the initial conditions of the shock tube are known. The shock wave strength or pressure ratio,  $P_2/P_1$ , across the wave is calculated using the following relationship,

$$\frac{P_4}{P_1} = \frac{P_2}{P_1} \left[ 1 - \frac{(\gamma_4 - 1) \left( \frac{a_1}{a_4} \right) \left( \frac{P_2}{P_1} - 1 \right)}{\sqrt{2\gamma_1 \left\{ 2\gamma_1 + (\gamma_1 - 1) \left[ \left( \frac{P_2}{P_1} \right) - 1 \right] \right\}}} \right]^{\frac{-2\gamma_4}{\gamma_4 - 1}}, \quad (5)$$

where  $a_1$  and  $a_4$  represent the speed of sound in the high- and low-pressure sections,  $P_1$  and  $P_4$  represent the high and low pressures,  $\gamma_1$  and  $\gamma_4$  are the heat capacity ratios at the high- and low-pressure sections, respectively. If the gas on both sides of the rupture disk is the same, then:

$$\gamma_1 = \gamma_4 = \gamma \quad (6)$$

By knowing the pressure ratio across the shock wave, it is then possible to calculate the temperature, density, and the velocity of the shock wave. Through algebraic manipulation covered in reference [4], the temperature ratio across the shock wave is derived into the following form,

$$\frac{T_2}{T_1} = \frac{P_2}{P_1} \left( \frac{\frac{\gamma+1}{\gamma-1} + \frac{P_2}{P_1}}{1 + \frac{\gamma+1}{\gamma-1} \frac{P_2}{P_1}} \right), \quad (7)$$

the density across the shock wave is obtained from the following relationship,

$$\frac{\rho_2}{\rho_1} = \frac{1 + \frac{\gamma+1}{\gamma-1} \left( \frac{P_2}{P_1} \right)}{\frac{\gamma+1}{\gamma-1} + \frac{P_2}{P_1}}, \quad (8)$$

and the velocity of the shock wave is calculated using the following equation,

$$w = a_1 \sqrt{\frac{\gamma+1}{2\gamma} \left( \frac{P_2}{P_1} - 1 \right) + 1}. \quad (9)$$

In addition to the relationships shown above, the mass-motion or contact surface velocity can be calculated using the following equation,

$$u_p = \frac{a_1}{\gamma} \left( \frac{P_2}{P_1} - 1 \right) \left( \frac{\frac{2\gamma}{\gamma+1}}{\frac{P_2}{P_1} + \frac{\gamma-1}{\gamma+1}} \right)^{\frac{1}{2}}. \quad (10)$$

When the shock wave reaches the end of the shock tube, the collision on a solid surface normal to the shock wave trajectory makes it to bounce back or reflect the wave to an opposite direction, but the velocity of the reflected wave differs from the incident shock wave. In order to calculate the velocity of the reflected wave, the following relationship is used,

$$w_R = M_R a_2 - u_p. \quad (11)$$

Here,  $w_R$  represents the velocity of the reflected wave,  $M_R$  is the Mach number of the reflected wave, and  $a_2$  is the speed of sound in region 2 of the shock tube. The equation that solves for the Mach number of the reflected wave is shown below,

$$\frac{M_R}{M_R^2 - 1} = \frac{M_s}{M_s^2 - 1} \sqrt{1 + \frac{2(\gamma-1)}{(\gamma+1)^2} (M_s^2 - 1) \left( \gamma + \frac{1}{M_s^2} \right)}, \quad (12)$$

where  $M_s$  is the Mach number of the incident shock wave. By knowing the initial conditions of the shock tube and implementing the equations shown above, it is possible to develop analytical solutions, which can be further used for verification of the CFD model developed in this study.

### 2.3 Existence Helium-3 Control Rod System

The use of helium-3 for power bursts in nuclear research reactors is not a novel technique. In fact, France has a 25 MW reactor, located in Cadarache, known as the CABRI reactor. This facility is an experimental pulse reactor whose primary purpose

is to perform tests on nuclear fuels under RIA conditions [10] [11] [12]. Further modifications to the reactor allowed it to perform experiments that mimic loss of coolant accidents under prototypical PWR conditions [10].

To obtain a more representative experiment of a RIA accident, it is essential to properly replicate the thermal hydraulic conditions of it. For instance, fuel tolerance tests require proper deposition of energy into the fuel in order to get a more representative data set of the fuel behavior under similar conditions of this transient accident. One way to recreate the power bursts, typical of a RIA event, is by creating an instantaneous power increase. These power bursts can be performed in the CABRI reactor since its main feature is the injection of reactivity through the depressurization of helium-3 from the transient rods [10]. A schematic of this system is shown in Figure 4.

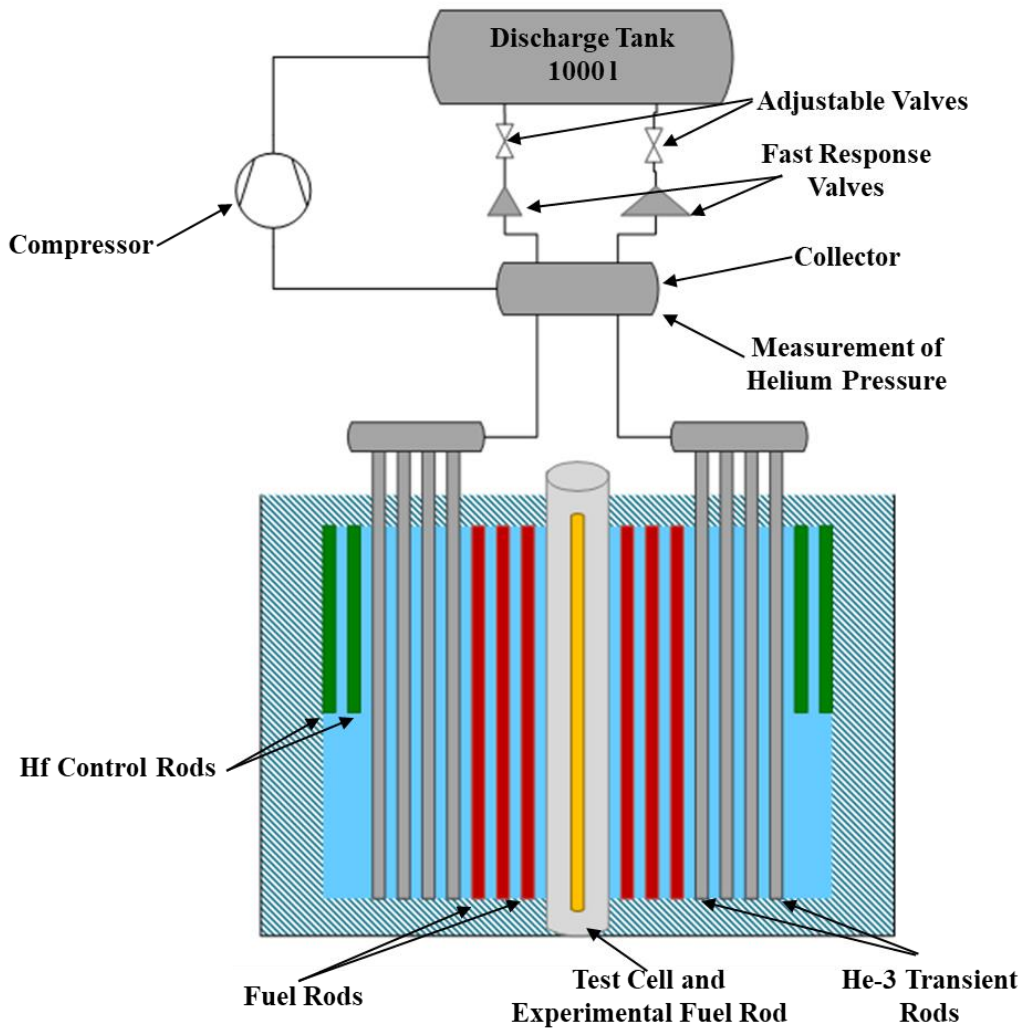


Figure 4. Schematic of CABRI helium-3 transient rod system [11].

The process followed in the CABRI facility to create a power bursts consists of operating the reactor at a relatively low power of about 100 kW [11]. At this point, the fuel sample is assumed to be placed in a test vehicle, which is later placed in a test position inside the reactor core. The transient rods, which are already pressurized with helium-3 and located inside of the reactor core, are pressurized. Due to the fact that helium-3 has a large neutron absorption cross-section, the pressurization of the transient rods prior to the experiment means that the helium is absorbing neutrons. The experiment starts when the fast and well-controlled depressurization of the transient rods causes an increase of reactivity that leads ultimately to a power burst. This means that as helium-3 is removed from the reactor core, the neutron population in the core

increases, resulting in a chain reaction that causes a transient power increase of up to about 20 GW within a few milliseconds [10]. Thereafter, the power is brought back to a safe level due to the Doppler Effect and negative reactivity feedback [10] [11]. An example of this behavior is presented in Figure 5, where it shows the depressurization of the transient rods and the core fission power increase.

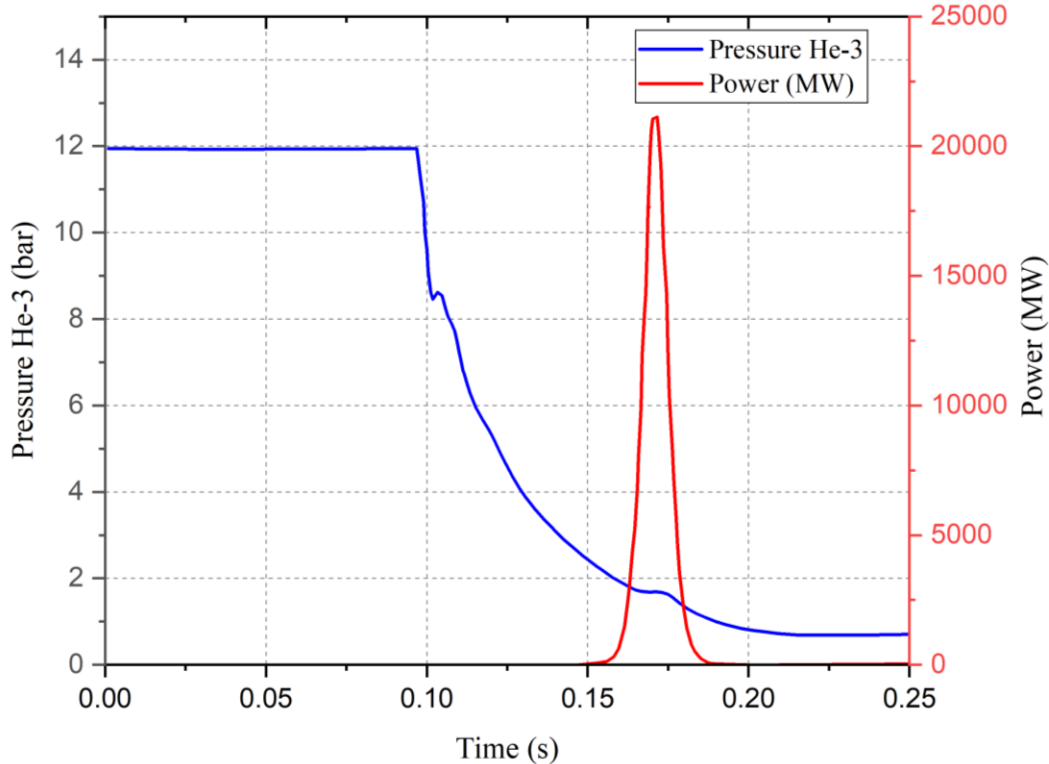


Figure 5. CABRI power transient [11].

Following the power spike, the safety and control rods are inserted into the core in order to adjust the total energy deposited into the sample [11].

The overview of existent helium-3 control rods is important in order to learn from past research done on systems that are similar to the HENRI system. Even though the system employed in the CABRI reactor consists of depressurization instead of pressurization of the gas chambers, this system shares a common objective as the HENRI system. These two systems are meant to control the reactor's pulse by adjusting the helium-3 atomic density inside of the gas chambers. This means that it is paramount to have a

good understanding of the atomic density evolution inside of the gas chambers and be able to accurately measure it.

## 2.4 STAR-CCM+ Governing Equations

The basic governing equations used by STAR-CCM+ or any other CFD software are the conservation of mass, momentum and energy. These equations can be expressed using an Eulerian or a Lagrangian approach due to the fact that STAR-CCM+ uses both to solve fluid problems based on whichever is more convenient [13]. The continuity equation can be written in the following form,

$$\frac{\partial \rho}{\partial t} + \frac{\partial}{\partial x}(\rho u) + \frac{\partial}{\partial y}(\rho v) + \frac{\partial}{\partial z}(\rho w) = 0. \quad (13)$$

Equation (13) can also be written into the Eulerian form,

$$\frac{\partial \rho}{\partial t} + \nabla \cdot (\rho \bar{v}) = 0, \quad (14)$$

where the first term of Equation (14) is the rate of change of mass in control volume,  $\nabla$  is the mathematical expression to express gradients,  $\rho$  represents the fluid's mass per unit volume, and  $\bar{v}$  represents the continuum velocity [14]. The continuity equation shown above can be used for both compressible and incompressible fluids. The conservation of linear momentum which is Newton's second law of motion, for the x-, y- and z- direction can be written in the following form [14]:

$$\rho \frac{\partial u}{\partial t} = -\frac{\partial P}{\partial x} + \frac{\partial}{\partial x} \left( \mu \frac{\partial u}{\partial x} \right) + \frac{\partial}{\partial y} \left( \mu \frac{\partial u}{\partial y} \right) + \frac{\partial}{\partial z} \left( \mu \frac{\partial u}{\partial z} \right) + F_{e,x}, \quad (15)$$

$$\rho \frac{\partial v}{\partial t} = -\frac{\partial P}{\partial y} + \frac{\partial}{\partial x} \left( \mu \frac{\partial v}{\partial x} \right) + \frac{\partial}{\partial y} \left( \mu \frac{\partial v}{\partial y} \right) + \frac{\partial}{\partial z} \left( \mu \frac{\partial v}{\partial z} \right) + F_{e,y}, \quad (16)$$

$$\rho \frac{\partial w}{\partial t} = -\frac{\partial P}{\partial z} + \frac{\partial}{\partial x} \left( \mu \frac{\partial w}{\partial x} \right) + \frac{\partial}{\partial y} \left( \mu \frac{\partial w}{\partial y} \right) + \frac{\partial}{\partial z} \left( \mu \frac{\partial w}{\partial z} \right) + F_{e,z}. \quad (17)$$

The equations presented for the conservation of linear momentum can be also written into its vector form,

$$\rho \frac{\partial \bar{v}}{\partial t} = -\nabla P - \mu \nabla^2 \bar{v} + F_e, \quad (18)$$

where  $P$ ,  $\mu$ , and  $F_e$  represent the pressure, dynamic viscosity, and external forces per unit volume, respectively. It is important to note that the shear stress can be written as,

$$\tau = \mu \left[ \nabla v + \nabla v^T + \frac{2}{3} \nabla \cdot v \right]. \quad (19)$$

The third equation, the energy equation, can be written into the following form,

$$\rho \frac{\partial e}{\partial t} + \nabla \cdot (\rho e \bar{v}) = \nabla \cdot (k \nabla T) + \Phi + S_i, \quad (20)$$

where  $e$ ,  $k$ ,  $T$ ,  $\Phi$ , and  $S_i$  represent the internal energy per unit mass, thermal conductivity, temperature, viscous dissipation rate and energy source per unit volume, respectively.

As previously mentioned, the three conservation equations, continuity, linear momentum, and energy, are part of the set of primary equations that help STAR-CCM+ simulate internal and external fluid flow for a variety of fluid types and flow regimes. However, an extra equation that can describe the relationship between the density, pressure and temperature is needed. Equation (21) is known as the equation of state for an ideal gas,

$$\rho = \frac{P}{RT}, \quad (21)$$

where  $P$  is the pressure,  $T$  is the temperature, and  $R$  is the specific gas constant.

The equations previously covered in this section form part of the fundamental equations used by STAR-CCM+ to solve a wide range of problems. The overview of these equations is essential to get familiar with the equations that are being solved for the simulations that form part of this study.

## 2.5 Boundary Layer and Wall Treatment

Most of the CFD simulations, including the simulations covered in this study, are bounded at least by one or more solid surfaces. The study of the fluid's behavior at solid surfaces is important because the roughness of a surface and viscosity of the fluid have a direct impact on the fluid's tendency to flow at the boundary. As the fluid incurs a shear stress on the solid surface, a boundary layer is created as seen in Figure 6.

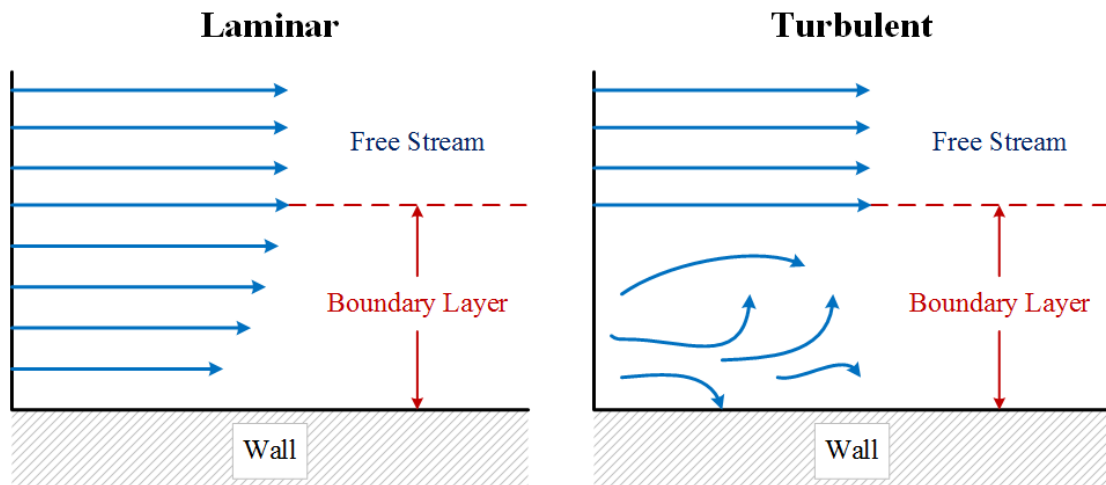


Figure 6. Velocity distribution for laminar and turbulent flows [15].

As it can be seen in Figure 6, the fluid is divided into two sections, free stream and boundary layer. The velocity profile at the boundary layer for a turbulent and a laminar flow are different as the turbulent flow has eddies and swirls, whereas the laminar flow

has a smooth flow. The extent of these layers can be calculated using the dimensionless  $y^+$  value, which can be described as,

$$y^+ = \frac{u_\tau y}{v}, \quad (22)$$

where  $u_\tau$ ,  $y$ , and  $v$  are the friction velocity, distance to the wall, and kinematic viscosity, respectively. The friction velocity and the kinematic viscosity can be written in the following form,

$$u_\tau = \sqrt{\frac{\tau_w}{\rho}}, \quad (23)$$

and,

$$v = \frac{\mu}{\rho}. \quad (24)$$

Here,  $\tau_w$  is the wall shear stress,  $\mu$  is the dynamic viscosity, and  $\rho$  is the density of the fluid. Figure 7 shows the law of wall for horizontal velocity near a wall.

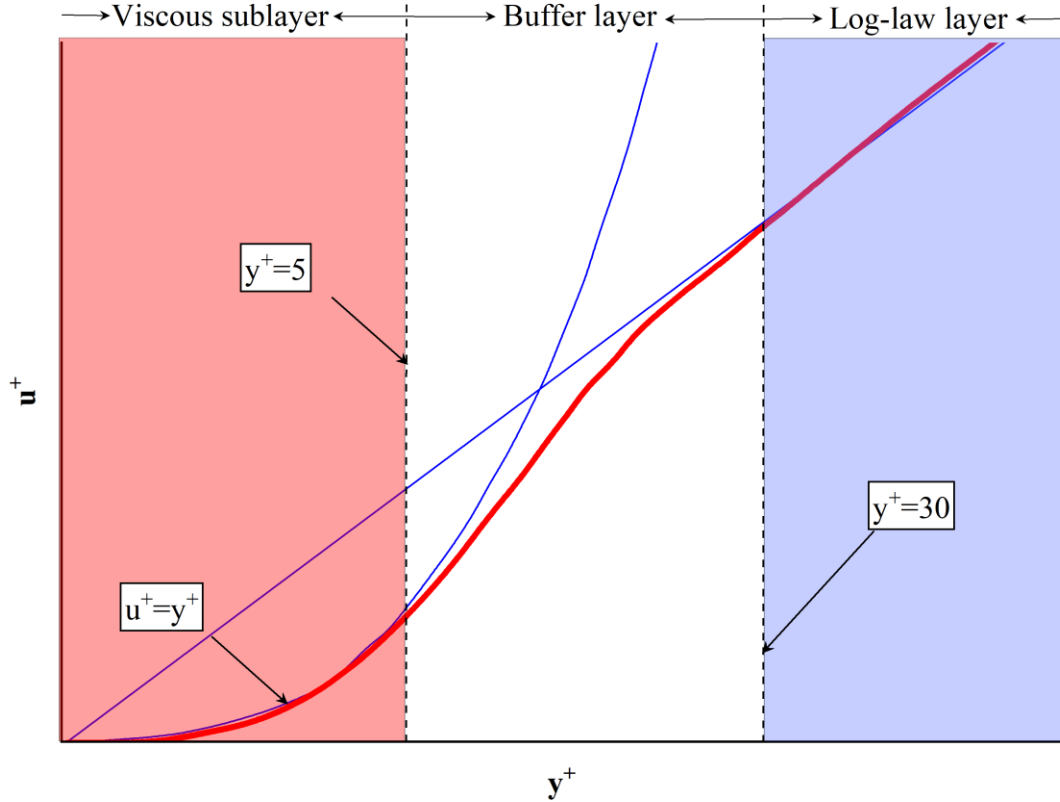


Figure 7. Law of wall for horizontal velocity near a solid surface [13].

Figure 7 divides the values of  $y^+$  into three regions, viscous sublayer, buffer layer, and log-law layer. For a  $y^+$  value of equal or less than 5, the dimensionless velocity,  $u^+$ , is well resolved as the Reynolds shear stress is negligible. Based on this, it can be concluded that:

$$u^+ = y^+. \quad (25)$$

However, for  $y^+$  values greater than 5 and lower than 30, their difference is considerable. If the log-law is implemented for this region, the difference is also non-negligible. Thus, while running simulations, it is recommended to avoid  $y^+$  values that fall within the buffer layer. The velocity profile in the log-law region is well resolved using the following equation,

$$u^+ = \frac{1}{\kappa} \ln(y^+) + B, \quad (26)$$

where  $B$  is a constant and  $\kappa$  is the Von Kármán constant [16]. STAR-CCM+ has three wall treatment options available to resolve the flow behavior at the boundary. Table 1 lists the 3 wall treatment options available in STAR-CCM+, and recommendations of which wall treatment to choose based on the user needs.

Table 1. Wall treatment recommendations retrieved from reference [13].

Wall treatment	Choose when:
High $y^+$	<ul style="list-style-type: none"> <li>• Wall-bounded effects are not a priority.</li> <li>• Separation is expected only due to sharp changes in the geometry.</li> <li>• Wall roughness effects need to be included.</li> <li>• Simulation time and thus cell count is a critical issue.</li> <li>• The selected turbulence model does not explicitly damp the turbulence in the near-wall region. Examples: Standard and Realizable K-epsilon models.</li> </ul>
Low $y^+$	<ul style="list-style-type: none"> <li>• An accurate prediction of the boundary layer velocity and/or temperature profile is important, such as for pressure-drop or drag calculations.</li> <li>• The boundary layer tends to separate due to adverse pressure gradients.</li> <li>• Simulation time and thus cell count is not a critical issue.</li> <li>• The selected turbulence model damps the turbulence in the near-wall region. Example: Standard K-epsilon Low-Reynolds Number model.</li> </ul>
All $y^+$	<ul style="list-style-type: none"> <li>• Choose this approach whenever available, especially when it is difficult to achieve a pure high- or low-<math>y^+</math> mesh because of varying geometrical and velocity scales associated with the model.</li> </ul>

Computational fluid dynamics models require to choose a  $y^+$  target value in order to select the most adequate wall treatment model and identify the best prism layer thickness. If the prism layer thickness is not chosen correctly, it will result in a poor simulation of the fluid near the boundaries. For the simulations covered in this study, a desired  $y^+$  value was chosen in order to calculate the prism layer thickness.

## 2.6 Turbulence Models

The theory behind laminar flow has been studied for years, and it is an area of fluid dynamics that is well documented. However, turbulent flow is a subject that is not as straightforward as laminar flow due to the randomness that takes place on the fluid's behavior. In CFD, there are different models that can simulate turbulent flows. Those models are:

1. Direct Numerical Simulations (DNS),
2. Large Eddy Simulations (LES),
3. Detached Eddy Simulations (DES), and
4. Reynolds-Averaged Navier-Stokes (RANS).

As the name suggests, Direct Numerical Simulations are numerical simulations of the Navier-Stokes equations in a 3-dimensional space. One of the characteristics of this turbulence model approach is that each simulation is an independent realization of the flow, so the numerical approach does not impose averaging. This means that DNS numerically simulates the temporal evolution of the turbulence structure, including phenomena related to the kinetic energy dissipation. One of the main limitations of this turbulence model approach is that it requires large computational resources, so large Reynolds numbers ( $Re \geq 200$ ) cannot be simulated [16].

Large Eddy Simulations is a turbulence model approach that solves time dependent Navier-Stokes equations. LES is able to resolve large-scale phenomena of turbulent flows such as vortexes, while the smallest scales of the flow are modeled using a

subgrid-scale (SGS) turbulence model. It is claimed that the main success of LES is its ability to simulate large-scale turbulent phenomena [16].

The Detached Eddy Simulations model was created to address the phenomena that takes place in fields of aerospace and ground transportation, where high Reynolds number and separated flows take place. DES is a combination of LES and RANS as LES is good at simulating large-scale phenomena but computationally expensive, and RANS is good at simulating thin boundary layers but lacks at simulating large separation regions [17]. Even though DES is computationally less expensive than DNS, it requires more computational power compared to the RANS model.

The Reynolds-Averaged Navier-Stokes model is an approach that is able to resolve large scale eddies while small phenomena is computed by the Reynolds stresses. Under the RANS model, several turbulence models are available, such as the Mixing-length model, which is claimed to be the simplest turbulence model, the Spalart-Allmaras model, which is a one-equation model, and the two-equation turbulence models, k-epsilon and k-omega.

The two most widely used turbulence models are k-epsilon ( $k-\epsilon$ ) and k-omega ( $k-\omega$ ). The main difference between these two models is that the second term for  $k-\omega$  is the specific turbulent dissipation rate,  $\omega$ , instead of the turbulent dissipation rate  $\epsilon$ . The turbulence model  $k-\epsilon$  has several advantages including its ability to simulate free stream, but one of the major drawbacks of it is its capability of simulating flow near walls unless damping functions are used. On the other hand,  $k-\omega$  is known to have good capability of simulating the boundary layer very well, but the free stream treatment is more complex. To address the drawbacks of these two turbulence models, the  $k-\omega$  Menter SST, and the adopted turbulence model for this study, combines the advantages of k-epsilon and k-omega by using the accurate formulation of k-omega for flows in the near-wall regions, and the free-stream is simulated using the k-epsilon formulation. To have a better understanding of how  $k-\omega$  Menter SST works, it is necessary to review the standard k-epsilon equations, which are:

$$\frac{d(\rho k)}{dt} + \nabla \cdot (\rho U k) = \nabla \cdot \left\{ \left( \mu + \frac{\mu_t}{\sigma_k} \right) \nabla k \right\} + P_k - \rho \varepsilon, \quad (27)$$

$$\frac{d(\rho \varepsilon)}{dt} + \nabla \cdot (\rho U \varepsilon) = \nabla \cdot \left\{ \left( \mu + \frac{\mu_t}{\sigma_\varepsilon} \right) \nabla \varepsilon \right\} + C_{1\varepsilon} P_k \frac{\varepsilon}{k} - C_{2\varepsilon} \rho \frac{\varepsilon^2}{k}. \quad (28)$$

If the identity,

$$\varepsilon = C_\mu k \omega, \quad (29)$$

is substituted into the dissipation rate equation, it yields:

$$\frac{d(\rho \omega)}{dt} + \nabla \cdot (\rho U \omega) = \nabla \cdot \left\{ \left( \mu + \frac{\mu_t}{\sigma_k} \right) \nabla \omega \right\} + \frac{\gamma}{v_t} P_k - \beta \rho \omega^2 + 2 \frac{\rho \sigma_{\omega 2}}{\omega} \nabla k : \nabla \omega. \quad (30)$$

If Equation (30) is compared to the k- $\omega$  turbulence model, which is:

$$\frac{d(\rho \omega)}{dt} + \nabla \cdot (\rho U \omega) = \nabla \cdot \left\{ \left( \mu + \frac{\mu_t}{\sigma_k} \right) \nabla \omega \right\} + \frac{\gamma}{v_t} P_k - \beta \rho \omega^2, \quad (31)$$

it can be noted that both equations are almost identical; however, Equation (30) has an extra term on the right-hand side of the equation. To combine both equations, a blending function is used for the additional term of Equation (30). This blending function, along with the extra term, is:

$$2(1 - F_1) \frac{\rho \sigma_{\omega 2}}{\omega} \nabla k : \nabla \omega, \quad (32)$$

where  $F_1$  ranges from 0 to 1. The blending function,  $(1 - F_1)$ , allows the k- $\omega$  Menter SST turbulence model to switch from k-epsilon to k-omega. For flows near the wall,

refer to Figure 8,  $F_1$  assumes a value of 1 to utilize the k-omega equation, and for free stream,  $F_1$  assumes a value 0 to switch to the k-epsilon equation.

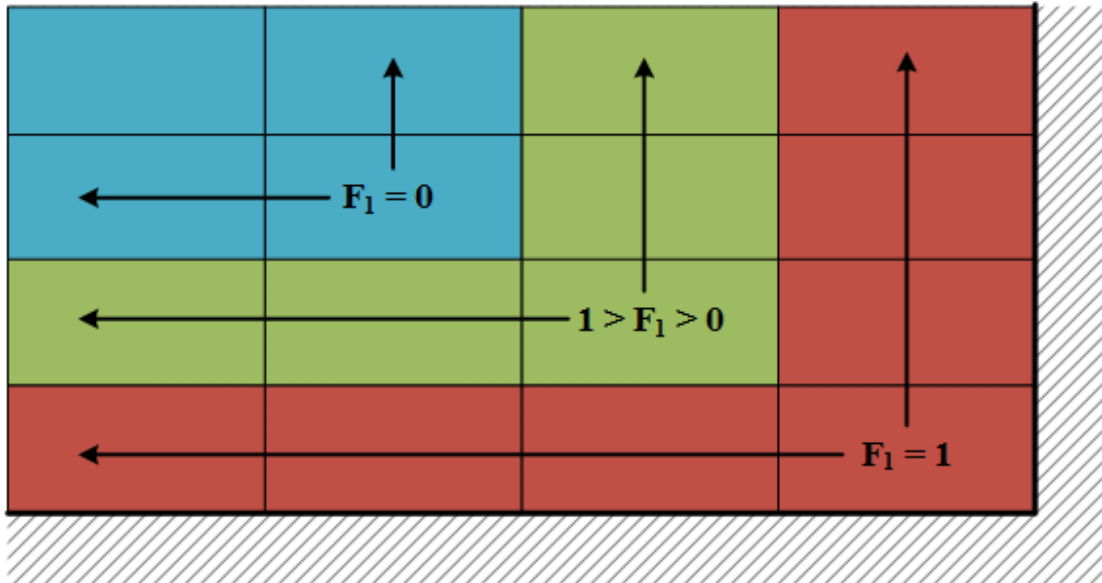


Figure 8. K-omega Menter SST blending function.

The value  $F_1$  is obtained from the following relationship:

$$F_1 = \tanh \left\{ \left[ \min \left( \max \left( \frac{\sqrt{k}}{\beta^* \omega y}; \frac{500v}{y^2 \omega} \right); \frac{4\rho\sigma_{\omega 2}k}{CD_{k\omega}y^2} \right) \right]^4 \right\}, \quad (33)$$

where  $y$  is the distance from the nearest wall, and  $CD_{k\omega}$  is written as:

$$CD_{k\omega} = \max \left( 2\rho\sigma_{\omega 2} \frac{1}{\omega} \frac{\partial k}{\partial x_j} \frac{\partial \omega}{\partial x_j}, 10^{-10} \right). \quad (34)$$

$F_1$ , in addition to help to switch from k-omega to k-epsilon and vice versa, is used to blend between the empirical constants, shown in Table 2, using the following relationship:

$$\phi = \phi_\omega F_1 + \phi_\epsilon (1 - F_1). \quad (35)$$

It is important to note that the viscosity is computed differently compared to the standard k-omega. The turbulent eddy viscosity is calculated using,

$$\mu_t = \frac{a_1 \rho k}{\max(a_1 \omega, S F_2)}, \quad (36)$$

where  $F_2$  is a limiter for the viscosity, and  $S$  is the magnitude of the shear strain. The closure coefficients and auxiliary relations are shown in the following table.

Table 2. Closure coefficients for k-omega Menter SST [18].

Constant	Value
$\alpha_1$	0.31
$\beta_1$	0.075
$\beta_2$	0.0828
$\beta^*$	0.09
$\sigma_{k1}$	0.85
$\sigma_{k2}$	1.0
$\sigma_{\omega 1}$	0.5
$\sigma_{\omega 2}$	0.856
$\kappa$	0.41

## 2.7 CFD simulation of the CABRI transient rods

CABRI, which is an experimental pulse reactor, is meant to perform transient tests on nuclear fuels. Since 1978, the testing campaigns carried out in the research reactor have been focused on the recreation of RIA accident events [19]. For this, the reactor has what is called “transient rods”, which are gas chambers filled with helium-3 [12]. By

depressurizing the gas chambers, the reactivity injection reaches up to \$3.90 in a few milliseconds [19]. In order to properly recreate RIA events, it is crucial to properly manipulate the density evolution of the gas chambers. Thus, a CFD analysis was performed to analyze the density evolution during a power transient using STAR-CCM+ and the DULCINEE multiphysics code.

The depressurization of the transient rods required an analysis using CFD software due to the fact that a CFD model is capable of solving several equations with complex geometries. As a result, an assessment of the performance of this system was done using the commercial CFD software, STAR-CCM+. The development of the CFD model was divided into three sections [19]:

1. Development of the geometry. This stage involves the development of the geometry using a 3D-CAD modeler, identification of the boundary conditions, selection of the physics models that can properly simulate the physical properties of the fluid, and the development of the mesh.
2. Solve the Navier-Stokes equations using the CFD solver. Following the pre-processing stage, STAR-CCM+ solves the Navier-Stokes equations by implementing a numerical approach.
3. Analysis of results. The last stage consists of post-processing the results obtained from the CFD solver. The results can be displayed using contour plots, x-y plots, and more.

The setup used for the CFD model can be seen in Table 3.

Table 3. CABRI's CFD model setup

Category	Setup chosen
Physics Models	3D modeling
	RANS (Reynolds Averaged Navier-Stokes)
	k- $\epsilon$ turbulence model
	All y + wall treatment
	Implicit solver
	Ideal gas: Thermal conductivity and dynamic viscosity of helium versus temperature were implemented
Meshing	Trimmer mesher (10 mm)
	2 Prism layers
Initial Boundary Conditions	High pressure section: varying from 1 to 14.85 bar Low pressure section: 66 mbar Ambient temperature: ~293 K Transient rods circuit: from 100 to 800 K

The validation process of the CFD model was done by comparing the CFD results with experimental data. For this, the depressurization of the transient rods is modeled. Figure 9 compares the results obtained from the CFD model and the experimental data.

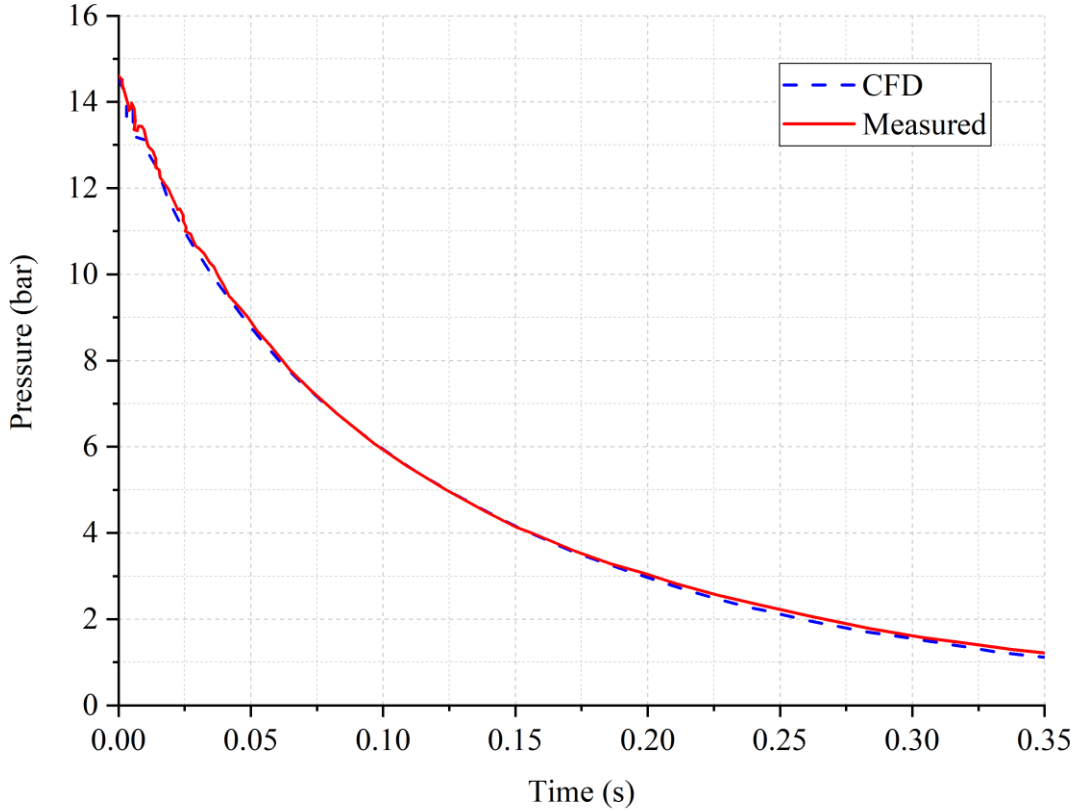


Figure 9. Comparison of CFD vs experimental data [19].

Based on Figure 9, the CFD model, with the chosen physics models, is able to reproduce the depressurization of the gas chambers. The overview of past research done on the CFD modeling of systems that use helium-3 as a way to insert negative reactivity is important as past information can be used to improve the model for the HENRI system.

### 3 FACILITY DESCRIPTION

#### 3.1 Overview

Even though the idea of using helium-3 to clip the pulse of a nuclear reactor is not a novel idea, it is important to demonstrate the feasibility and repeatability of the HENRI system. As stated in earlier chapters, the development of a gas injection system for the TREAT reactor was originally proposed by INL and designed and built at OSU to

address the system's performance. The design of the test facility has several constraints, but the main ones are: (1) the speed and repeatability of the valves and (2) the scarcity and cost of helium-3.

One of the proposed goals of this system is to reach the desired atomic density in the gas chamber within 5 ms. This means that the valves chosen for this system must have a very fast opening time. Also, since this system will be placed inside of the reactor core, ideally a reusable valve should be used. The scarcity of helium-3 is another key challenge for the facility since the cost of this noble gas is considerably expensive. Prior to the development of the out-of-pile HENRI test facility, it is required to perform preliminary calculations in order to determine the amount of helium-3 needed to reduce the neutron population so the pulse can be clipped. This analysis was done by INL using the MCNP code, which is a stochastic code used for neutron, electron, proton or coupled neutron, electron, proton transport. Through the use of this code, it was estimated that with an annular in-core pressure chamber geometry of 2.75 in. OD x 2.25 in. ID with an atomic density of  $3.35 \times 10^{20} \text{ atoms/cm}^3$  would provide the highest neutron-capturing flux area and limit volume consumption. Based on the inner and outer diameters provided and the length of the active core, the total volume of the gas chamber is  $1167 \text{ cm}^3$ . Since the atomic density is challenging to manipulate directly, it is advised to reach the desired atomic density by adjusting the temperature and pressure. Table 4 provides the helium-3 atomic and molecular densities used in the MCNP worth calculations for the HENRI facility for a volume of  $1167 \text{ cm}^3$  at  $25^\circ\text{C}$ . Based on the information presented in the Table 4, a pressure of 200 psi is required to reach the desired atomic density.

Table 4. Atomic and molecular density of helium-3.

Pressure [psi]	Atomic density $\left[ \frac{atoms}{cm^3} \right]$	Molecular density $\left[ \frac{moles}{cm^3} \right]$
100	$1.675 \times 10^{20}$	$2.782 \times 10^{-4}$
200	$3.350 \times 10^{20}$	$5.563 \times 10^{-4}$
300	$5.025 \times 10^{20}$	$8.344 \times 10^{-4}$
400	$6.700 \times 10^{20}$	$1.113 \times 10^{-3}$
500	$8.375 \times 10^{20}$	$1.391 \times 10^{-3}$
600	$1.005 \times 10^{21}$	$1.669 \times 10^{-3}$
700	$1.173 \times 10^{21}$	$1.947 \times 10^{-3}$
800	$1.340 \times 10^{21}$	$2.225 \times 10^{-3}$
900	$1.508 \times 10^{21}$	$2.503 \times 10^{-3}$
1000	$1.675 \times 10^{21}$	$2.782 \times 10^{-3}$

Even though the amount of helium-3 needed to clip the pulse is considerably small, the amount needed for the driver tank is considerably large. In addition to these constraints, the facility is required to fulfill the following requirements:

- The repeatability of the fast opening valve shall be within 2 ms.
- The amount of helium-3 needed for the system must not exceed 4000 liters at standard pressure and temperature. A smaller quantity is encouraged.
- The system must be able to repeat the process for at least 1000 cycles.
- The system must comply with the ASME boiler and pressure code. This means the safety factor of the system must be at least 2.0 or higher so the final in-core design meets the safety standards.
- The system's geometry design must be bounded based on the footprint available for it. Further information is provided in the following section.

### 3.2 Design

Since this system is anticipated to operate inside of the reactor core of the TREAT facility, it is paramount to constraint its size based on the space available for the transient rods. The assembly is limited to a 4 x 4 in. footprint in the core itself, as shown in Figure 10, and an 8 in. diameter cylinder above the core for the driver tank.

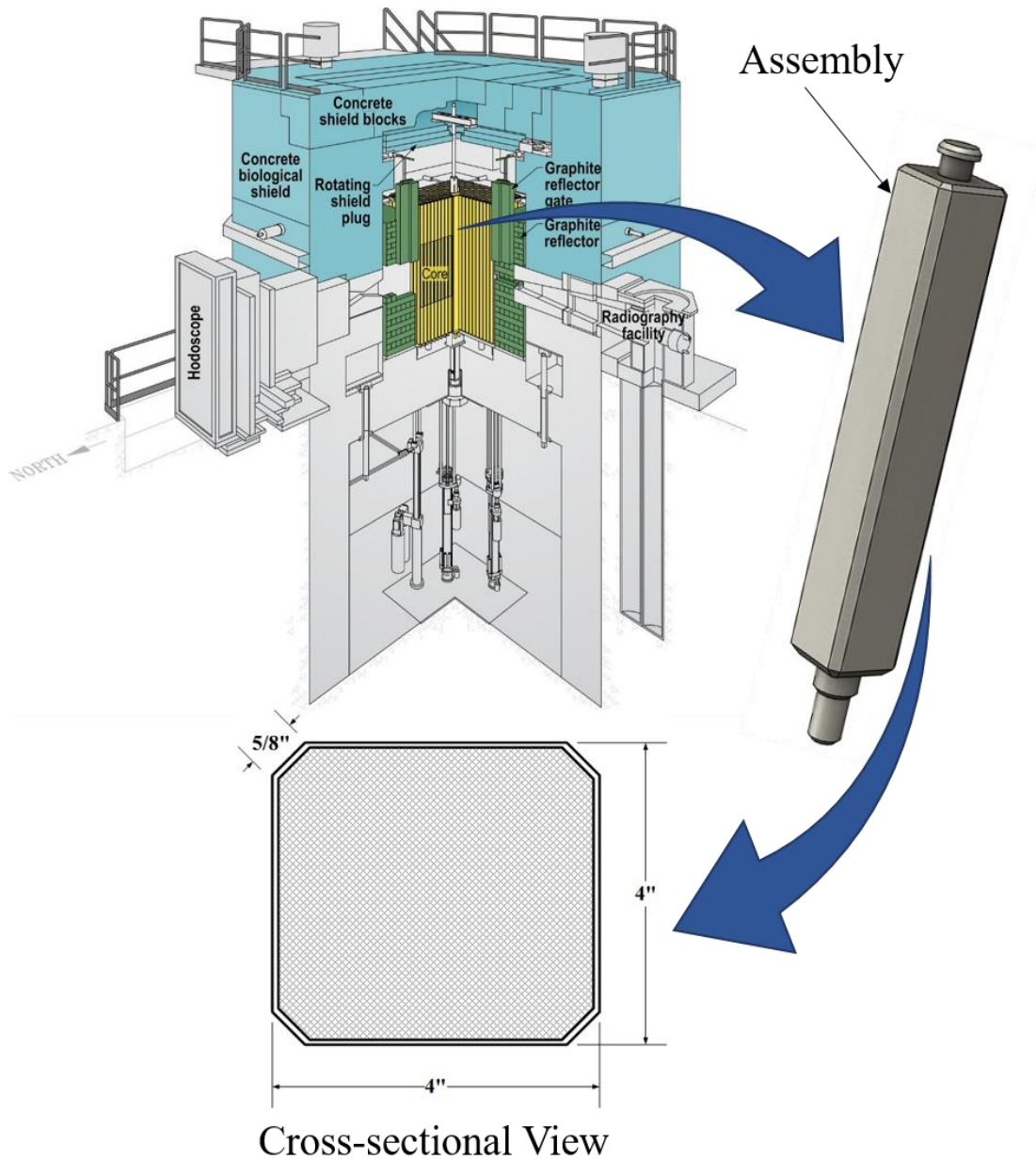


Figure 10. TREAT's assembly cross-sectional view [20].

Prior to performing experimental tests on an annular gas chamber, which ultimately is the final design of the cartridge, it is recommended to perform experiments on a simpler geometry with a fast response opening system. This approach helps to test the software and instrumentation, have a better understanding of the gas dynamics in a simpler geometry, obtain confidence on the system's setup, and execute preliminary pressure tests to have an idea of the system's performance at different initial conditions. For the geometry of the test section, instead of performing tests on an annular gas chamber a simple tube geometry with the same volume is advised. Based on the requirements and boundary conditions in place, OSU designed a driver tank, refer to Figure 11, used to hold the helium. Since this system requires to operate for a short period of time, the stainless-steel driver tank is pressurized to a high pressure so the working fluid can move from a high-pressure section to a low-pressure section. The driver tank, which is intended to be located above the core, is rated to 9.93 MPa (1440 psig) at 311 K (100 °F) for a total volume of 5.90 liters. [20] Due to the fact that the driver tank will be located above the core, a connection between the driver tank and the gas chamber is required. Thus, an intermediate section (Figure 12) is included in the design.



Figure 11 . HENRI test facility driver tank.

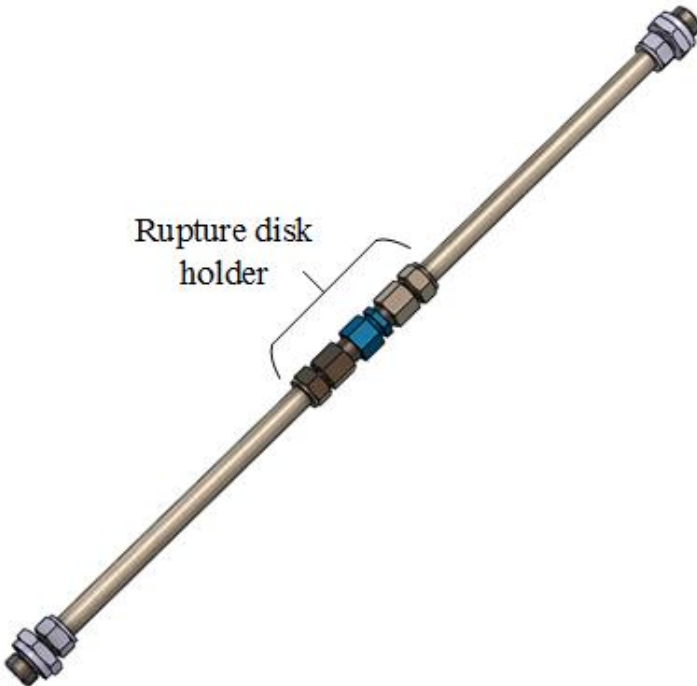


Figure 12. Out-of-pile HENRI test facility intermediate section [20].

It is envisioned that a fast response valve will be included to the design of the HENRI system. However, existing fast response valves are not fast enough for this system. To address this issue, OSU has designed a fast opening valve system that is actuated using a piston. Even though a new fast response valve is being developed for the HENRI system, rupture disks are used for the early design stages of this facility. Rupture disks are placed in the middle of the intermediate section using a disk holder as seen in Figure 12. Since these rupture disks are designed to burst at specific pressures, it is important to identify the desired pressure level of the driver tank, so the rupture disks can be purchased based on the pressure at which they need to be triggered. Table 5 shows the different rupture disk sizes used for the out-of-pile HENRI test facility.

Table 5. Rupture disk description

Burst rating pressure kPa (psia)	Rupture disk diameter mm (in)	Rupture disk type	Test section geometry
3447 (500)	17.47 (11/16)	Fragmenting	
5160 (800)	17.47 (11/16)	Fragmenting	
6895 (1000)	17.47 (11/16)	Fragmenting	
6895 (1000)	12.7 (1/2)	Non- fragmenting	
6895 (1000)	19.05 (3/4)	Non- fragmenting	
6895 (1000)	25.4 (1)	Non- fragmenting	

Prior to the beginning of a fuel test in the TREAT facility, it will be desired to have the annular gas chamber under vacuum conditions as helium-3 inserts negative reactivity. As stated in previous sections of this document, the proper clipping of the TREAT's pulse involves the proper pressurization of the annular gas chamber of the HENRI system as fast as possible using helium-3. This means that the helium located in the reservoir or driver tank will move from a high-pressure section to the low one. Since the low-pressure section will be under vacuum conditions, a large discontinuity of pressure will take place as helium molecules move towards the other end of the system,

resulting in the formation of shock waves. It is important to analyze the phenomena that takes place inside of the facility as it can be crucial for the design of it. In this case, shock waves can disturb the system's performance. Shock waves tend to reflect on solid surfaces, similar to the wall located at the end of the test section. This means that once the shock wave reaches the end of the test section, it will bounce back resulting on the collision between the particles moving from the high to low pressure section with the wave front. This interaction causes the particles to be stopped, elongating the time it takes to pressurize the test section. To address this issue, an extension section should be used.

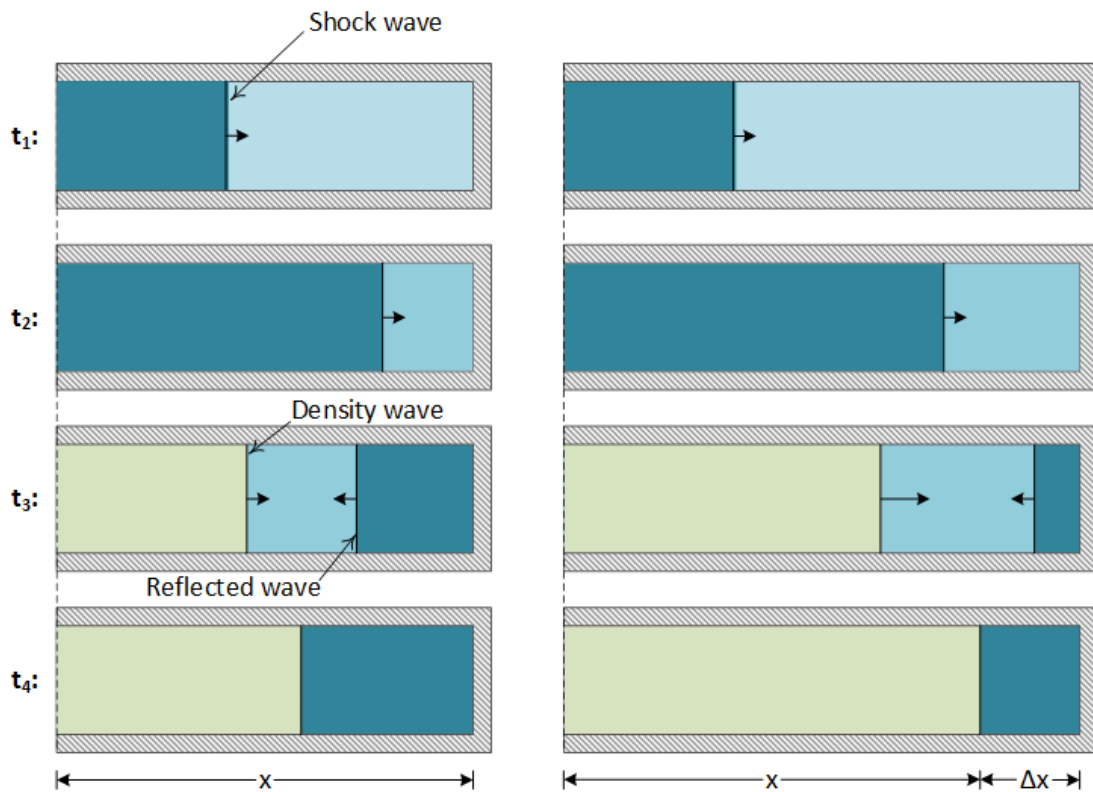


Figure 13. Schematic of shock wave interaction with extension (right) and without extension (left).

To better explain the benefit of using the extension section, Figure 13 shows two examples. On the left side, it shows the wave displacement at the end of the test section without an extension section. On the right side, an extension is added to the test section,  $\Delta x$ . At  $t_1$  and  $t_2$ , the shock wave is moving towards the low-pressure section. When the

shock wave reaches the end, the wave is reflected. At  $t_3$ , the density front and the reflected wave are moving towards each other. Thereafter, at  $t_4$ , the reflected wave and the density front collide. The main difference between both examples is that the shock wave travels longer prior colliding with the density front with the extension section configuration. On the other hand, the scenario that does not include the extension section shows that the reflected wave collides earlier with the density front. In order to reach the desired atomic density level within the test section, the collision between the reflected wave and density front should be delayed as much as possible, allowing more helium molecules to reach the end of the test section. As a result of this analysis, an extension section was added to the design as shown in Figure 14.

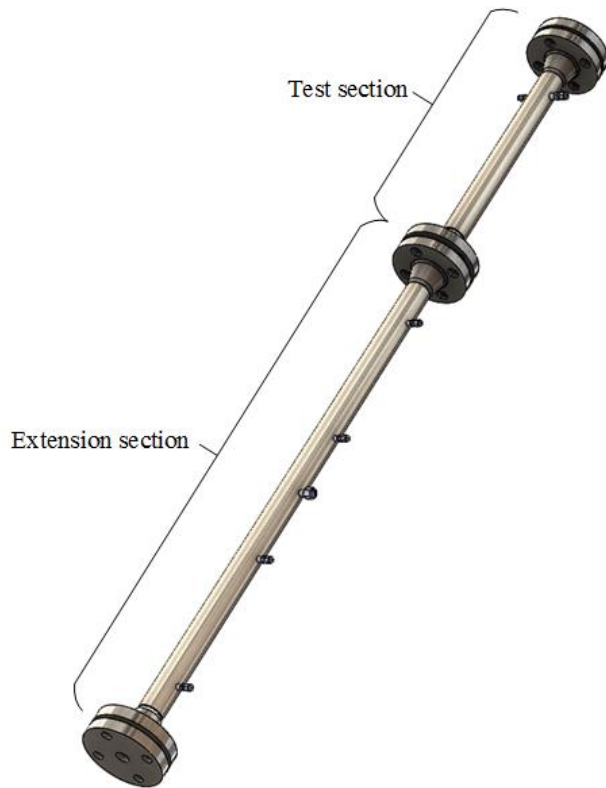


Figure 14. Out-of-pile HENRI test facility test and extension sections [20].

A rendering of the out-of-pile HENRI test facility is shown in Figure 15.

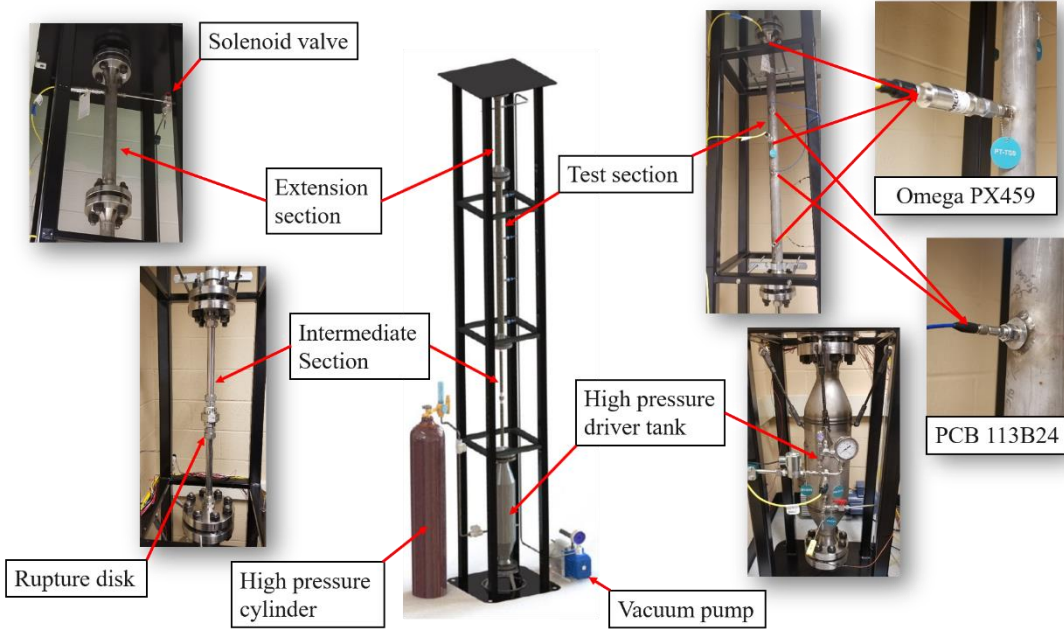


Figure 15. Rendering of the OSU out-of-pile HENRI test facility [20].

### 3.3 Instrumentation

One of the parameters of interest in this system is the density evolution along the test section. Since there is no instrumentation developed to measure directly the density with such fast response,  $<1\mu\text{s}$ , the out-of-pile HENRI test facility system employs temperature and pressure sensors to calculate the density. The use of fast response instrumentation for the out-of-pile HENRI test facility is needed since pressure, temperature, and density inside of this system changes considerably fast. In addition, a data acquisition system must be used to collect data at a fast rate [20].

The instrumentation used to measure the pressure along the system varies. For the pressure of the driver tank (PT-DV1), an Omega PX459 absolute pressure transducer with a 0.05% accuracy is used. The same sensor is used for the test (PT-TS0, PT-TS1 and PT-TS4) and the extension (PT-RX1) sections. In addition to the Omega sensors, two 113B24 piezoelectric pressure transducers from PCB Piezotronics (PT-TS2 and PT-TS4) were placed in the test section. It is important to note that the Omega sensors measure static pressure with a response time of less than 1 ms, and the piezoelectric

pressure transducers measure dynamic pressure with a response time of less than  $1\ \mu\text{s}$ . The latter sensors are powered through the use of a PCB-482C signal conditioner.

The temperature in the driver, test, and extension sections is measured with a 1/16 in. diameter k-type sheathed thermocouple from Omega. The response time of these thermocouples is considerably slow compared to the fast temperature changes that take place inside of HENRI. The position of the pressure and temperature sensors is shown in Figure 16.

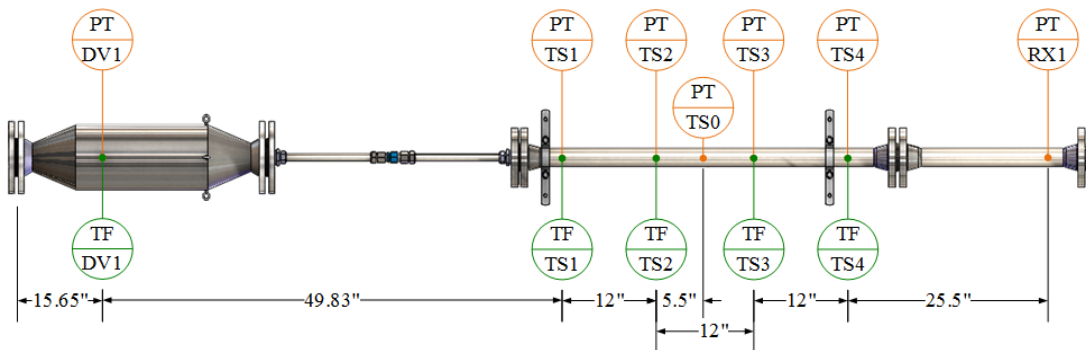


Figure 16. Pressure and temperature sensors location [20].

The instrumentation covered so far have a considerably fast response time, but the information needs to properly be captured through a data acquisition system. The out-of-pile HENRI test facility uses a PXIe acquisition card from National Instruments. The acquisition card, PXIe-4303, has an acquisition rate of 51.2 kHz per channel with a 24-bit resolution.

### 3.4 Matrix Test

The development of a matrix test is important in order to be able to systematically isolate the optimal conditions to reach the desired atomic density within a short timeframe. It is anticipated that the performance of this system is heavily influenced by several factors, including:

- initial pressure and temperature of the gas,
- geometry of the system,

- wall roughness of the annular test section, and
- time to fully open the system's valve.

The system is anticipated to be tested at different initial pressures. Here, three tests are performed, where the driver tank is pressurized at different pressures: 500, 800, and 1000 psi. For these three tests, the pressure of the test section is assumed to be near vacuum conditions, which is achieved through the use of a vacuum pump that is connected to the end side of the extension section. Since it is anticipated that the 1000-psi pressure test will provide the best results, tests focused on the geometry, roughness and valve response are performed using this pressure. Temperature is a parameter that cannot be omitted; however, this system is envisioned to operate in scenarios where the temperature can be assumed to be relatively constant. Thus, the adjustment of temperature in the testing campaign is not considered.

The geometry of the system is tested by changing the tube diameter of the intermediate section. It is anticipated that as the area increases, the mass flow rate increases as well. Three different tube diameters are tested, 1/2", 3/4", and 1", but the one-inch tube diameter is expected to provide the best results. Based on this, the rest of the experiments are performed using the 1" tube diameter. In addition to the change of area of the intermediate section, the geometry of the gas chamber or test section is modified as well. In this case, the test section is modified from a cylindrical to an annular geometry. This change of geometry is meant to indicate how the annular geometry influences the system's performance. Even though the final design consists of using an annular geometry, it is good to quantify how this configuration can influence the gas dynamics.

Since it is unknown if the wall roughness of the annular test section has a significant influence on the system's performance, the wall roughness of the annular test section is tested to determine if a smooth or rough surface has a considerable influence on the system's performance. Here, the inner part of the annular test section is tested using a rough surface, then it is polished until a relatively smooth surface is achieved. The final

stages of this testing campaign consist of testing the fast response opening device. For the first series of tests, rupture disks are used due to their simple installation, low costs, and fast response time. Thereafter, a new fast opening system, a piston valve, is anticipated to be tested to corroborate its repeatability and response time. Appendix B provides a summary of the testing campaign executed in the out-of-pile HENRI test facility.

For the purpose of this study, the out-of-pile HENRI test facility with cylindrical and annular test sections are simulated. However, the configuration considered for the simulations only include rupture disks. Further adjustments to the simulations can be done to adopt the piston valve configuration; however, those studies are out of the scope of this work.

#### 4 CFD MODELING AND METHODOLOGY

The development of CFD models has become an indispensable tool for science and engineering. The increasing use of this tool has been attributed due to the capacity to solve complex flow phenomena through the use of numerical methods in a timely matter. The use of a computational fluid dynamics software can be beneficial from a research standpoint since it can reduce time and costs by obtaining preliminary results using a numerical approach instead of building an experimental facility which can result costly. The development of a CFD model for the HENRI facility is not meant to replace experimental tests. Rather, it is meant to corroborate experimental findings, provide a comprehensive and detailed visualization of the gas behavior by solving a wide range of equations that are complicated to solve through an analytical approach, and simulate the spatial and temporal density evolution inside of the annular gas chamber with high confidence. Due to the fact that a CFD software can solve complex fluid problems in a timely manner, the corroboration of a system's behavior using a numerical approach can pave the path towards the development of a gas injection system for the TREAT reactor without compromising the integrity of the reactor.

The CFD model is anticipated to be coupled with a reactor physics model in order to get a more representative behavior of the HENRI system in the TREAT facility. There are several software available that have the capability of performing gas dynamic simulations; however, this study focuses on the modeling of the HENRI system using STAR-CCM+. This commercial code has the capability of performing fluid dynamics and heat transfer simulations using numerical methods and algorithms. Since this tool can be used for multiple purposes, a strict methodology has been followed to develop simulations that can provide consistent results that are accurate enough and can be obtained in an acceptable amount of time. The use of a standardized methodology is important for proper setup of all CFD simulations and reproducibility of results. The methodology followed for the development of CFD models can be divided into 3-tier steps, as shown below:

1. Development of the flow region geometry, discretization of the geometry domain, identification of the physics models needed to solve or mimic the phenomena desired, and identification of the initial and boundary conditions.
2. Setup of the solver settings which is needed to maintain stability throughout the simulation, identification of the time step, inner iterations, and courant number.
3. The last step consists of processing the information obtained, also known as post-processing. The information can be represented in plots or scenes, and it can be stored in reports. Since this information is collected while running the simulation, it is necessary to create post-processing objects prior running a simulation.

Figure 17 shows a simplified version of the general process that has to be followed to properly setup a simulation.

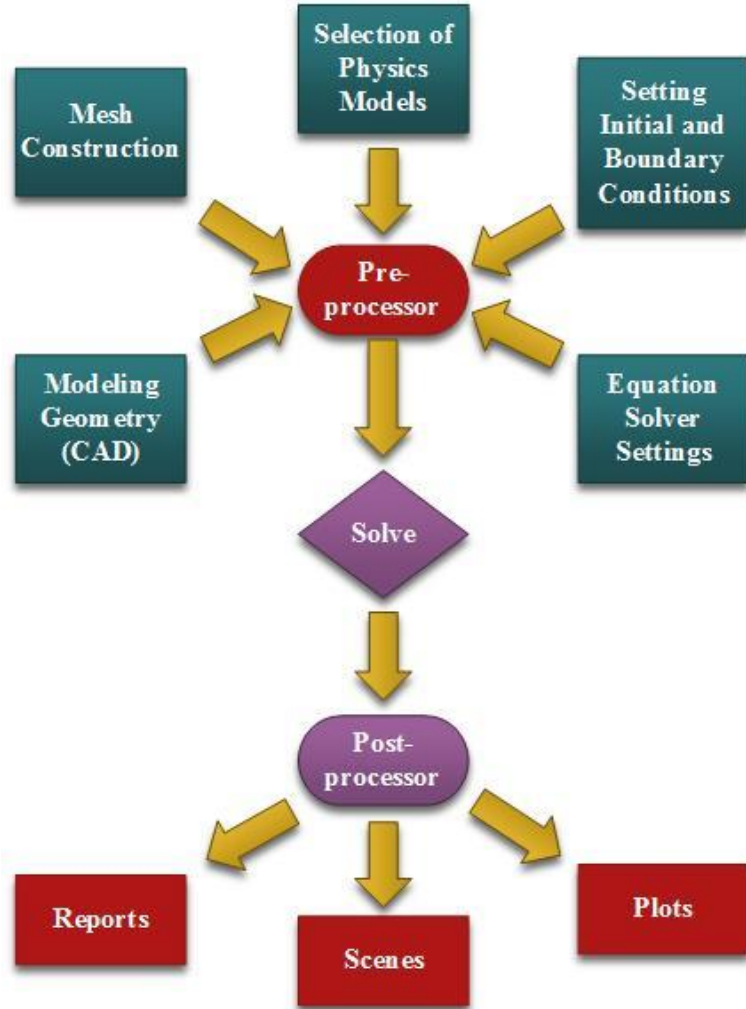


Figure 17. Simplified CFD methodology.

The following sections of this study provides a more in-depth description of the standardized process followed for the development of the CFD model. These sections include information pertaining to the assumptions considered, the analysis performed, and the description of the setup implemented.

#### 4.1 Geometry Development

The 3D modeling of an object can be done through the use of a 3D computer-aided design (3D-CAD) software such as the interface in STAR-CCM+, Siemens NX, SolidWorks, or any other software capable of creating 3D geometries. For the CFD models developed in this study, SolidWorks was used to develop the geometries needed.

The successful development of a CFD model requires to verify that the differential equations are being solved properly and to validate that the CFD model is simulating real-world phenomena properly based on the settings used. For the verification of the CFD model, a shock tube analysis is used to verify that the physics models chosen to simulate supersonic flow are being solved properly with the chosen numerical solver setting. The geometry of the shock tube consists of a long tube with both ends closed. A schematic of the geometry is shown below.

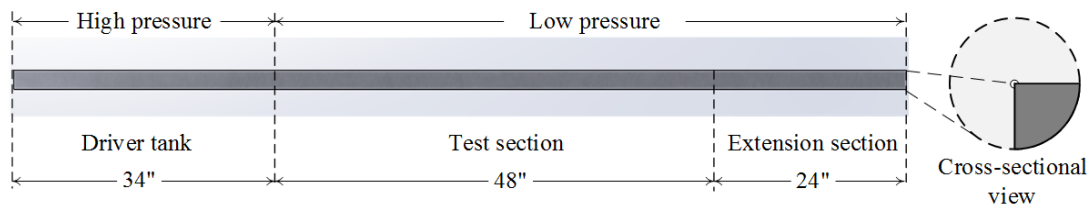


Figure 18. Schematic of a shock tube.

The length of the high-pressure section is based on the length of the driver tank, and the low-pressure section is based on the length of the test section and extension section as it can be seen in Figure 18.

For the validation or benchmark of the CFD model, the experimental data gathered from the cylindrical test section of the out-of-pile HENRI test facility is used to quantify the CFD model capability to recreate real-world phenomena. The geometry adopted for the benchmark is the same as the one used for the out-of-pile HENRI test facility. Figure 19 shows the rendering of the out-of-pile HENRI test facility with a cylindrical test and extension sections along with the 3D geometry used for the CFD model.

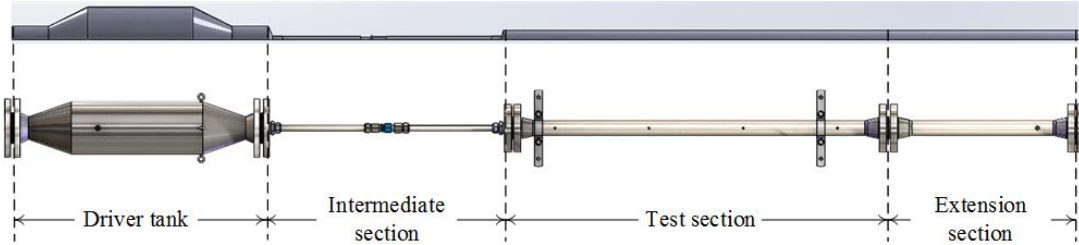


Figure 19. 3D-CAD and rendering of the out-of-pile HENRI test facility.

In addition to the verification and validation of the CFD model, a parametric study is performed on the out-of-pile HENRI test facility with an annular test section. This 3D geometry consists of modeling the same driver tank and intermediate section as shown in Figure 11 and Figure 12; however, the test section has an annular geometry as shown below.

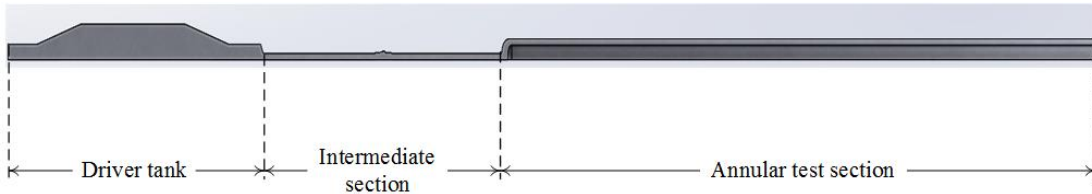


Figure 20. 3D-CAD of annular test section.

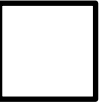
Since the mesh that needs to be implemented in the simulation requires to be small enough to capture shock waves, the computational cost of a 3D simulation is very expensive. As it can be seen in Figure 18, Figure 19, and Figure 20, the geometry is symmetric from the axial point of view. Thus, a 2D axisymmetric simulation was developed in an attempt to reduce the computational cost. The development of a 2D axisymmetric geometry can be performed in STAR-CCM+, but the geometry has to be modified using SolidWorks. Thus, the original geometry must be divided into a quarter of its original size and after converting the mesh of the geometry into a 2D mesh, the symmetry plane can be used as the axis of symmetry for the axisymmetric model. Following the development of the 3D geometries, they were imported to STAR-CCM+. Since the geometry was not developed through the 3D CAD interface in the CFD software, the geometry must be saved as a Parasolid file (.x\_t) in order to be able to import the geometry to STAR-CCM+.

## 4.2 Mesh Generation and Refinement Process

The accuracy of the results from the CFD model can be largely influenced by the mesh imposed on the geometry. The proper selection of the mesh configuration is an important aspect that has to carefully be analyzed in order to reduce the error introduced by it. One important aspect to take into account while selecting the mesh setup is that the smaller the mesh, the solution is more accurate. Ideally, the mesh size of a simulation would be considerably small so the results from the CFD model can have little to no error. Unfortunately, the mesh size is proportional to the computational cost. In other words, the development of a very fine mesh requires to solve several equations for each cell. The finer the mesh, the more equations need to be solved. Thus, the selection of the mesh is a tradeoff between the accuracy of the results and the computational cost of the simulation.

STAR-CCM+ has several types of meshing models that can be implemented based on the available resources, desired outcomes, or geometric constraints. As stated in section 4.1, the development of a 3D CFD simulation can be computationally expensive, and the very fast changes that take place inside of the system. Furthermore, a 2D simulation is adopted for this study. The mesh is created using an automated 2D mesh, where three mesher options are available. The available options are shown in Table 6 [13].

Table 6. Cell-type options for 2D simulations.

Cell type	Diagram	Nodes
Triangular (2D)		3
Quadrilateral (2D)		4
Polygonal (2D)		7

The triangular mesher is an efficient and simple model that allows the development of complex mesh generation problems. If this mesher is compared against the other two mesher models, the triangular is the fastest and uses the least amount of memory for a given number of cells. However, the triangular option produces poor results. In other words, to obtain the same accuracy results as a polygonal or quadrilateral mesh, the triangular requires 5 to 8 times the number of cells [13]. The quadrilateral mesher provides better results than the triangular mesher because the strain of a three noded triangle is constant whereas in a quadrilateral mesher is not the case. In other words, the quadrilateral mesher, which has four nodes, can provide better results than triangular mesher, which uses the constant strain triangle, as the four-node element is able to represent higher order strain states [21]. The polygonal mesher is known to provide more accurate solutions than the triangular mesher, and it is relatively easy and efficient to build, but if the quality of the starting surface triangulation is poor, the mesh quality decreases as well [13]. The quadrilateral and polygonal mesher were tested; however, the residuals of the model that used polygonal reached lower residual values compared to the quadrilateral. Therefore, the polygonal cell type was the option selected.

The base size of the mesh is 3 mm, but the mesh size for the intermediate and low-pressure sections was further reduced. The intermediate section was reduced to 30% relative to the base size (0.9 mm), and the low-pressure section for both, the cylindrical and annular test sections, was reduced to 60% relative to the base size (1.8 mm). Figure 21 shows the mesh size for different sections of the out-of-pile HENRI test facility with cylindrical test section

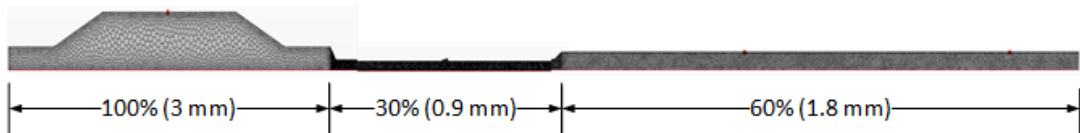


Figure 21. Mesh refinement of out-of-pile HENRI test facility 3D CAD.

The prism layer model is used to improve the accuracy of the flow simulation at the boundaries or surfaces by creating orthogonal prismatic cells. The use of this model is essential since the solver is able to better quantify physics phenomena that takes place near the boundaries such as heat transfer, friction, and more. Prior to the development of the mesh, a subsurface is created based on the prism layer thickness. Thereafter, the mesh is created using this subsurface. Once the core mesh is created, the prism layers are generated by extruding the cell faces from the core mesh [13]. The parameters for the prism layer must be setup while inputting the parameters of the core mesh. The following table shows the parameters needed to develop the prism layer.

Table 7. Description of prism layer setting options.

Parameter	Description
Base size	The base size is the value that all later calculations for the generation of the prism layer will be based upon.
Number of prism layers	This option determines the number of prism layers (refer to Figure 22).
Prism layer stretching	The stretching function determines the cell layer thickness distribution
Prism layer total thickness	It is the property that determines the total overall thickness of all the prism layers (refer to Figure 22).

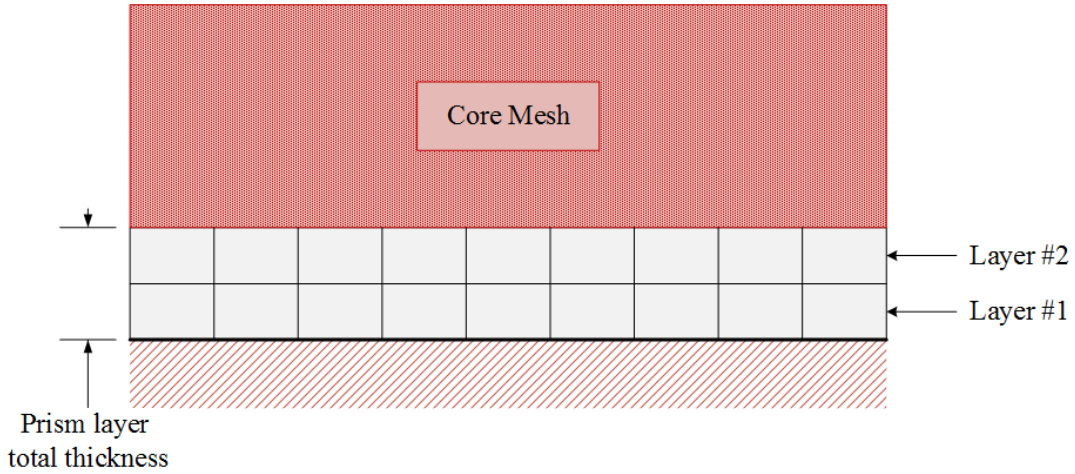


Figure 22. Schematic of prism layer.

In order to choose the appropriate parameters for the prism layer, preliminary calculations of the non-dimensional wall distance parameter,  $y^+$ , were performed. Since the buffer layer region shown in Figure 7 is not well resolved, it is recommended to avoid the  $y^+$  value fall within this range. If the boundary layer is not well resolved, the fluid's properties at the boundary layer will not be calculated correctly and significant errors can result [13]. Section 2.5 of this document provides a table with recommendations regarding what wall treatment should be used. Since the simulation is recreating transient phenomena, it is challenging to have a pure high- or low- $y^+$  value. Thus, the all- $y^+$  wall treatment option was chosen. The preliminary calculations for the prism layer properties were obtained by choosing a  $y^+$  value target of 300. This value was chosen since it falls far away from the buffer layer, and a high  $y^+$  value is being targeted in this study as one thick prism layer can be used to solve the viscous sublayer using the logarithmic law. It is important to note that the more prism layers are added to the simulation, the more computational resources are needed to simulate the boundary layer. If more than one prism layer is used, it is crucial to ensure a reasonable volume change from one cell to its neighbor [13]. Thus, two prism layers with a geometric growth is used in order to ensure a smooth transition. An approximation of the values needed for  $y^+$  were obtained from STAR-CCM+ by running a simulation using a uniform mesh. Table 8 shows the values obtained from a simple simulation.

Table 8. Average  $y^+$  parameters.

Parameter	Value	Units
$u_\tau$	24.7	$m/s$
$\rho$	5.98	$Kg/m^3$
$\mu$	$3.58 \times 10^{-5}$	$N \cdot s/m^2$

Based on the values shown above, the distance to the wall,  $y$ , can be approximated as shown below.

$$y = \frac{\mu y^+}{\rho u_\tau} = \frac{(3.58 \times 10^{-5} Pa - s)(300)}{\left(5.98 \frac{Kg}{m^3}\right) \left(24.7 \frac{m}{s}\right)} = 7.27 \times 10^{-5} m. \quad (37)$$

By choosing a stretching factor of 1.2, the total prism layer thickness can be calculated using the following equation,

$$PL_{th} = PL_{1st} \left( \frac{1-q^n}{1-q} \right), \quad (38)$$

where  $q$  is the prism layer stretching,  $n$  is the number of prisms, and  $PL_{1st}$  is the prism layer thickness of the first layer [13]. Based on information presented above, the total prism layer thickness is,

$$PL_{th} = 7.27 \times 10^{-5} m \left( \frac{1-1.2^2}{1-1.2} \right) = 1.60 \times 10^{-4} m. \quad (39)$$

The value presented above can be used as a starting point for choosing the total thickness of the prism layer as the values that it uses are averages. It has been determined that an absolute prism layer thickness of  $2 \times 10^{-4}$  m provides the best results for the simulations presented in this study.

The proper development of the mesh is an important aspect to have in mind since a mesh can successfully be created, but it can have a significant negative impact in the solution if it does not have a good cell quality [13]. Hence, the validity and quality of the volume mesh is important, and the tools to check these two parameters are already included in STAR-CCM+.

The face validity consists of the correctness of the face normal relative to the centroid of the cell. The following figure shows an example of a good and bad face validity.

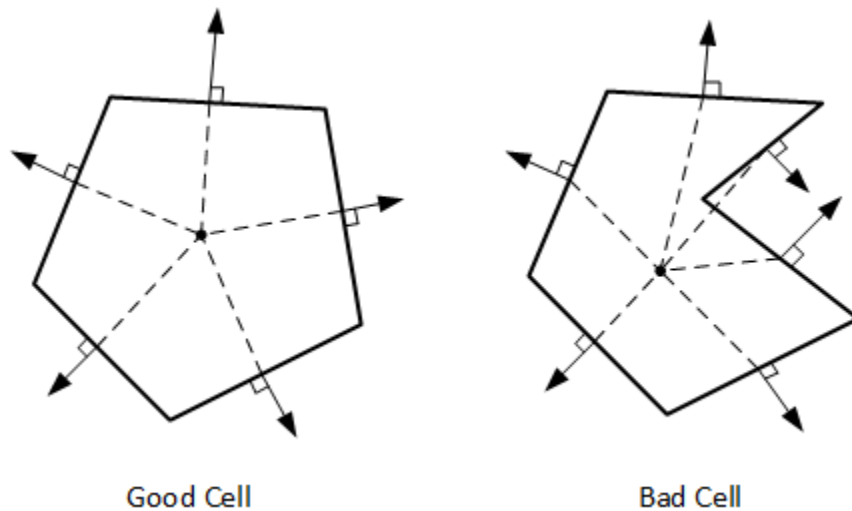


Figure 23. Example of a good and bad face validity [13].

When the face normal of the cell point outwards, a face validity of 1.0 is awarded, but when a value of less than 1.0 is awarded, it means that some of the faces are pointing inward towards the centroid. It is recommended that the face validity is greater than 0.9, and it is strongly advised to avoid values less than 0.8 [13]. The volume change is one of the parameters used to characterize a good from a bad cell. When the volume of a cell is equal or higher than its neighbors, a value of 1.0 is assigned. However, when a considerable change of volume from cell to cell is present, potential inaccuracies and instability in the solvers can result. Thus, it is recommended to have volume change

greater than  $10^{-3}$ , but a volume change of  $10^{-3}$  or less should be avoided [13]. Figure 24 shows an example of a good and bad cell.

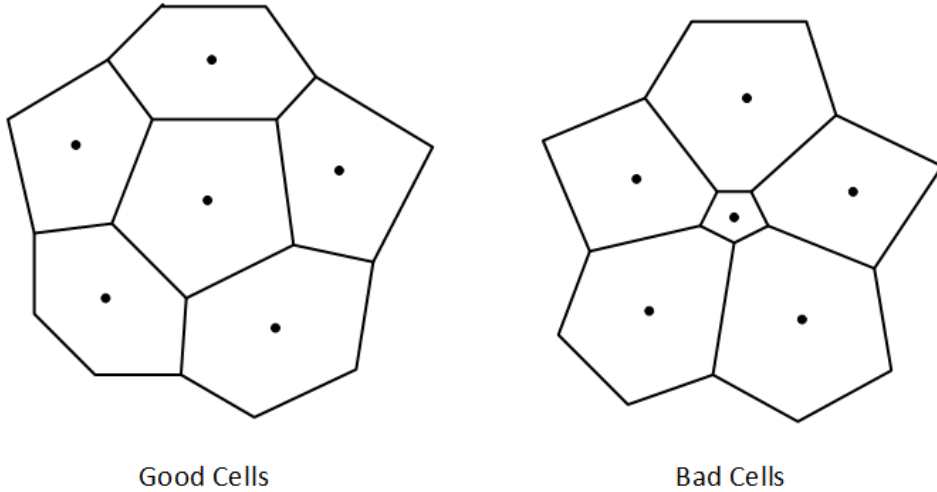


Figure 24. Example of good and bad cells [13].

#### 4.2.1 Grid Independence Study

As mentioned previously, the smaller the mesh size, the solution is more accurate. This means that the grid density is a trade-off between accuracy and available computational resources to obtain reasonable results [22]. The development of a grid independence study is crucial because it can help to select the adequate mesh size, and it can quantify the error introduced by the mesh selected. A systematic approach is provided in reference [23] where the Grid Convergence Index (GCI) method is used for the discretization error estimate, and it is the recommended method in ASME V&V 20-2009. This method is divided into 5 steps which are:

- Step 1: Define a representative mesh size. For this, the following relationship is used for two-dimensional grids,

$$h = \left[ \frac{1}{N} \sum_{i=1}^N (\Delta A_i) \right]^{\frac{1}{2}}, \quad (40)$$

where  $\Delta A_i$  is the area of the  $i^{th}$  cell,  $N$  is the total number of cells used for the simulation, and  $h$  is the representative mesh size.

- Step 2: Select three different spatial resolutions. It is important to note that the refinement factor must be 1.3 or greater. This refinement factor can be calculated using the following relationship,

$$r = \frac{h_{coarse}}{h_{fine}}. \quad (41)$$

Even though this refinement value is not obtained through a formal derivation, empirical experience obtained from other studies has shown this value is acceptable for most practical problems [23]. The three grid sizes chosen are  $h_1=2$  mm,  $h_2=3$  mm, and  $h_3=4$  mm.

- Step 3: Calculate the refinement factor for the 3 different grid sizes and the apparent or observed order,  $p$ ,

$$p = \frac{\left| \ln \left( \left| \frac{\varepsilon_{32}}{\varepsilon_{21}} \right| \right) + q(p) \right|}{\ln(r_{21})}, \quad (42)$$

where  $q(p)$  can be written as,

$$q(p) = \ln \left( \frac{r_{21}^p - s}{r_{32}^p - s} \right), \quad (43)$$

and

$$s = \text{sign} \left( \frac{\varepsilon_{32}}{\varepsilon_{21}} \right). \quad (44)$$

Here,  $h_1 < h_2 < h_3$ , and

$$r_{21} = \frac{h_2}{h_1}, \quad (45)$$

$$r_{32} = \frac{h_3}{h_2}, \quad (46)$$

$$\varepsilon_{32} = \varphi_3 - \varphi_2, \quad (47)$$

and

$$\varepsilon_{21} = \varphi_2 - \varphi_1. \quad (48)$$

It is important to note that if  $r$  is constant, then  $q(p) = 0$ , and  $\varphi_k$  represents the solution of the  $k^{th}$  grid. Equations (42), (43) and (44) can be solved using the fixed-point iteration method with an initial guess equal to the first term. The absolute value in Equation (42) is important to ensure extrapolation towards  $h=0$  [23].

- Step 4: Calculate the extrapolated values from the following equations,

$$\varphi_{ext}^{21} = \frac{(r_{21}^p \varphi_1 - \varphi_2)}{(r_{21}^p - 1)}, \quad (49)$$

and

$$\varphi_{ext}^{32} = \frac{(r_{32}^p \varphi_2 - \varphi_3)}{(r_{32}^p - 1)}. \quad (50)$$

- Step 5: The last step consists on calculating and reporting the error estimates. For this, an approximate relative error and an extrapolated relative error are used as shown below.

$$e_a^{21} = \left| \frac{\varphi_1 - \varphi_2}{\varphi_1} \right|, \quad (51)$$

and

$$e_{ext}^{21} = \left| \frac{\varphi_{ext}^{21} - \varphi_2}{\varphi_{ext}^{21}} \right|. \quad (52)$$

The fine Grid Convergence Index is calculated using the following relationship,

$$GCI_{fine}^{21} = \frac{Fs \cdot e_a^{21}}{r_{21}^p - 1}. \quad (53)$$

For the equation shown above, a Factor of Safety of 1.25 is used as it is recommended in ASME V&V 20-2009.

Since the mesh independence study only analyses how the mesh size influences the results obtained from the simulation, only a small timeframe is needed for the mesh independence study to determine the error introduced by the mesh size.

### 4.3 Initial Conditions

The initial conditions of the high- and low-pressure sections differ from each other. Since the rupture of the burst disk is not being modeled, a field function is created

instead. This field function is created to specify the pressure and temperature conditions of the high- and low-pressure sections right after the rupture disk bursts. The following table summarizes the initial conditions of the simulations covered in this study.

Table 9 . Initial pressure and temperature conditions.

Study	Geometry	High/low pressure sections [psi]	Temperature of high/low pressure sections [K]
Verification	Shock tube	1000/0.01	300/295
		1000/0.10	300/295
		1000/0.25	300/295
		1000/0.50	300/295
		1000/1.00	300/295
Validation/ Benchmark	Cylindrical test section with 0.75" intermediate section	~940/0.25	~300.84/~294.30
	Cylindrical test section with 1" intermediate section	~944/0.25	~302.18/~295.31
Parametric Study	Cylindrical test section with 0.5" intermediate section	~913/~0.1	~300.65/~294.47
	Cylindrical test section with 0.75" intermediate section	~940/0.25	~300.84/~294.30
	Cylindrical test section with 1" intermediate section	~944/0.25	~302.18/~295.31
	Annular test section with 1" intermediate section	900/0.25	300/295
		1000/0.25	300/295
		1100/0.25	300/295

#### 4.4 Boundary Conditions

The analysis of the boundary conditions of the CFD model is important since boundary conditions enable the flow to leave or enter the domain. STAR-CCM+ has several options for the simulation of the boundary conditions, but for the purpose of this study only two boundary conditions are covered: wall and symmetry plane boundary conditions.

The symmetry plane is a boundary option that consists of an imaginary plane. This boundary is assigned where the geometry and flow are symmetric with respect to the symmetry plane, and no boundary inputs are needed. The use of symmetry planes is beneficial from a computational standpoint since it can reduce the computational cost considerably as the computational domain is reduced. At this boundary, the flux across this plane and the gradient of other variables are zero [13]. The wall boundary condition is a more complex boundary compared to the symmetry plane since the interaction of the fluid on the wall has to be calculated and several options are available. The wall boundary consists of an impermeable surface that confines the fluid. Table 10 lists the different possible configurations for the wall boundary, and the options that were selected for the CFD model.

Table 10. Wall physics conditions.

Property	Options	Selected
Reference frame specification	Lab frame	Region reference frame
	Region reference frame	
	Local reference frame	
Shear stress specification	Non-slip	Non-slip
	Slip	
Tangential velocity specification	Fixed	Fixed
	Vector	
	Rotation rate	
	Local rotation rate	
Thermal specification	Adiabatic	Convection
	Heat flux	
	Heat source	
	Convection	
	Temperature	
	Environment	
Wall surface specification	Smooth	Smooth
	Rough	
User wall heat flux coefficient specification	Specify value	None

For the thermal specification, the lumped capacitance method is implemented, due to its simplicity and conservative method for transient heating and cooling problems, in order to determine if the heat transfer through the walls has a significant influence on the cooling of the gas during these transient scenarios. The lumped capacitance method consists of assuming the temperature of the solid is uniform at any time interval during the transient process [24]. For the walls of the out-of-pile HENRI test facility (refer to Figure 25), it can be assumed a steady-state conduction through the plane wall. By applying the energy equation, under steady-state conditions, the following energy balance relationship for the inner surface of the walls is obtained:

$$\frac{kA}{L}(T_{o,s} - T_{i,s}) = hA(T_{i,s} - T_{He}). \quad (54)$$

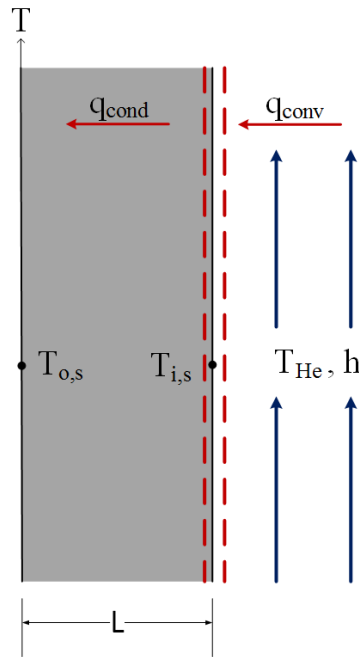


Figure 25. Temperature distribution across walls.

By rearranging the equation shown above, the following dimensionless number is obtained,

$$\frac{T_{o,s} - T_{i,s}}{T_{i,s} - T_{He}} = \frac{hL}{k} = Bi. \quad (55)$$

The dimensionless number shown above is the Biot number, and it can be used as indicator for the temperature distribution on a solid or in this case the walls in a transient process as shown in Figure 26.

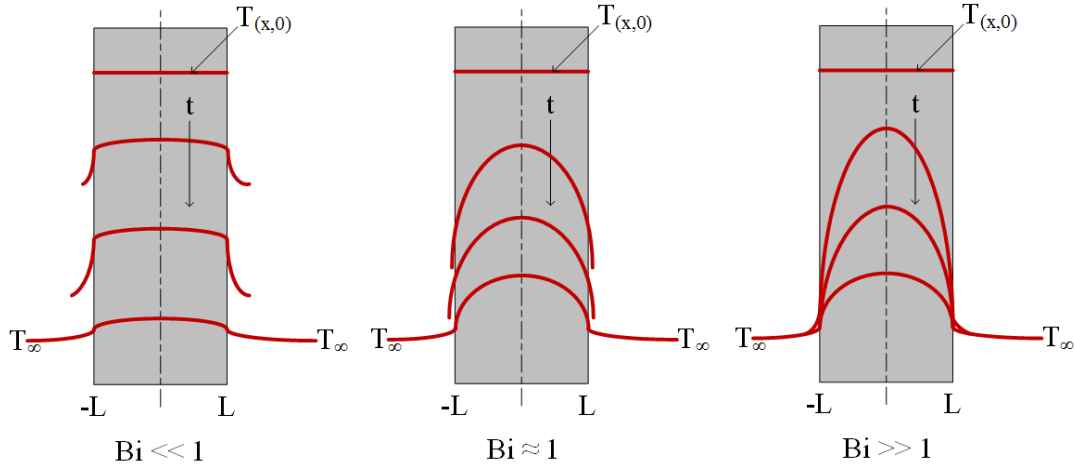


Figure 26. Temperature distribution for different Biot numbers in transient events [24].

If the Biot number is small ( $Bi \ll 1$ ), then the temperature distribution can be assumed uniform across the solid at any time internal during the transient process. If the Biot number is about or greater than 1, then temperature gradients across the solid can take place. Furthermore, the Biot number needs to be calculated in order to determine if the convection process that takes place on the walls removes significant or negligible amount of energy. This analysis is approached by calculating the convection term,  $h$ , in one of the CFD models used for the benchmark of the simulation. The convection term is calculated as follows,

$$h = \frac{Nu k_{He}}{L_c}, \quad (56)$$

where the Nusselt number,  $Nu$ , is calculated using the Dittus-Boelter equation,

$$Nu = 0.023 Re_D^{0.8} Pr^n. \quad (57)$$

Here,  $n$  has a value of 0.3 for cooling and 0.4 for heating. Combing the Biot number equation with the Dittus-Boelter and the convection equation, it yields,

$$Bi = \frac{0.023 Re_D^{0.8} Pr^{0.3} k_{He}}{k_s}, \quad (58)$$

where  $k_{He}$  is the thermal conductivity of the gas,  $k_s$  is the thermal conductivity of the solid, which is SS-304 for this study, and  $Pr$  is the Prandtl dimensionless number. The Biot number was calculated using a line probe placed along the cylindrical test section, since it is the section of interest, and the total time length of the simulation is 5 ms. The following figure shows the average Biot number obtained from the cylindrical test section of the out-of-pile HENRI test facility.

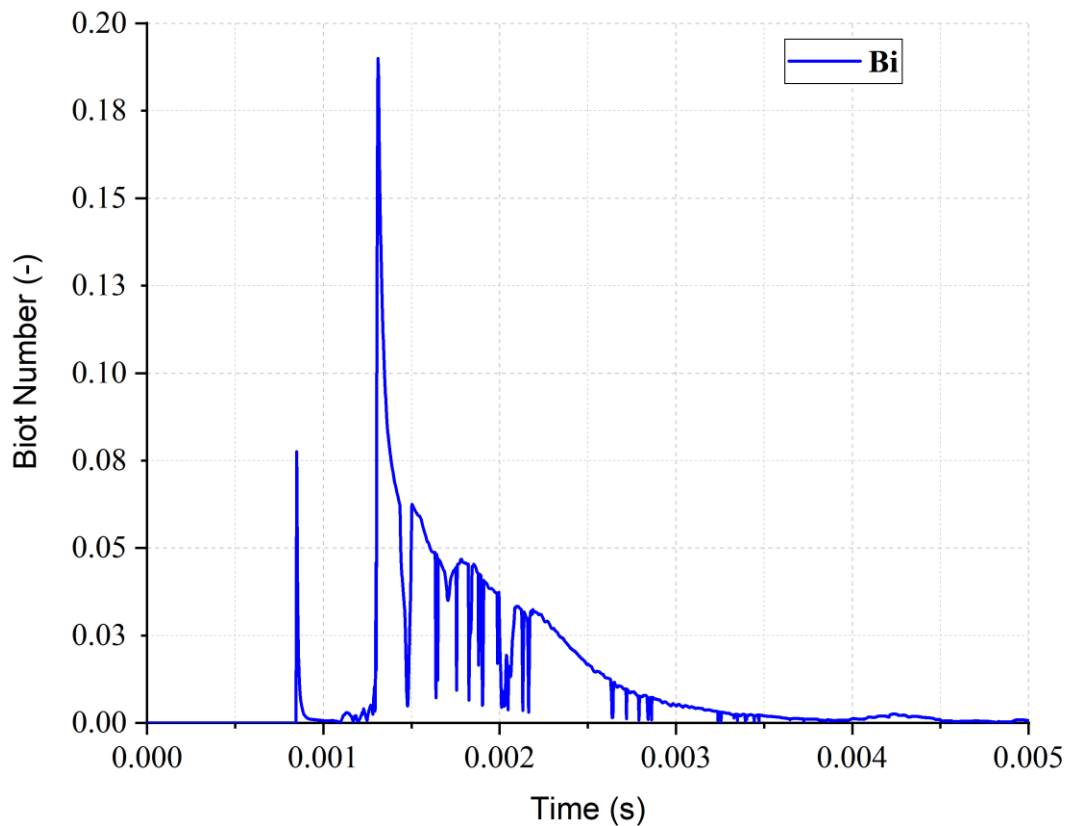


Figure 27. Biot number from cylindrical test section of the out-of-pile HENRI test facility.

Based on the Biot number shown in Figure 27, the temperature across the walls of the out-of-pile HENRI test facility can be assumed to be close to uniform. This means that transient process inside of the out-of-pile HENRI test facility is considerably faster than

the time required to have significant heat loss due to convection. At early stages of this study, an adiabatic boundary condition was used; however, the residual values of the simulations did not reach acceptable levels. Technical support from STAR-CCM+ advised to use a very low convective heat transfer value instead of an adiabatic condition. For the purpose of this study, a small heat transfer coefficient of 5 W/m<sup>2</sup>-K was assumed. Upon a closer examination, this assumption is not ideal for sections where the helium moves at a slower velocity. Further information about this is covered in Section 6 of this document.

## 4.5 Physics Models

### 4.5.1 Flow Solver

STAR-CCM+ has three flow solvers available: viscous, segregated, and coupled flow solver. To determine the most adequate flow solver, reference [13] states that the coupled solver “yields more robust and accurate solutions in compressible flow, particularly in the presence of shocks”. By selecting the coupled flow solver, it solves simultaneously the conservation of mass, energy and momentum as a vector of equations using a numerical time-marching approach. The momentum equation provides information about the velocity field, the continuity equation helps to calculate the pressure, and the equation of state evaluates the density [13]. The governing equations in Cartesian integral form are:

$$\frac{\partial}{\partial t} \int_V \bar{W} dV + \oint \left[ \bar{F} - \bar{G} \right] \cdot da = \int_V \bar{H} dV. \quad (59)$$

The vectors of the equation shown above are defined as,

$$\bar{W} = \begin{bmatrix} \rho \\ \rho v \\ \rho E \end{bmatrix}, \quad (60)$$

$$\bar{F} = \begin{bmatrix} \rho v \\ \rho vv + pI \\ \rho vH + pv \end{bmatrix}, \quad (61)$$

$$\bar{G} = \begin{bmatrix} 0 \\ \bar{T} \\ \bar{T} \cdot v + \dot{q}'' \end{bmatrix}, \quad (62)$$

$$\bar{H} = \begin{bmatrix} S_u \\ f_r + f_g + f_p + f_u + f_{\omega} + f_L \\ S_u \end{bmatrix}, \quad (63)$$

where,

$$E = H - \frac{P}{\rho}, \quad (64)$$

$$H = h + \frac{|v|^2}{2}, \quad (65)$$

and,

$$h = C_p T. \quad (66)$$

Here,  $\rho$  is the density,  $v$  is the velocity,  $E$  represents the total energy per unit mass,  $P$  is the pressure,  $\bar{T}$  is the viscous stress tensor,  $\bar{H}$  is the vector of body forces,  $H$  is the total enthalpy,  $C_p$  is the specific heat capacity, and  $T$  represents the temperature [13].

In order to improve the simulation's capability of capturing shock waves and contact discontinuities, the Advection Upstream Splitting Method – Flux Vector Splitting or AUSM+FVS scheme was chosen for evaluating inviscid fluxes. This scheme was used in some CFD simulations covered in references [25] and [13] for better accuracy of

pressure and density discontinuities. Also, reference [13] suggests using this scheme for flows that fall within the high supersonic regime. The accuracy can be further improved by selecting the MUSCL 3rd-order/CD convection scheme which is a mixture between the 3rd-order central-differencing reconstruction scheme and the MUSCL 3rd-order upwind scheme [13]. Since using a 3<sup>rd</sup>-order upwind scheme increases the computational cost of the simulation, a 2<sup>nd</sup>-order discretization is used instead in an attempt to reduce computational time. However, if the accuracy of the simulation needs to be increased even further, it is then recommended to activate this option.

The convergence of the simulations was improved by setting an explicit relaxation factor of 0.68, and the minimum absolute pressure was adjusted to 1 Pa as suggested in some case studies provided in reference [13]. In addition, the AMG linear cycle type is changed from V-Type to F-Type with 0 pre sweeps, 3 post sweeps, and 2 max levels. This adjustment is implemented as the F-cycle converges faster than the V-cycle [13].

#### 4.5.2 Time Solver

Due to the large number of unknown equations, it is preferably desired to choose the implicit unsteady model. A second order temporal scheme resolution was chosen for the simulations in order to perform second order forward prediction by application of the last time-step results. The time-step chosen for the simulations was estimated using the following equation,

$$CFL = \frac{v\Delta t}{\Delta x}, \quad (67)$$

where, *CFL* represents the Courant–Friedrichs–Lewy number, which is a mathematical condition needed for convergence while solving partial differential equations using a numerical approach,  $\Delta t$  is the time-step,  $\Delta x$  is the grid size, and  $v$  is the velocity of the information that traverses a grid cell [26]. The grid size is obtained based on the minimum mesh size imposed on the geometry, the courant number is chosen by the

user, and the velocity can be estimated based on the velocity of the fluid. It has been identified that a time-step of  $1 \times 10^{-7}$  s with a convective CFL timestep control provides the best results in terms of convergence.

#### 4.5.3 Material Selection

The material selection provides several options, but due to the fact that the fluid under analysis is in gaseous state, it is advised to select the “gas” option. Also, it is important to consider that at high-flow speed regimes, fluids behave different. For the purpose of this study, the fluid, helium, is assumed to be thermally perfect. Thus, the ideal gas option is selected. For most of the material properties, such as molecular weight, specific heat, and turbulent Prandtl number, their values were setup constant; however, the dynamic viscosity and the thermal conductivity were calculated using the Sutherland’s law. By selecting this option, the dynamic viscosity and the thermal conductivity become a function of temperature. The Sutherland’s law for dynamic viscosity is,

$$\frac{\mu}{\mu_0} = \left( \frac{T}{T_0} \right)^{3/2} \left( \frac{T_0 + S}{T + S} \right), \quad (68)$$

and for thermal conductivity is,

$$\frac{k}{k_0} = \left( \frac{T}{T_0} \right)^{3/2} \left( \frac{T_0 + S}{T + S} \right), \quad (69)$$

where  $S$  is the Sutherland constant,  $\mu_0$ ,  $T_0$ , and  $k_0$  are the reference viscosity, temperature, and thermal conductivity [13]. It is claimed that the Sutherland’s law increases the accuracy of the results with small percentage error for a wide range of temperatures [25].

#### 4.5.4 Turbulence Model

The DNS, LES, and DES turbulence models were discarded in this study due to the large computational resources that they require. From the RANS turbulence models, k-epsilon is one of the most widely used model [27], and it was one of the turbulence model considered for this study. However, for some simulations with very large pressure discontinuities and complex geometries covered in this study, the numerical residuals did not reach acceptable levels when the low-pressure section has a pressure below 1 psi. Alternatively to k-epsilon, k-omega is a two-equation turbulence model which is the second most widely used two-equation turbulence model [27]. The main difference between the k- $\epsilon$  and k- $\omega$  is that the second term for k- $\omega$  is the specific turbulent dissipation rate  $\omega$  instead of the turbulent dissipation rate  $\epsilon$ . The Menter SST k-omega turbulence model is the adopted turbulence model for this study as this turbulence model is able to perform simulations for the HENRI system with an absolute pressure as low as 0.25 psi. In addition, this turbulence model has incorporated the advantages of the k-epsilon and k-omega turbulence models. For more information regarding this, refer to Section 2.6 of this document.

An all  $y^+$  wall treatment is selected along the turbulence model since the simulation is able to well resolve the viscous sublayer at some points of the simulation, and high  $y^+$  values are also observed during most of the simulation. It is important to note that a document released by the NASA, reference [28], states that changing the value of  $a_1$  to 0.355 improves the predictions of shock separated flows, and reference [13] suggests to select QCR (quadratic) as the consecutive option.

## 4.6 Stopping Criteria

The simulations covered in this study required only two stopping criteria: a maximum physical time and a maximum number of inner iterations per time step. The maximum physical time was chosen based on the information needed to adequately compare the computed results against the experimental data obtained from the out-of-pile HENRI test facility. Since the timeframe of interest is within the first 5 milliseconds of the

pressurization, the maximum simulation time cannot be less than this timeframe. It was identified that 40 and 10 milliseconds of physical time for the cylindrical and annular test section, respectively, provides enough information to analyze and compare the data.

In order to identify the adequate number of inner iterations per time step, it is recommended to observe the output residuals. For this, the first time-steps of the simulations ran for several inner iterations. By doing this, the continuity, energy, x- and y-momentum, turbulence kinetic energy, and turbulence dissipation rate residuals have enough inner iterations to reach their plateau. At the beginning of the simulations, it was required to run each time-step for at least 250 inner iterations to ensure the numerical residuals reach acceptable levels. After a few hundred time-steps, the number of inner iterations was reduced to 175 in an attempt to reduce computational cost.

#### 4.7 Post processing Setup

The data collected from the out-of-pile HENRI test facility was pressure and temperature, but the facility did not have instrumentation that was able to measure the density directly. Since the atomic density is one of the most important parameters to analyze while pressurizing the gas chamber, information pertaining the pressure, temperature, and density evolution in the gas chamber and driver tank needs to be collected. For data collection, probe points were used.

For the shock tube simulations, 10 probe points were placed along the geometry, as shown below, to quantify the pressure and track the displacement of the incident and reflected shock waves along the shock tube.

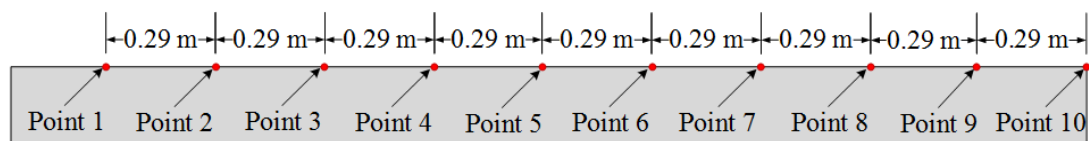


Figure 28. Probe points in shock tube.

For the cylindrical test section, 7 probe points were used. Since one of the objectives of this study is to determine the CFD model's capability to reproduce real-world phenomena, it is imperative to compare experimental data against the results obtained from the CFD model. Thus, the probe points were placed at the same position as the instrumentation ports shown in Figure 16. The following figure display the position of the probe points.

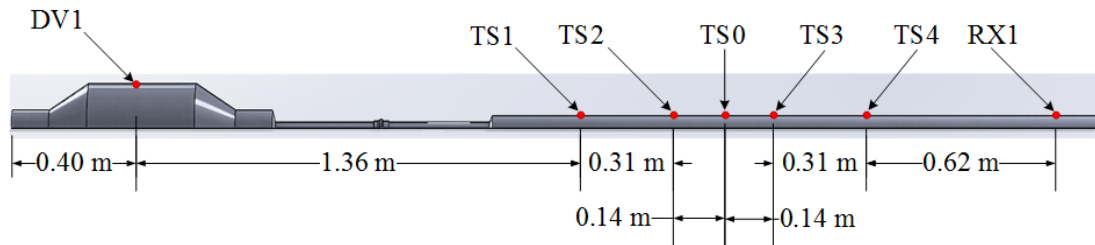


Figure 29. Position of probe points in test facility with cylindrical test section.

The test facility with an annular test section uses the same number of probe points since the instrumentation ports are distributed in a similar manner as the cylindrical test section. A schematic of the probe points of the test facility with annular test section is shown below.

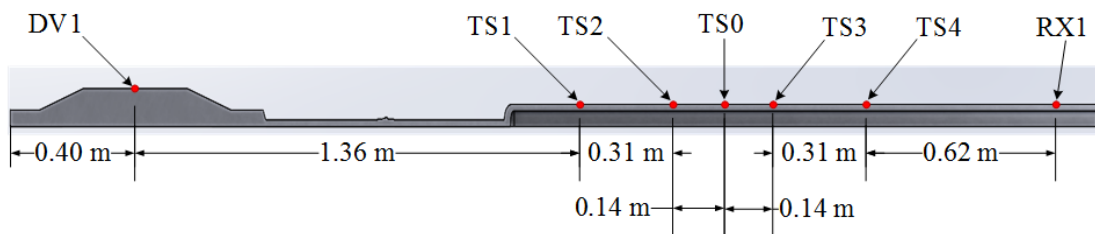


Figure 30. Position of probe points in test facility with annular test section.

## 5 EXPERIMENTAL BENCHMARK

One of the major concerns of this study is to assess the accuracy of the CFD model to recreate real-world phenomena. The Standard for Verification and Validation in Computational Fluid Dynamics and Heat Transfer (ASME V&V 20-2009) provides a

systematic approach to verify and validate simulations. The approach presented in reference [6] aids to quantify the simulation's capability to represent phenomena that takes place in the real world. For this, a code verification and solution verification must be addressed first. According to reference [6], the validation comparison error,  $E$ , is defined as,

$$E = \delta_S - \delta_D, \quad (70)$$

where  $\delta_S$  is the error in the solution value and  $\delta_D$  is the error in the experimental data. These two errors can be defined as,

$$\delta_S = S - T, \quad (71)$$

and

$$\delta_D = D - T. \quad (72)$$

Here,  $T$  represents the true value, which is unknown,  $S$  is the simulation solution value, and  $D$  is the experimental data value. Based on Equation (70), the validation comparison error is the combination of the simulation and experimental results. It is important to note that “the ‘truth’ is the value of a quantity of interest defined by the observer and is an abstraction” [6]. The experimental data obtained from the out-of-pile HENRI test facility is used to benchmark the CFD models of this study.

## 6 RESULTS AND DISCUSSION

Prior to discussing the results obtained in this study, it is necessary to provide a preliminary overview of the tests performed and their relevance. The objective of this study is to develop a CFD model for the HENRI system with an annular gas chamber. In order to provide enough evidence that the CFD model provides adequate results,

three studies have to be completed. The first study consists of verifying the CFD software is capable of numerically solving accurately the physics models incorporated in the simulation. The numerical solution is compared against a known solution. For the purpose of this study, an analytical solution for a shock tube is compared against the results obtained from simulating a shock tube using STAR-CCM+. The second study consists of the grid independence study which analyzes the error introduced by the mesh chosen for the simulations. The third study consists of the validation of the CFD model. Since the simulation is expected to recreate the physics that take place in the HENRI system, the CFD model is compared against experimental data to determine the degree to which it can accurately simulate real-world phenomena. For this approach, the CFD model is benchmarked against experimental data obtained from the out-of-pile HENRI test facility with a cylindrical test section. The fourth study focuses on a parametric study on the HENRI facility with an annular test section. This parametric study consists of analyzing the influence of the system's geometry and the driver tank pressure to reach the desired atomic density level within the annular test section of the HENRI system. Also, this parametric study is intended to identify relationships or patterns that can be used to have a better understanding of the system's performance.

## **6.1 Verification: Shock Tube Analysis**

The analysis of a shock tube is used in this study to verify that the physics models chosen can simulate supersonic flow, and to ensure the differential equations can be solved correctly using the chosen numerical solver configuration. One of the advantages of analyzing a shock tube is that an analytical solution can be obtained from the equations covered in Section 2.2. In this analysis, the effects of friction and heat transfer are neglected. Also, the cross-sectional area of the shock tube is assumed to be uniform.

One of the main concerns of this study is to maintain numerical stability throughout the entire simulation. However, it was identified that choosing very low pressures for the simulations result in numerical instability. It is important to identify the minimum

possible pressure for the simulations since the low-pressure section of the out-of-pile HENRI test facility operates at a pressure near vacuum conditions. STAR-CCM+ is unable to perform simulations with pressures near vacuum conditions. Thus, to identify an adequate low pressure for the simulations with the chosen physics models and the numerical solver settings, five simulations are analyzed in this section. These five simulations have the same settings, but the low-pressure section of the shock tube is different. For this study, the five different low pressures considered for this study are: 1, 0.5, 0.25, 0.1, and 0.01 psi.

Since x-t diagrams are commonly used in shock tube analyses, this study uses it to compare the displacement of the incident wave and contact surface obtained from an analytical and numerical approach. Figure 31 through Figure 35 plot the incident shock wave and the density wave, or contact surface, displacement along the shock tube for the five different pressure scenarios.

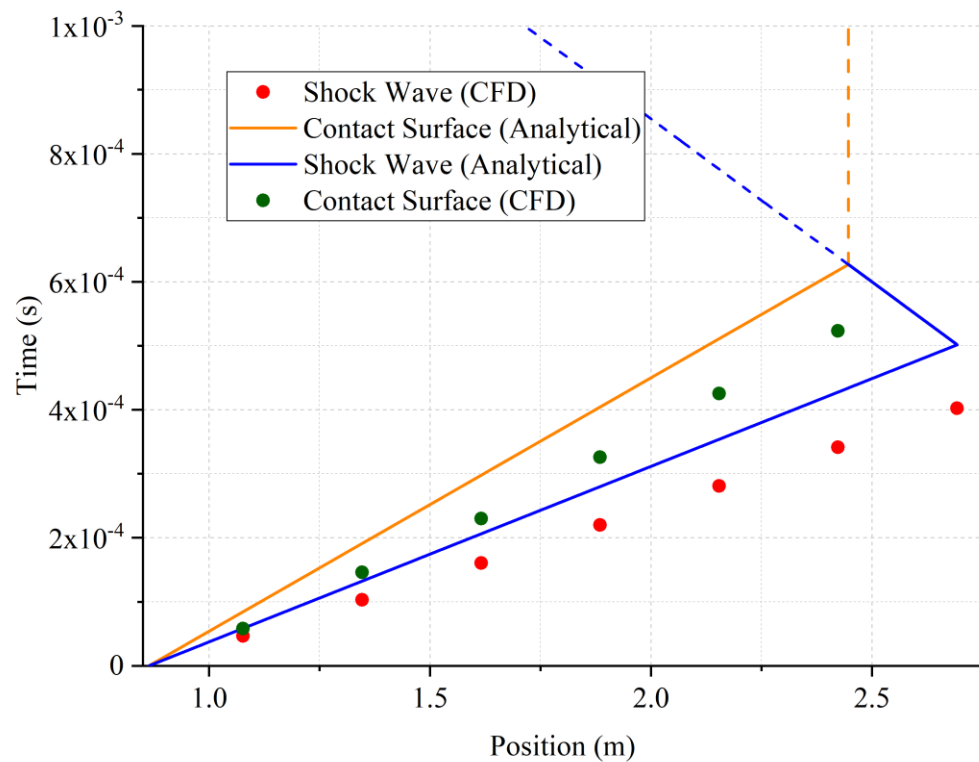


Figure 31. x-t diagram of shock tube with initial pressures of 1000 and 0.01 psi.

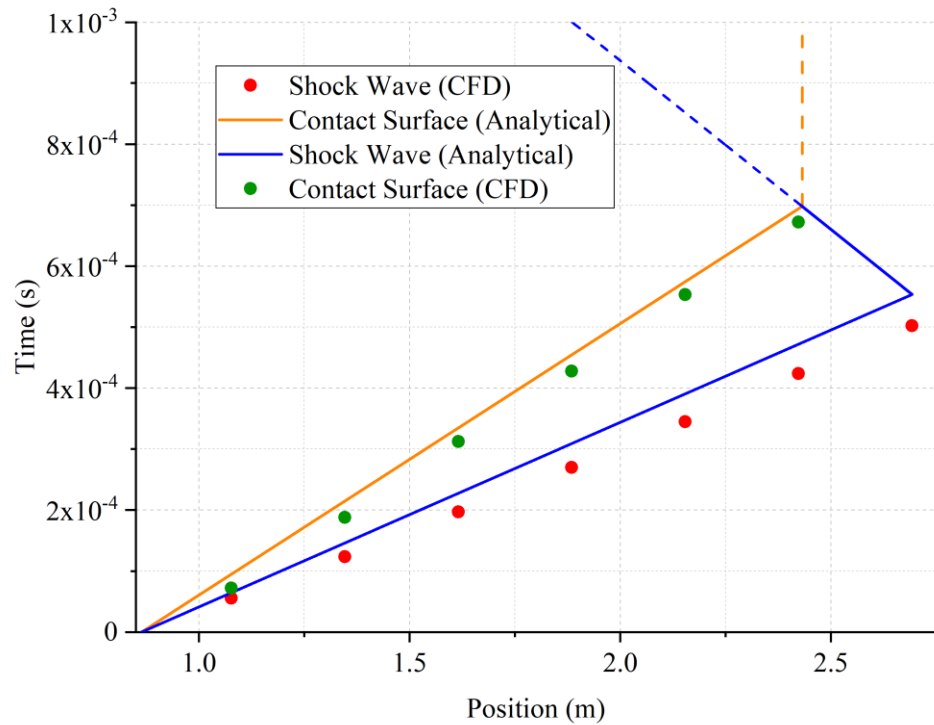


Figure 32. x-t diagram of shock tube (1000/0.1 psi).

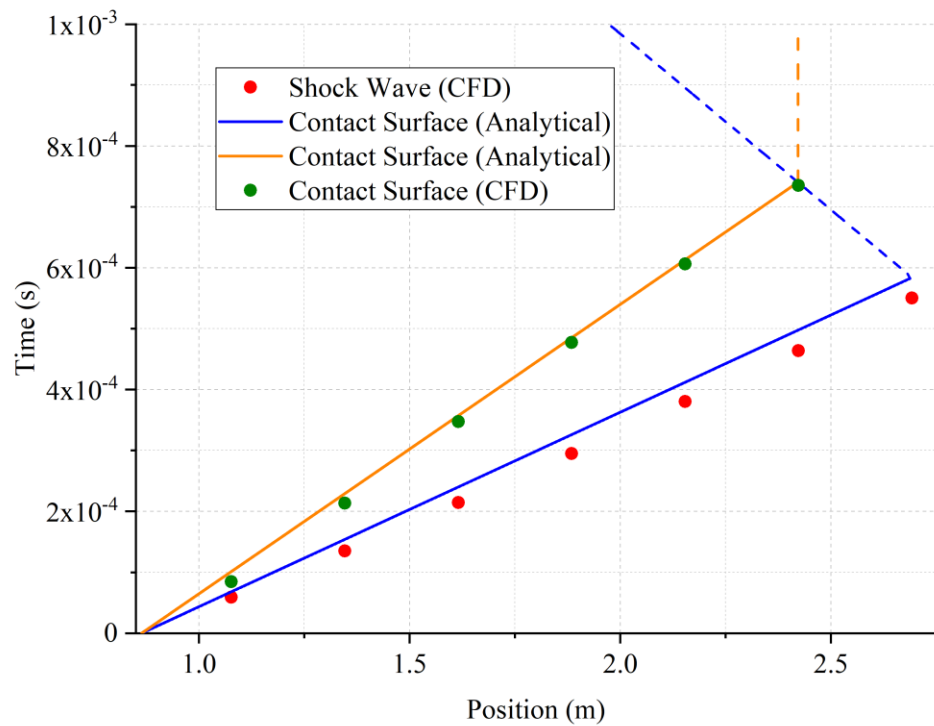


Figure 33. x-t diagram of shock tube with initial pressures of 1000 and 0.25 psi.

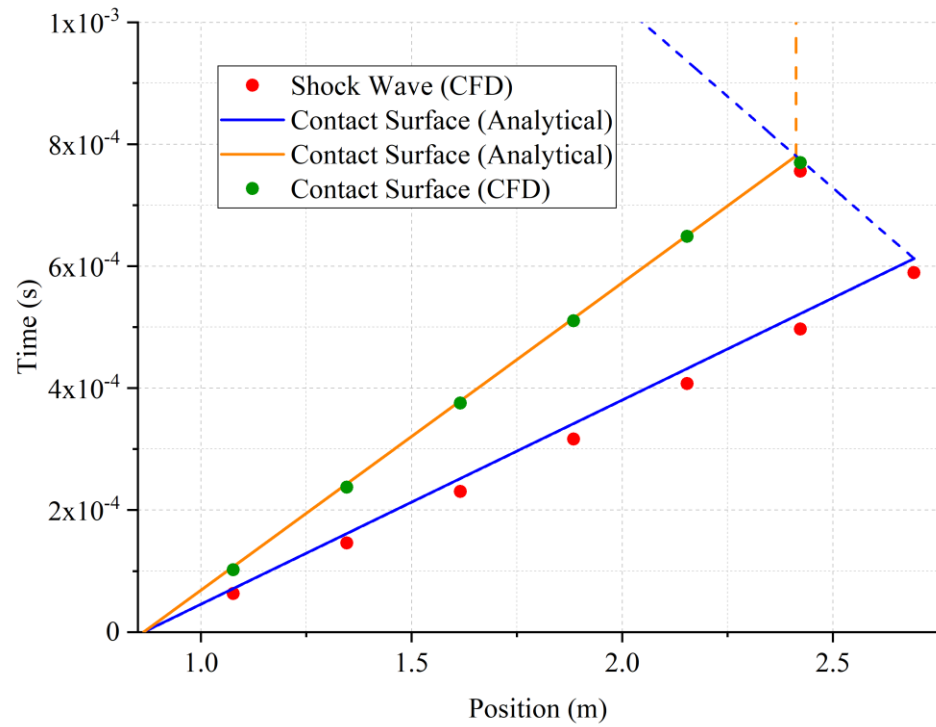


Figure 34. x-t diagram of shock tube with initial pressures of 1000 and 0.5 psi.

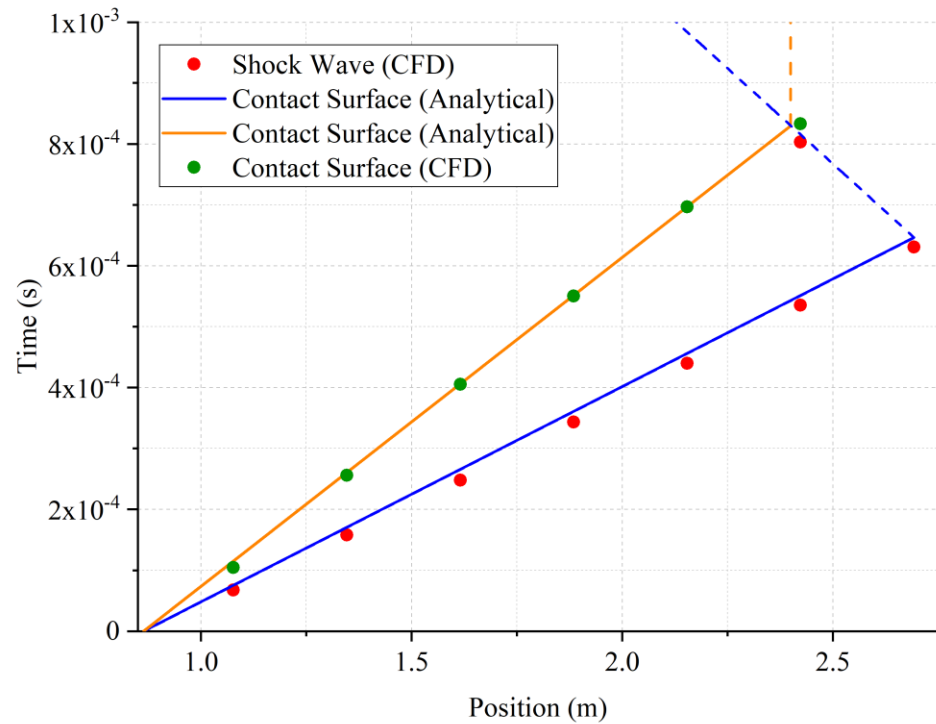


Figure 35. x-t diagram of shock tube with initial pressures of 1000 and 1 psi.

As it can be seen in Figure 31Figure 35, the solutions obtained from the CFD simulations deviate from the analytical solution as the pressure is lowered. This indicates that with the chosen numerical solver setting, the CFD model is unable to simulate pressures near vacuum without introducing large errors. This issue was addressed by quantifying the error associated with the absolute pressure, temperature and velocity of the shock wave. The following table shows the results and their respective error.

Table 11. Average pressure, temperature and velocity of incident shock waves.

Driven pressure	Incident shock wave parameters	Analytical solution	Numerical solution	$\pm$ Error
0.01 psi	Absolute pressure	0.16 psi	0.24 psi	52.55%
	Temperature	1454.18 K	1992.28 K	37.00%
	Velocity	3646.51 m/s	4545.73 m/s	24.66%
0.10 psi	Absolute pressure	1.31 psi	1.54 psi	17.26%
	Temperature	1238.61 K	1337.25 K	7.96%
	Velocity	3304.42 m/s	3626.00 m/s	9.73%
0.25 psi	Absolute pressure	2.94 psi	3.12 psi	6.17%
	Temperature	1137.88 K	1131.29 K	0.58%
	Velocity	3132.06 m/s	3298.57 m/s	5.32%
0.50 psi	Absolute pressure	5.34 psi	5.34 psi	0.00%
	Temperature	1057.19 K	1035.78 K	2.02%
	Velocity	2987.00 m/s	3074.61 m/s	2.93%
1.00 psi	Absolute pressure	9.55 psi	9.42 psi	1.31%
	Temperature	973.69 K	926.64 K	4.83%
	Velocity	2829.36 m/s	2872.55 m/s	1.53%

As shown in Table 11, the overall percentage error increases as the pressure of the driven section of the shock tube is lowered. In order to identify an acceptable low-pressure value for the simulations, the following two aspects were considered:

1. the percentage error of the absolute pressure, temperature, and velocity of the incident shock wave must be below 10%, and
2. the lowest pressure should be considered, as long as the results have a percentage error of less than 10%, in order to reproduce the same results.

Based on the two requirements shown above, a pressure of 0.25 psi provides the best overall results. Thus, the simulations presented in this study use a pressure of 0.25 psi in lieu of a pressure near vacuum.

## 6.2 Grid Independence Study

The grid independence study is a useful approach to quantify the error that it is introduced by the mesh. The use of a coarse mesh can have its pros and cons. One of the pros of using a coarse mesh is that the computational cost of a simulation can be reduced significantly. In other words, the computational cost of a simulation is strongly affected by the number of cells used to compute the results of a simulation. One of the major concerns of using a very coarse mesh is the accuracy of the results. The use of a coarse mesh can reduce the accuracy of the results, and it can potentially affect the convergence of the simulation. These two issues can be addressed if the mesh is reduced. The smaller the mesh, the more accurate the solution is. However, the use of a very small mesh can increase the computational cost of the simulation. Thus, it is important to identify a mesh that can provide reasonable results without increasing the computational cost of the simulation considerably. The mesh used in this study is believed to provide reasonable results without increasing the computational cost too much. The question to be asked is how much error is being introduced by the mesh selected for this study. The quantification of this error can be addressed by using the GCI method. As stated in Section 4.2.1, three different mesh sizes,  $h_1=2$  mm,  $h_2=3$  mm, and  $h_3=4$  mm, were chosen for this analysis. The geometry used for this analysis was based on the out of pile HENRI test facility with an annular test section and an intermediate tube diameter of 1". From the three simulations created, the following information was retrieved regarding the mesh:

Table 12. Statistics for coarse, medium, and fine meshes.

Statistics	Range	Coarse (4 mm)	Medium (3 mm)	Fine (2 mm)
Number of cells		21939	35364	67283
Face validity	0.90≤0.95	0%	0%	0%
	0.95≤1.00	100%	100%	100%
Volume change	0.01≤0.10	2.398%	1.920%	0.926%
	0.10≤1.00	97.608%	98.080%	99.074%

The information presented in Table 12 can help us to determine if bad cells were created. However, the results presented indicate that the quality of the mesh is very good as the cells have a face validity of 100% for the three types of mesh, and over 97% of the volume change for the cells ranged from 0.10 to 1.00.

Once the mesh quality is assessed, the error of the CFD models is calculated by comparing the results obtained from the three different simulations. Here, the pressure and temperature of the annular test section is used for this analysis. Figure 36 shows the pressure and temperature in the annular test section at four different points at t=1 ms.

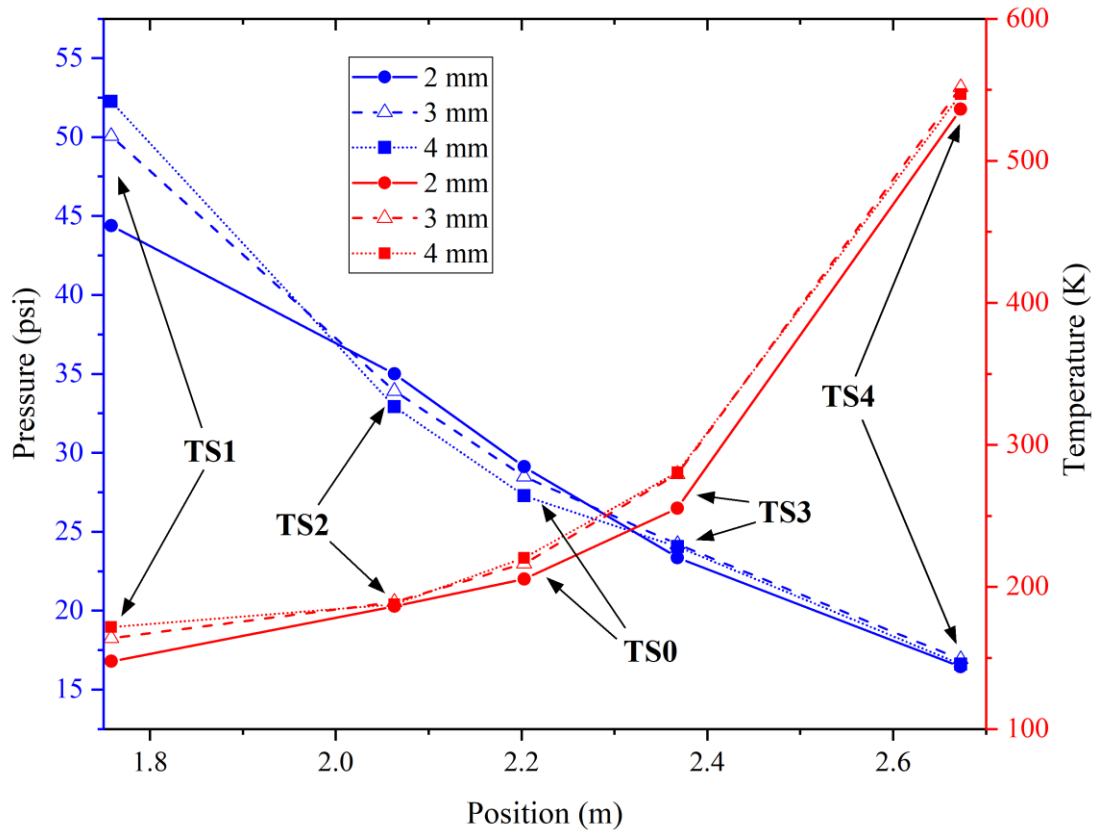


Figure 36. Pressure and temperature recorded in the test section at time 1 ms. using 3 different grid sizes.

By implementing the equations shown in Section 4.2.1, an extrapolated solution was obtained with its respective error bars as shown below.

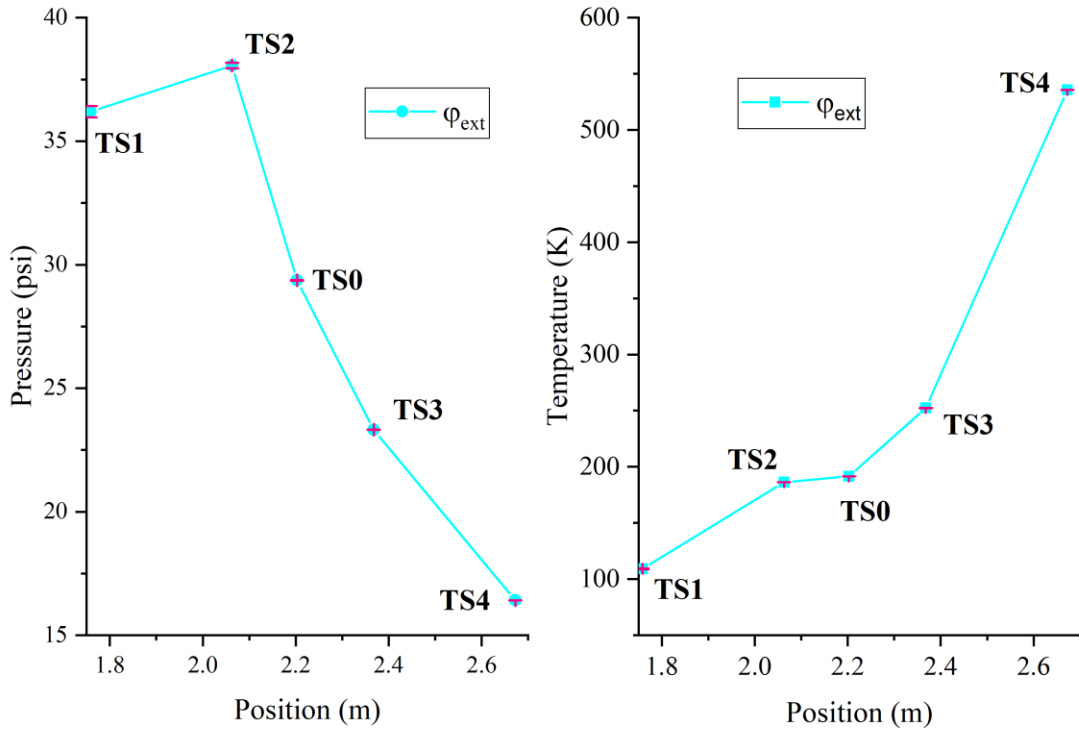


Figure 37. Extrapolated solutions for the pressure (left) and temperature (right) of the annular test section.

A summary of the values obtained in this study is shown in Table 13 and Table 14.

Table 13. GCI pressure results from grid independence study.

$r_{12}$	$r_{32}$	$\phi_1$	$\phi_2$	$\phi_3$	$p$	$\phi_{ext}$	$e_a$	$e_{ext}$	GCI [%]
1.50	1.33	29.11	28.49	27.28	3.02	29.37	0.02	0.01	1.11
1.50	1.33	44.39	50.06	52.25	1.30	36.19	0.13	0.23	23.08
1.50	1.33	35.00	33.92	32.92	0.75	38.06	0.03	0.08	10.91
1.50	1.33	23.35	24.20	24.06	8.05	23.32	0.04	0.00	0.18
1.50	1.33	16.44	16.92	16.61	7.82	16.42	0.03	0.00	0.16

Table 14. GCI temperature results from grid independence study

r <sub>12</sub>	r <sub>32</sub>	ϕ <sub>1</sub>	ϕ <sub>2</sub>	ϕ <sub>3</sub>	p	ϕ <sub>ext</sub>	e <sub>a</sub>	e <sub>ext</sub>	GCI [%]
1.50	1.33	205.52	216.52	220.51	1.43	191.55	0.05	0.07	8.50
1.50	1.33	147.65	164.06	171.79	0.88	109.15	0.11	0.35	32.59
1.50	1.33	186.34	189.45	187.83	7.76	186.20	0.02	0.00	0.09
1.50	1.33	255.50	279.39	280.74	5.26	252.29	0.09	0.01	1.57
1.50	1.33	536.25	551.72	546.90	7.79	535.56	0.03	0.00	0.16

### 6.3 Validation: Experimental Benchmark

The experimental benchmark or validation of the CFD model is performed by simulating experimental results using a CFD model with the numerical solver settings and assumptions adopted in this study. The validation process is of upmost importance for the development of CFD models as this process can indicate how close the numerical approach is able to reproduce real-world phenomena. Ideally, the CFD model should bear resemblance to experimental data. However, several factors can affect the results obtained from the simulation. Therefore, it is crucial to identify those factors and quantify their influence on the results. This quantification process is addressed as follows: one of the limitations encountered on the verification process is the inability to simulate very low pressures, especially pressures near vacuum. Even though experiments were conducted using pressures near vacuum, a pressure of 0.25 psi was chosen in lieu. The question to be asked is how this assumption affects the overall pressure evolution within the HENRI system. To address this question, three simulations were compared against each other. All the initial conditions are the same for the three simulations, but they differ from each other as their test and extension sections have a different pressure. These simulations were based on the initial conditions of the 1" intermediate section scenario shown in Table 9. The following table summarizes the initial conditions of the three simulations.

Table 15. Initial conditions for three simulations used for the low-pressure analysis.

Geometry	High/low pressure sections [psi]	Temperature of high/low pressure sections [K]
Cylindrical test section with 1" intermediate section	944/0.25	302.18/295.31
	944/0.50	302.18/295.31
	944/1.00	302.18/295.31

Based on these initial conditions, the following pressure plots from the cylindrical test section were obtained.

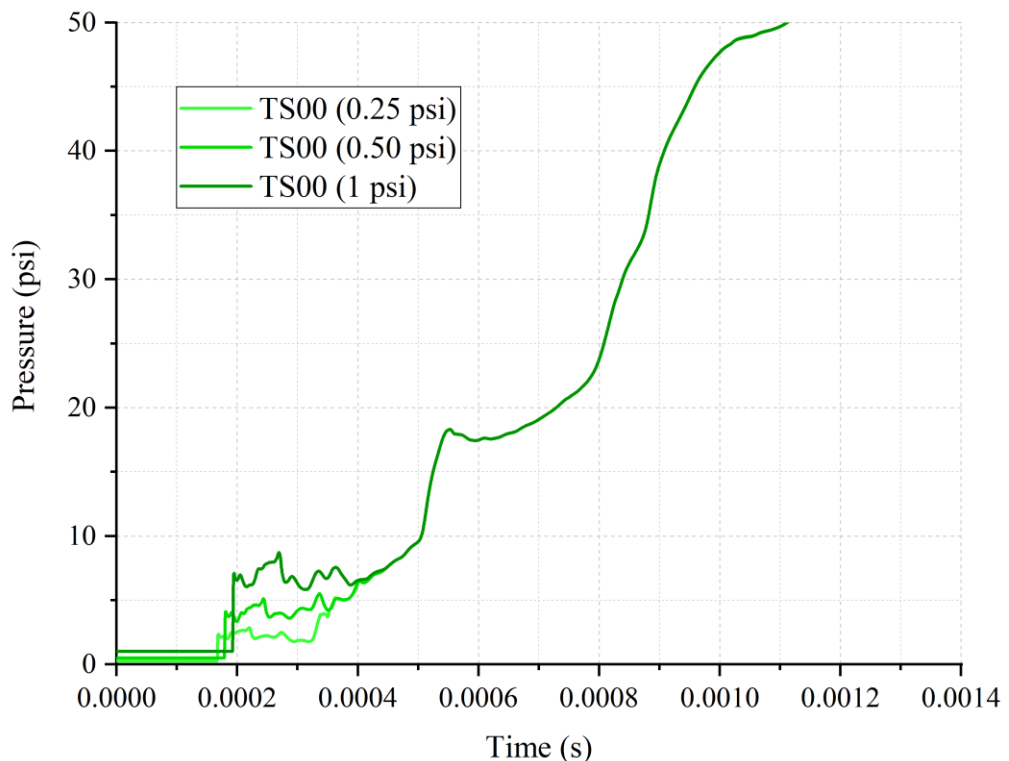


Figure 38. Pressure evolution for probe point TS00 using different low pressures.

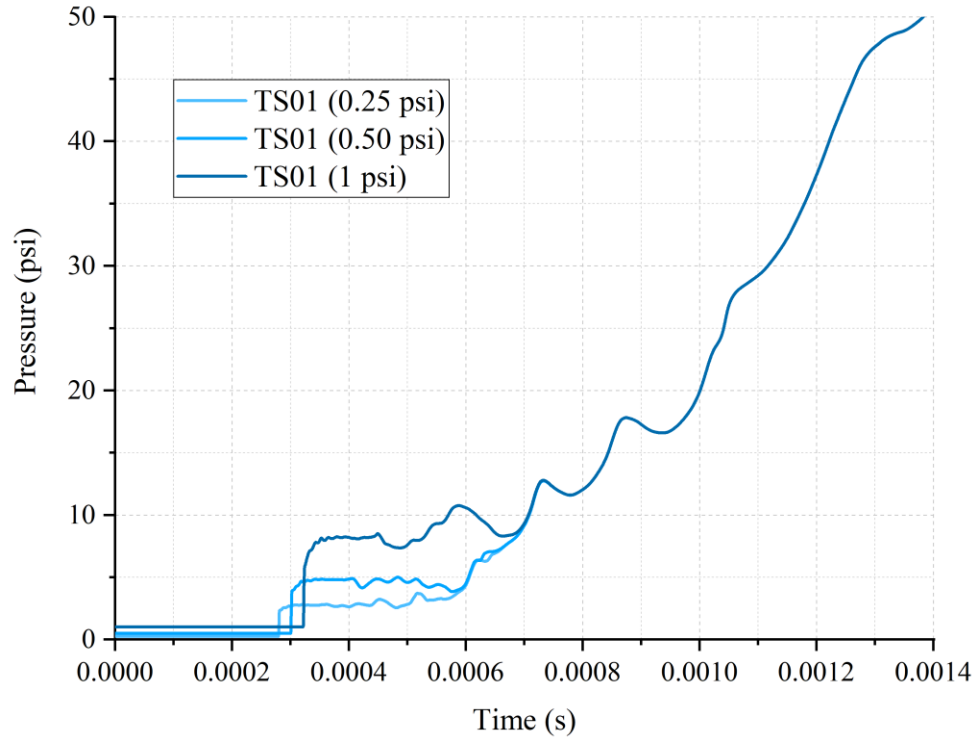


Figure 39. Pressure evolution for probe point TS01 using different low pressures.

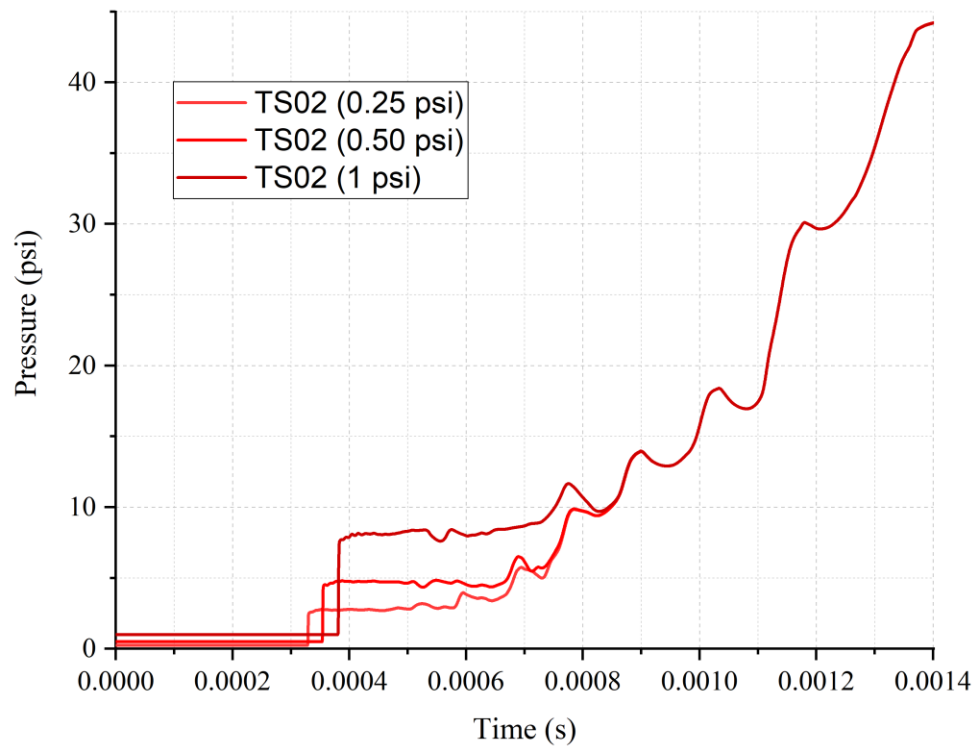


Figure 40. Pressure evolution for probe point TS02 using different low pressures.

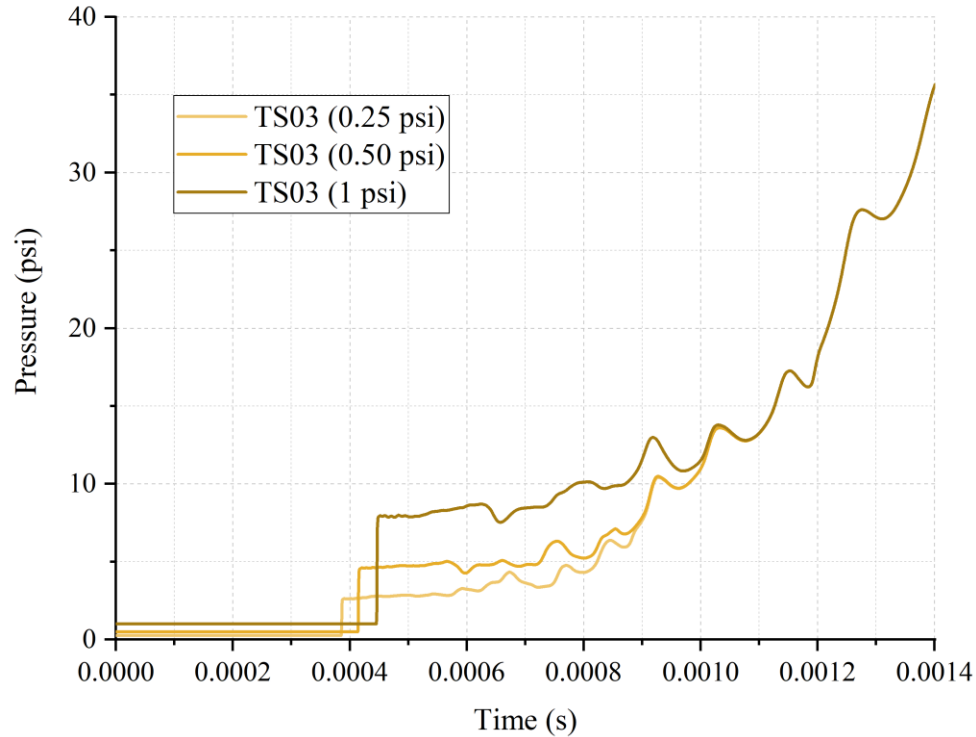


Figure 41. Pressure evolution for probe point TS03 using different low pressures.

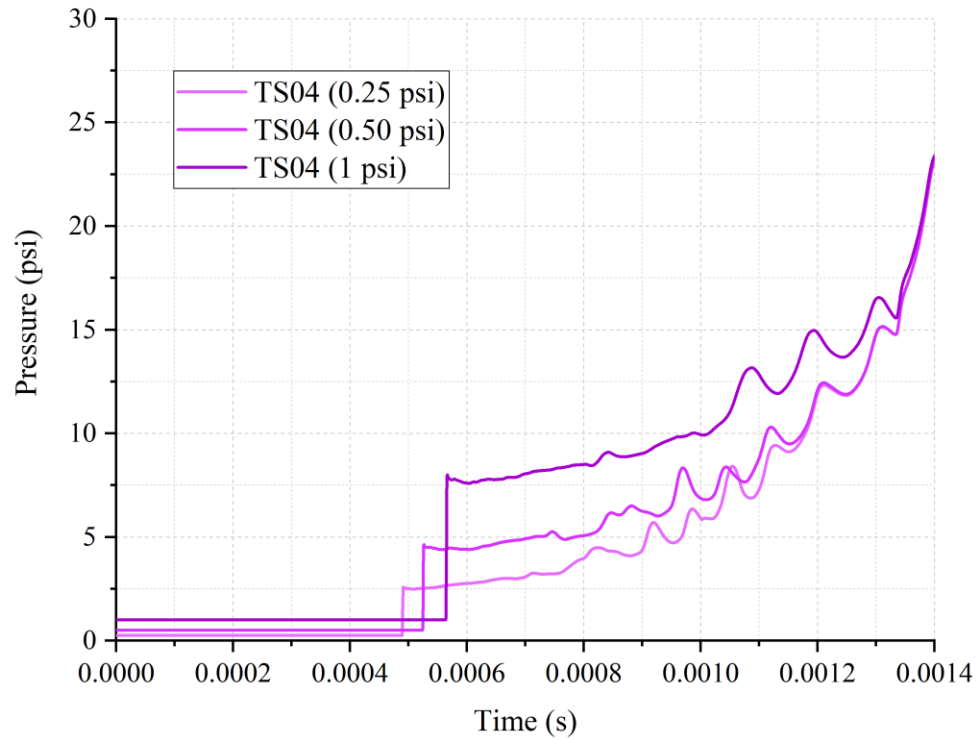


Figure 42. Pressure evolution for probe point TS05 using different low pressures.

As shown in Figure 38 though Figure 42, the pressure evolution of the three simulations differ from each other within the first 1.4 milliseconds. One clear and expected difference is the intensity of the shock wave, which are the sharp pressure steps. However, after the first 1.4 ms, the pressure evolution of the three simulations follow the same trend. This means that even though the low-pressure section has different initial pressure levels within the first 1.4 ms, the pressurization process is the same afterwards.

Now that the low-pressure assumption was addressed, the overall pressure, temperature, and time difference between experimental and CFD results should be compared against each other. For this process, two different scenarios were simulated. The first simulation for the validation or benchmark process consists of a cylindrical test section connected to the driver tank with an intermediate section diameter of 0.75". The initial conditions of the experiment are summarized in Table 9.

The first comparison addressed is the pressure evolution within the cylindrical test section. Here, only the first 40 milliseconds were simulated. It is important to note that the instrumentation used in the out-of-pile HENRI test facility has some uncertainty associated to it. The response time of the sensors also influences the experimental data. For instance, the response time of the Omega sensors is about 1 ms, whereas the PCB sensors have a rise time of 1  $\mu$ s [29] [30]. The following figure shows the comparison between experimental and CFD results for the low-pressure section.

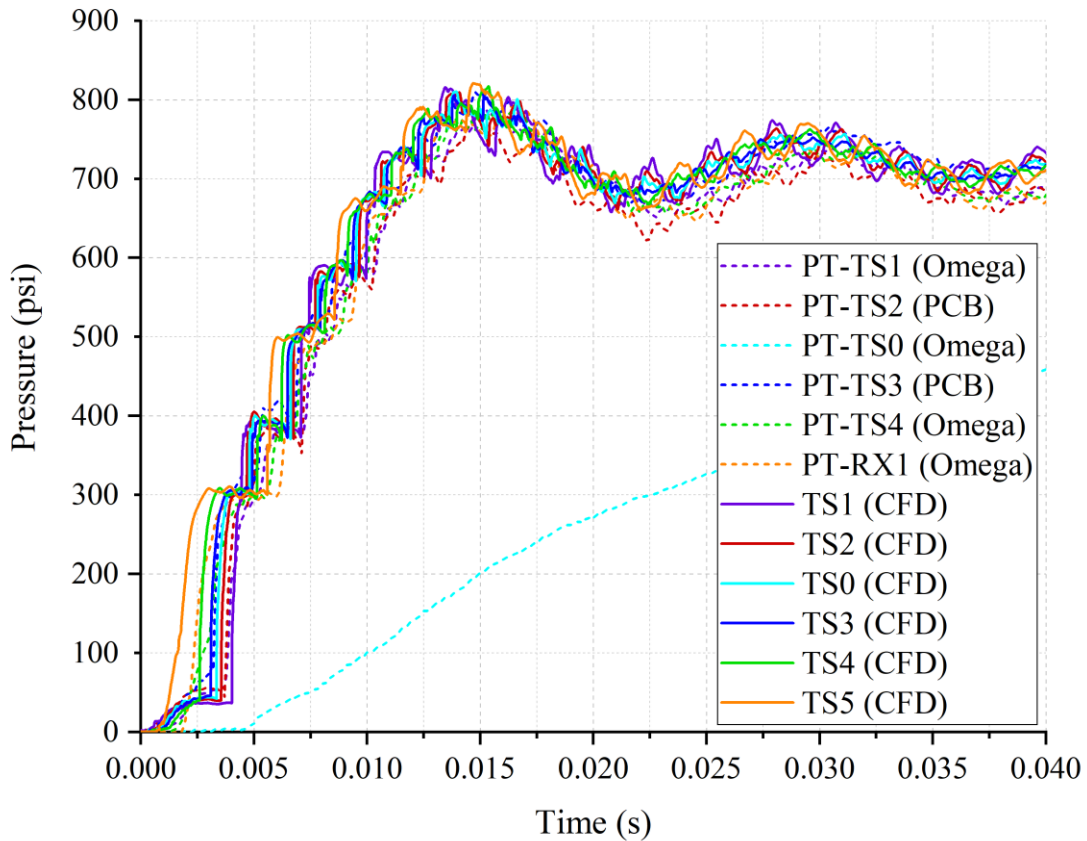


Figure 43. Pressure evolution inside of the cylindrical test section of the experiment and CFD model using an intermediate section tube diameter of 0.75".

Prior to discussing the results obtained any further, it is important to note that the pressure recorded by the sensor PT-TS0 differs from the other sensors, as shown above. Upon closer examination, it was found that the sensor was not working properly. Thus, a comparison between the data collected by this sensor and the calculated by the probe point TS0 cannot be performed.

To make a better judgment of the difference between the experimental and numerical results, Figure 44 only compares the measured and calculated pressure evolution at the top (TS1) and bottom (TS4) of the test section.

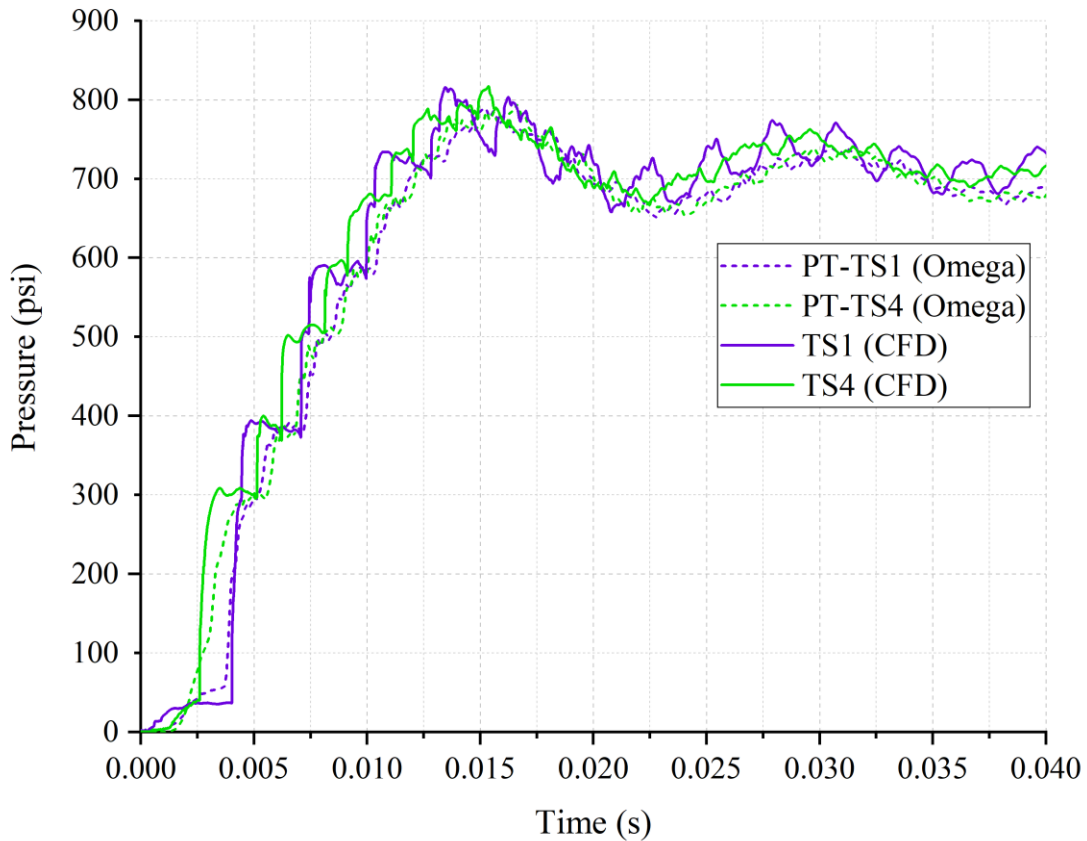


Figure 44. Pressure evolution at the top (TS4) and bottom (TS1) of the cylindrical test section of the out-of-pile HENRI test facility using an intermediate section tube diameter of 0.75".

Overall, the calculated and measured pressure evolution in the test section of the out-of-pile HENRI system seem to follow the same pattern within the first 40 milliseconds. To quantify their difference, the calculated maximum pressure and time to reach the maximum pressure are compared to that of the experimentally measured values as seen in Figure 45 and Figure 46.

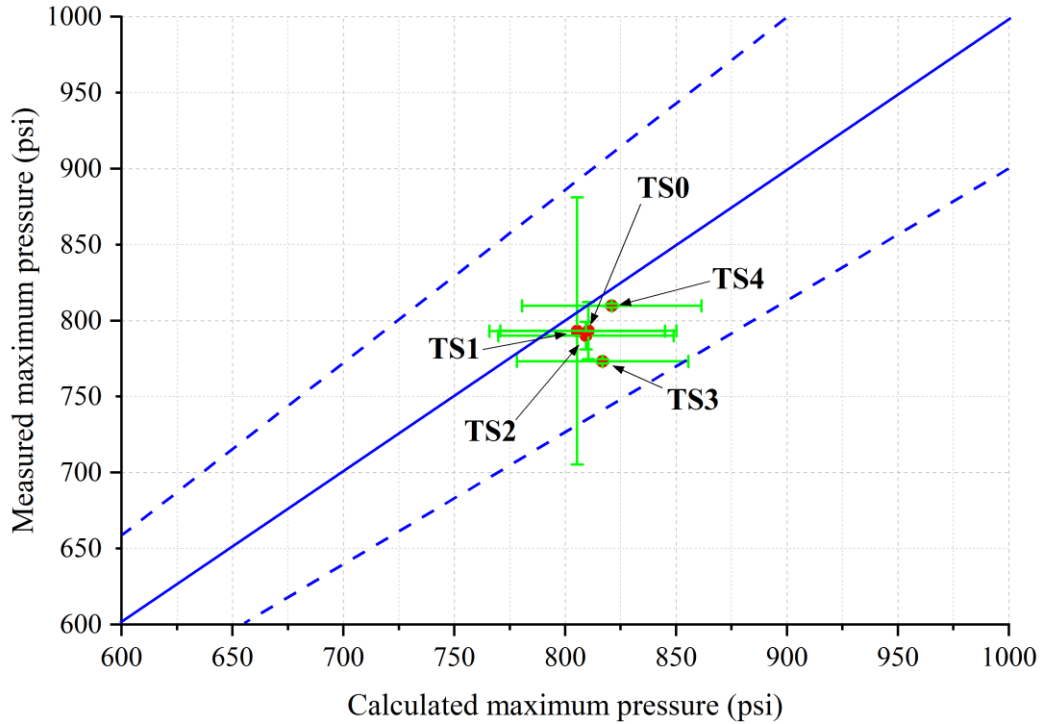


Figure 45. Comparison of measured vs. calculated maximum pressure for the out-of-pile HENRI test facility with intermediate section tube diameter of 0.75".

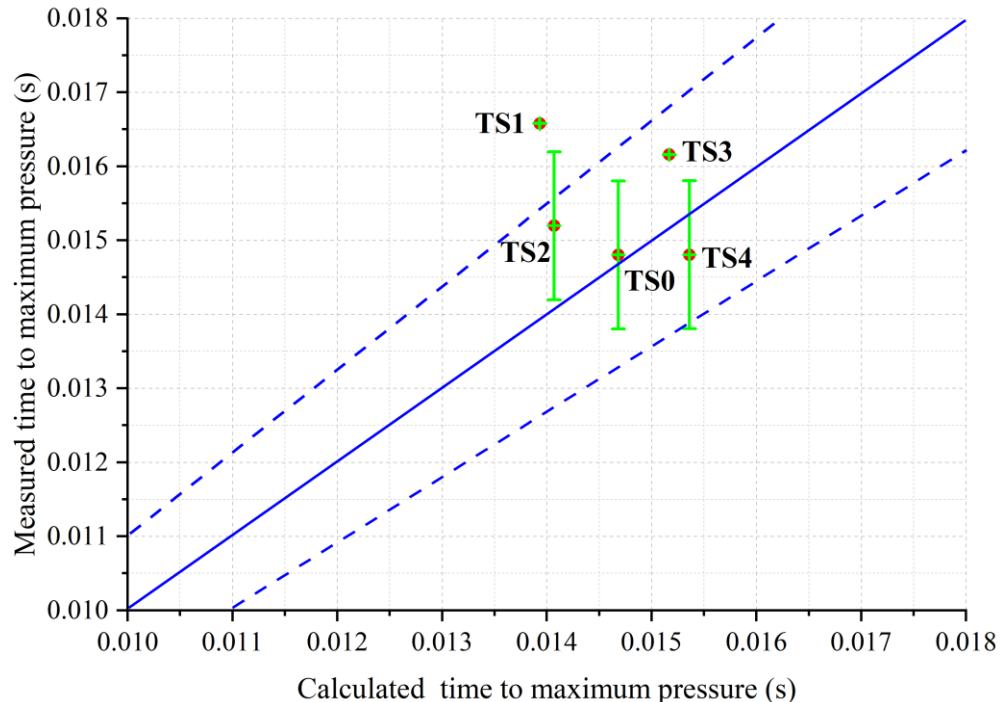


Figure 46. Comparison of measured vs. calculated time to maximum pressure for the out-of-pile HENRI test facility with intermediate section tube diameter of 0.75".

The solid line shown in Figure 45 and Figure 46 represents a 1 to 1 correlation between the measured and calculated values, and the dotted lines delimit the  $\pm 10\%$  difference. Upon close inspection, the pressure calculated by the CFD model is slightly underestimated, but the difference falls within the  $\pm 10\%$  range. For the time to maximum pressure, the calculated timing is mostly overestimated, but the difference is not considerably significant.

The depressurization of the driver tank was also considered in this study, and the comparison between the measured and calculated pressure is shown below.

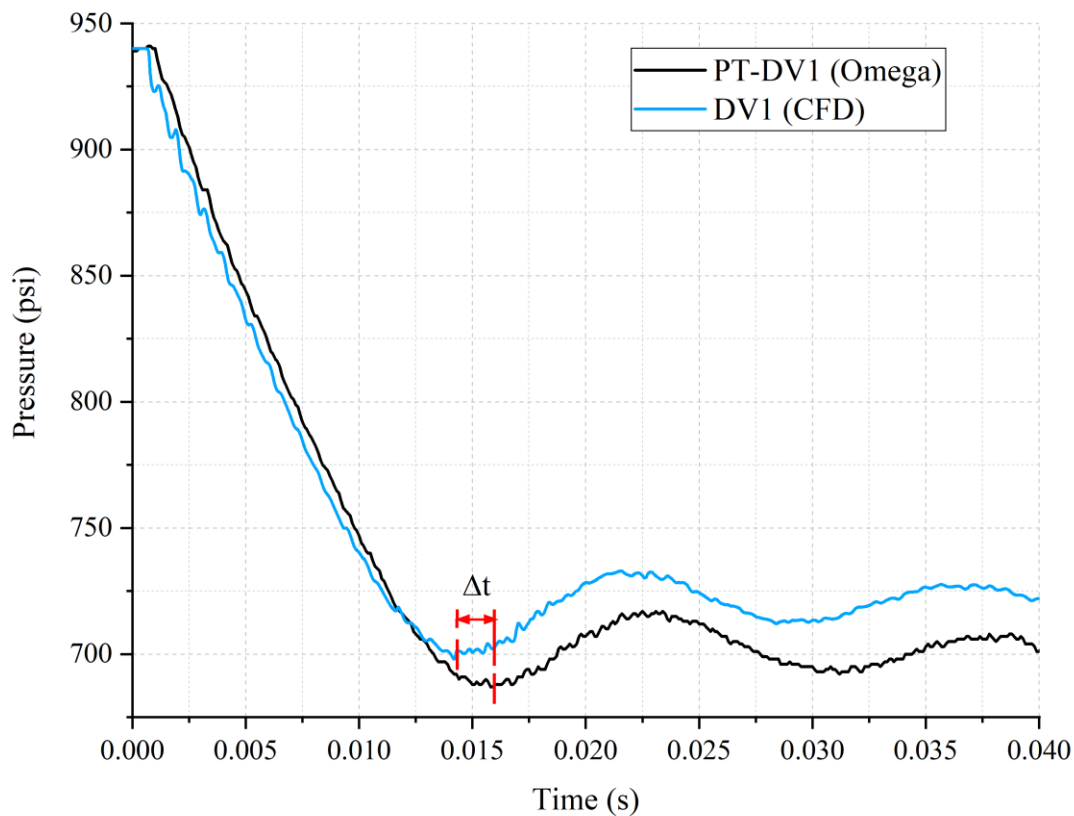


Figure 47. Pressure evolution inside of the driver tank of the experiment and CFD model using an intermediate section tube diameter of 0.75".

The difference between the CFD and experimental data is considerably noticeable when comparing the depressurization of the driver tank. As discussed in the Section 4.4 of this document, the heat transfer in the test section was assumed to be negligible;

however, it is possible that this is not the case for the driver tank as the helium moves slower compared to the helium that moves in the test section. If the gas moves slower, then it is possible that heat transfer due to convection is significant in this section. Since a low heat transfer coefficient was assumed, the driver tank takes longer to cool down, and the pressure will drop at a lower rate. This can possibly explain why the driver tank pressure oscillates at a higher level than the calculated pressure. The time difference between the calculated and measured pressure can be attributed to the response time of the pressure transducers. As stated previously, an Omega pressure transducer sensor was used in the driver tank. The response time of the sensor is about 1 ms. The phase difference of both oscillations is about 1.64 ms, which means that the response time of the instrumentation is the major contributor of the time difference between the experimental and numerical results presented in Figure 47.

In addition to the pressure, the measured and calculated temperature were compared against each other. Figure 48 and Figure 49 show the temperature evolution inside the low-pressure section of the out-of-pile HENRI test facility.

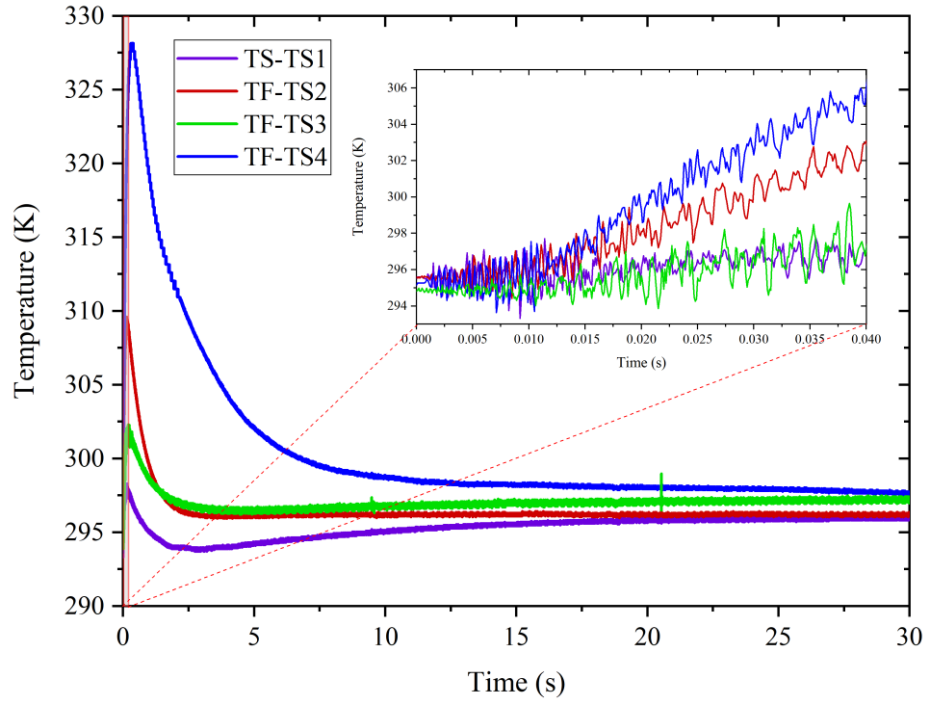


Figure 48. Temperature evolution inside of the cylindrical test section obtained through the HENRI test facility using an intermediate section tube diameter of 0.75".

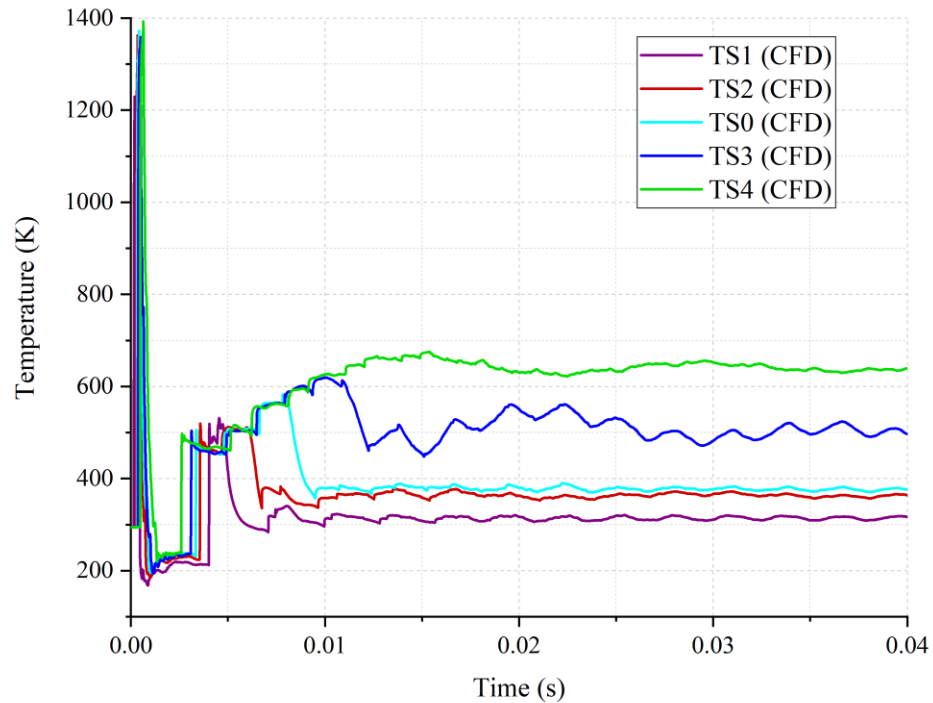


Figure 49. Temperature evolution inside of the cylindrical test section obtained through the HENRI test facility using an intermediate section tube diameter of 0.75".

The temperature evolution for both, measured and calculated, are completely different from each other. This can be attributed to the response time of the instrumentation. The peak temperatures from the simulation for all probe points were recorded within 1 ms, whereas the peak temperature recorded by the thermocouples took place within 1 sec. Another difference is the temperature amplitude. The peak temperatures for the simulation have an amplitude of about 1400 K. However, the thermocouples recorded different peak temperatures that do not exceed the 330 K. Due to these differences, a direct comparison of the temperature evolutions could not be done. Even though the temperatures are different, it is important to note that the stratification is consistent with the experimental data. Since density is a function of pressure and temperature, the analysis of the stratification can provide an estimate of the difference of density along the test section.

The second simulation or scenario to compare consists of using a tube diameter of 1" for the intermediate section. Using the same initial conditions as stated in Table 9 for this configuration, the following pressure evolution data was obtained for the low-pressure section.

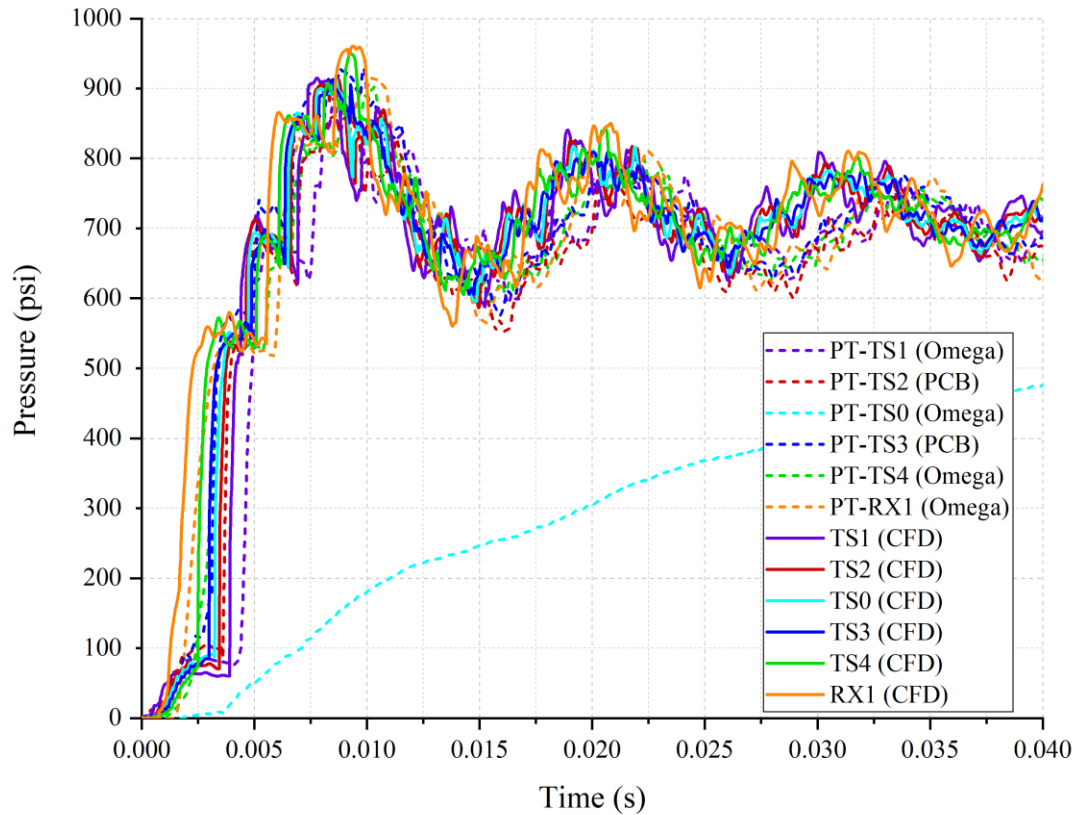


Figure 50. Pressure evolution inside of the cylindrical test section of the experiment and CFD data using an intermediate section tube diameter of 1".

Again, to provide a better comparison between the experimental and numerical results, Figure 51 shows the pressure evolution at the top (TS4) and bottom (TS1) of the cylindrical test section.

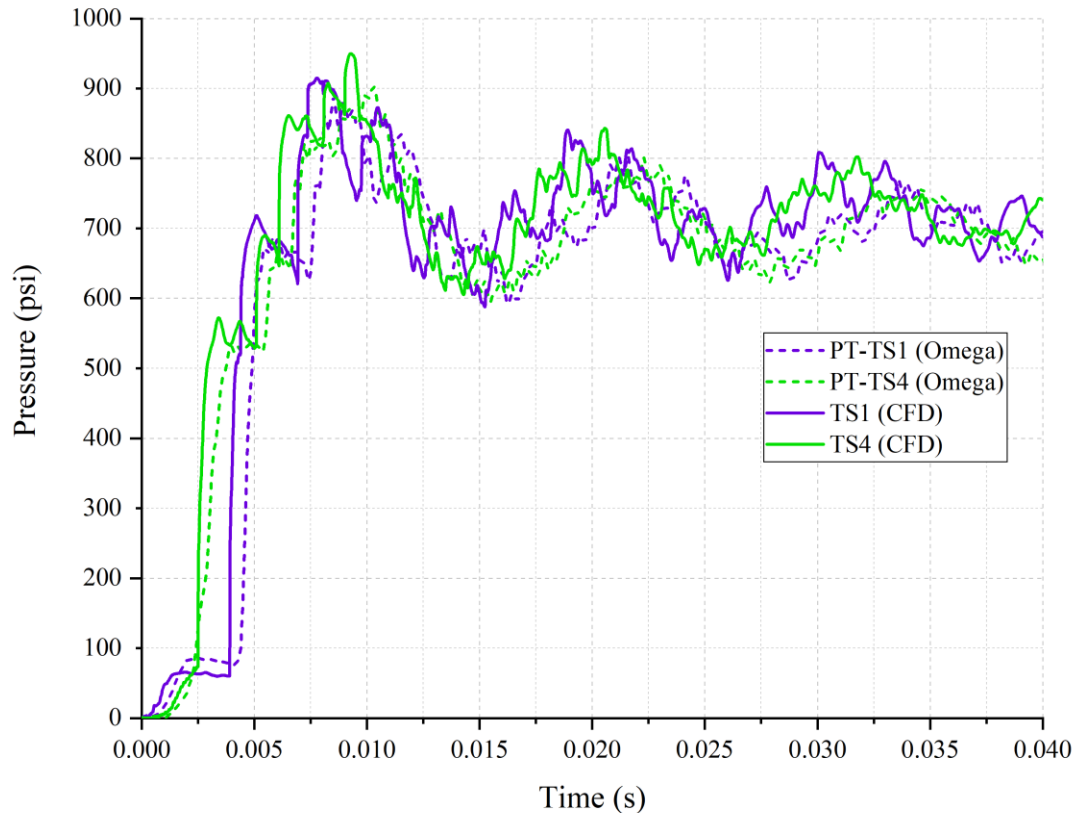


Figure 51. Pressure evolution at the top (TS4) and bottom (TS1) of the cylindrical test section of the out-of-pile HENRI test facility using an intermediate section tube diameter of 1".

The CFD model is able to reproduce experimental data with high accuracy. However, the pressure evolution within the driver tank shows a clear difference in terms of the timing and pressure level, as shown in Figure 52.

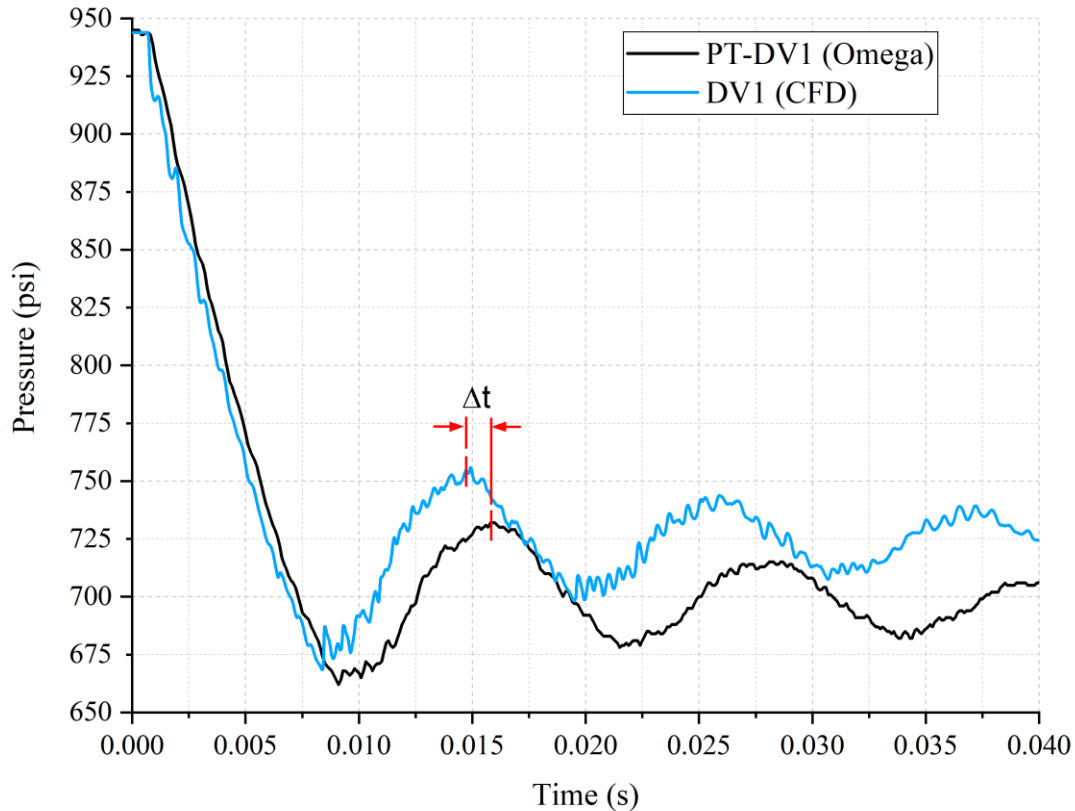


Figure 52. Comparison of pressure evolution inside of the driver tank between experimental and CFD data using an intermediate section tube diameter of 1".

As it was pointed out in the previous simulation, it is possible that the cooling rate of the driver tank in the simulation is slower due to the low heat transfer coefficient assumed. This can be corroborated if the temperature evolution of the CFD model is compared against the measured one. Nonetheless, a direct comparison cannot be effectuated between the calculated and measured temperatures due to the slow response time of the thermocouples used for the out-of-pile HENRI test facility. Another example of the slow response time of the thermocouples is shown in Figure 53 and Figure 54.

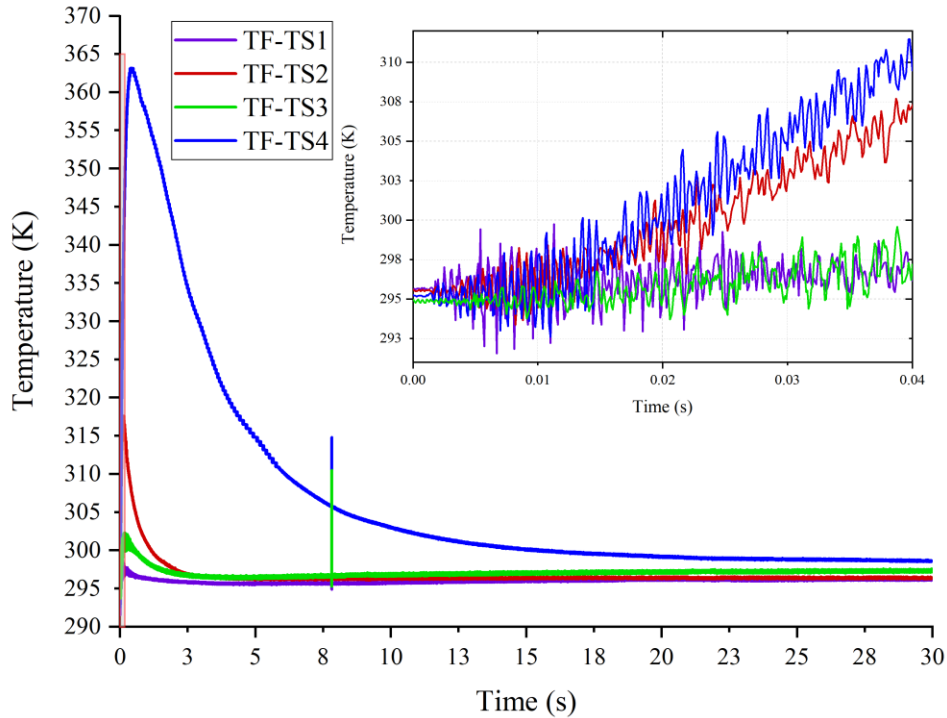


Figure 53. Temperature evolution inside of the cylindrical test section obtained through the HENRI test facility using an intermediate section tube diameter of 1".

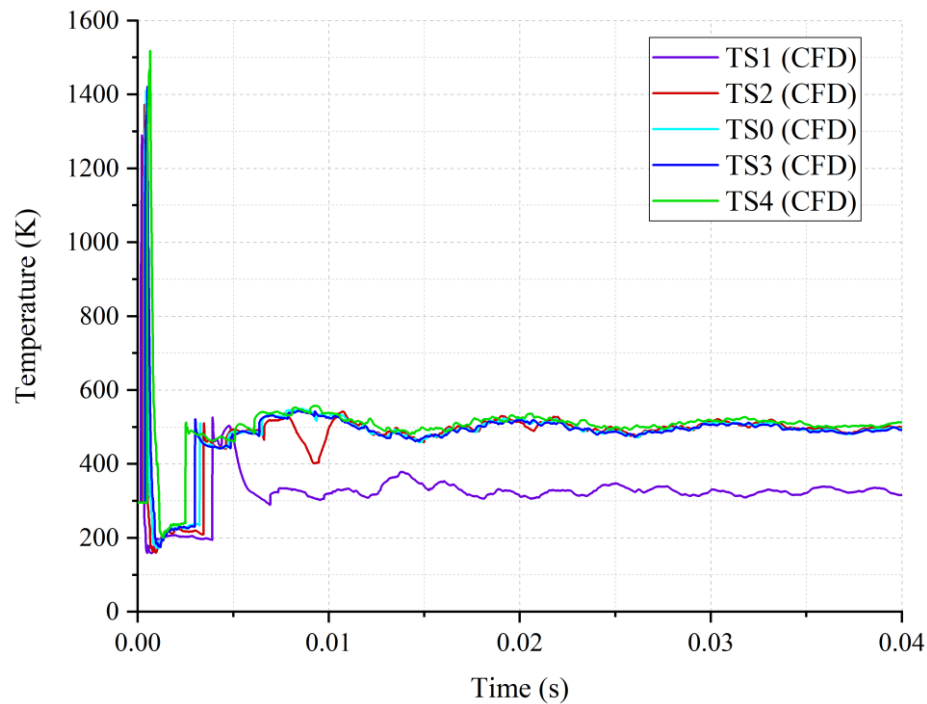


Figure 54. Temperature evolution inside of the cylindrical test section obtained through the HENRI test facility using an intermediate section tube diameter of 1".

The timing and amplitude of the temperature peaks differ from each other considerably. Some of the measured peaks recorded from the experiment have a duration of a few seconds, whereas the calculated peak temperatures have a duration of a fraction of a millisecond. Since a direct comparison of the temperature cannot be performed using the experimental data gathered from the out-of-pile HENRI test facility, further studies regarding the heat transfer mechanism that take place inside of the HENRI test facility should be performed to identify the adequate value for the heat transfer coefficient for the CFD model. However, this analysis is out of the scope of this study.

Since the pressure is the only property that can be compared against the numerical results, the calculated and measured maximum pressure and time to reach the maximum pressure are compared against each other. The results of this 1:1 comparison is shown in Figure 55 and Figure 56.

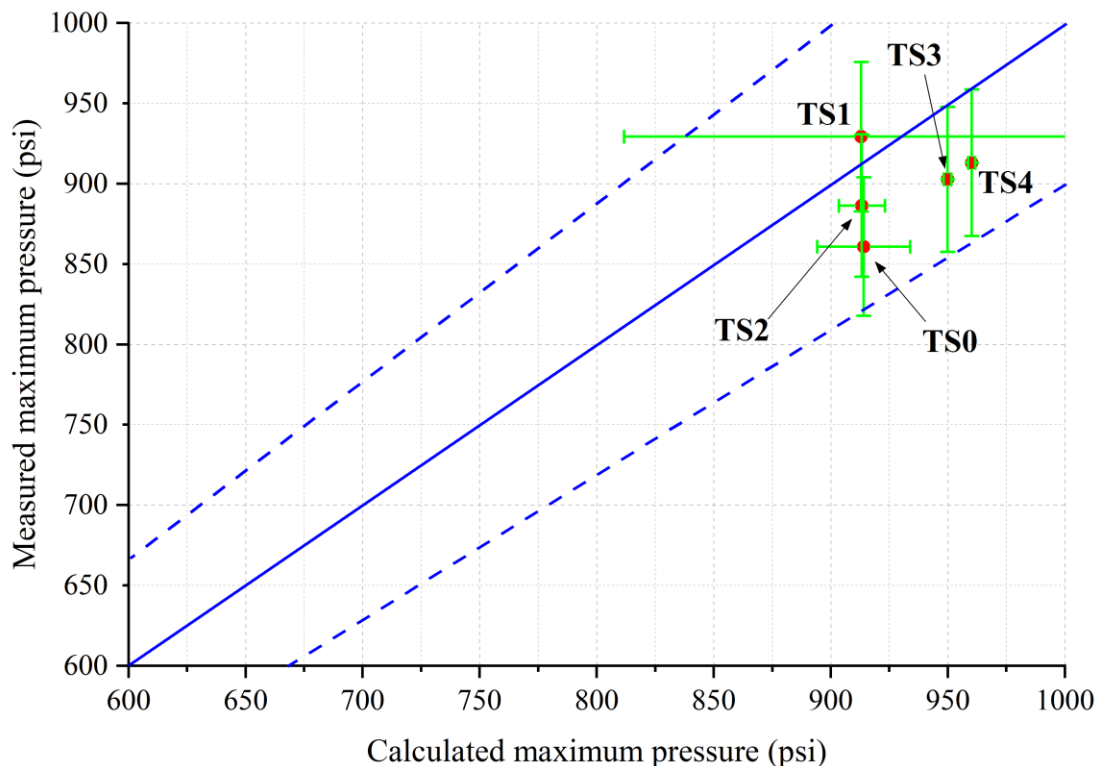


Figure 55. Comparison of measured vs. calculated maximum pressure for the out-of-pile HENRI test facility with intermediate section tube diameter of 1".

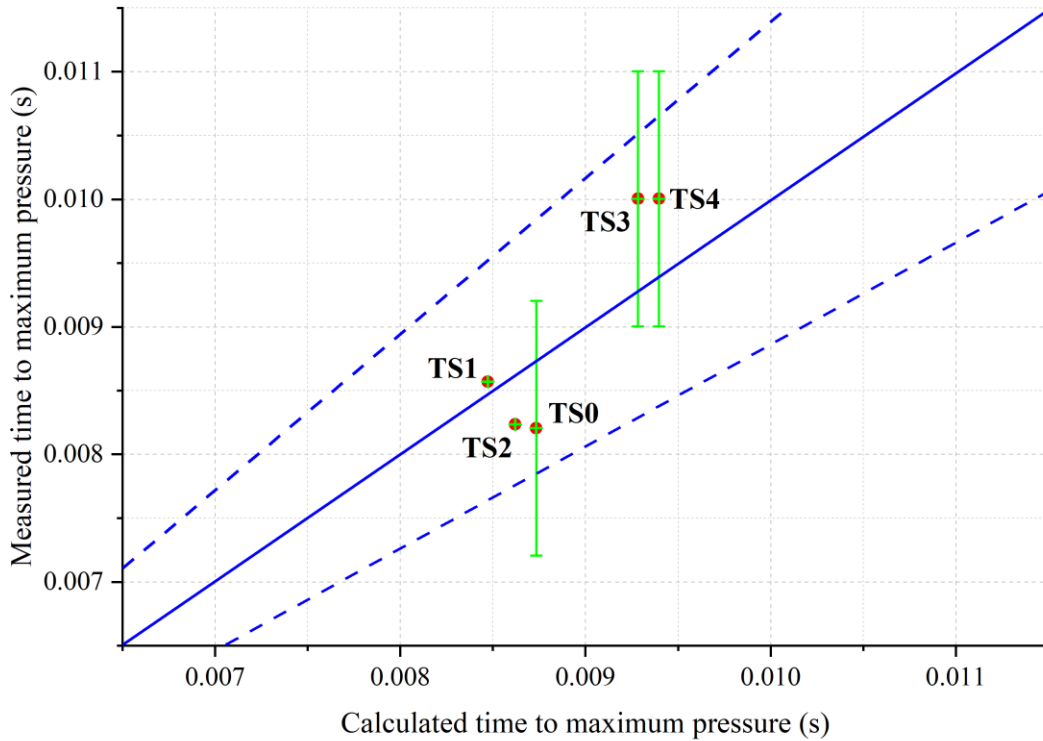


Figure 56. Comparison of measured vs. calculated time to maximum pressure for the out-of-pile HENRI test facility with intermediate section tube diameter of 1".

Based on the results shown in Figure 55, the CFD model is again slightly underestimating the pressure, but the confidence of the values falls within the 10% range. On the other hand, the timing to maximum pressure does not show a significant bias, and the results fall within the 10% range. This means that the timing of the results is very close to the measured values, which indicates that the CFD model can predict the timing of the phenomena with less than 10% difference with respect to the measured data.

Based on the results obtained from the two different scenarios, it can be concluded that the CFD model is able to confidently simulate the pressure evolution within the cylindrical test section. However, some differences were identified while comparing the measured and calculated pressure evolution of the driver tank. This difference can be attributed to the slow response time of the instrumentation and the assumed heat transfer coefficient. The response time of the instrumentation plays a significant role

as it is not considerably fast for the timeframe of interest. This issue can clearly be seen in all the temperature plots. Due to the slow response time of the thermocouples, a direct comparison between the measured and calculated temperatures could not be done. The measured pressures, on the other hand, were compared against the calculated ones as the response time of the sensors is considerably faster than the thermocouples. However, they still have some delay that should be considered. Upon closer examination, the heat transfer coefficient assigned to the wall boundaries was not the most adequate. This conclusion arises from the fact that the calculated pressure of the driver tank oscillates at a higher level, which could be influenced by the temperature. If a low heat transfer coefficient is assigned to the walls of the CFD model, the temperature and pressure will drop at a lower rate.

#### **6.4 Parametric Study: Annular Test Section**

The parametric study done on the HENRI facility is intended to obtain a better understanding of the system's performance under different initial and boundary conditions. For this, two analyses are performed. The first one consists of analyzing the influence of the tube diameter of the intermediate section. Since the mass flow rate is directly influenced by the flow area, a more representative analysis of the system's performance with different tube diameters for the intermediate section is needed. This analysis can corroborate the experimental findings, which support the idea of using a 1" tube for the intermediate section instead of a 0.50" and 0.75" tube.

The second section of this parametric study consists of analyzing the influence that different driver tank pressures can have on the pressurization of the test section. For the driver tank pressure, three different scenarios are considered, where the initial pressure of the driver tank is 900, 1000, and 1100 psi. The goal of this study is to determine if the HENRI facility with an annular test section is able to reach the desired atomic density within 5 ms. In addition, the analysis of three different initial pressures can provide more information regarding relationships or patterns that can be used for future scaling analysis.

#### 6.4.1 Geometry Analysis: Intermediate Section

The analysis of different configurations of the HENRI facility is paramount to better understand the system's performance under different configurations. The following table summarizes the initial and boundary conditions of the simulations used for this analysis.

Table 16. Initial and boundary conditions of the parametric study done on the HENRI facility with different tube diameters for the intermediate section.

Geometry	High/low pressure sections [psi]	Temperature of high/low pressure sections [K]
Cylindrical test section with a 0.50" intermediate section	~913/0.25	~300.65/~294.47
Cylindrical test section with a 0.75" intermediate section	~940/0.25	~300.84/~294.30
Cylindrical test section with a 1.00" intermediate section	~944/0.25	~302.18/~295.31

As it can be noted above, the initial conditions for the 0.75" and 1.00" scenarios are the same as the simulations covered in the benchmark analysis. This was done in an attempt to corroborate the experimental findings, and to use the CFD results to analyze the density evolution using different tube diameters for the intermediate section. Figure 57 compares the calculated pressure evolution inside of the test section using different tube diameters for the intermediate test section.

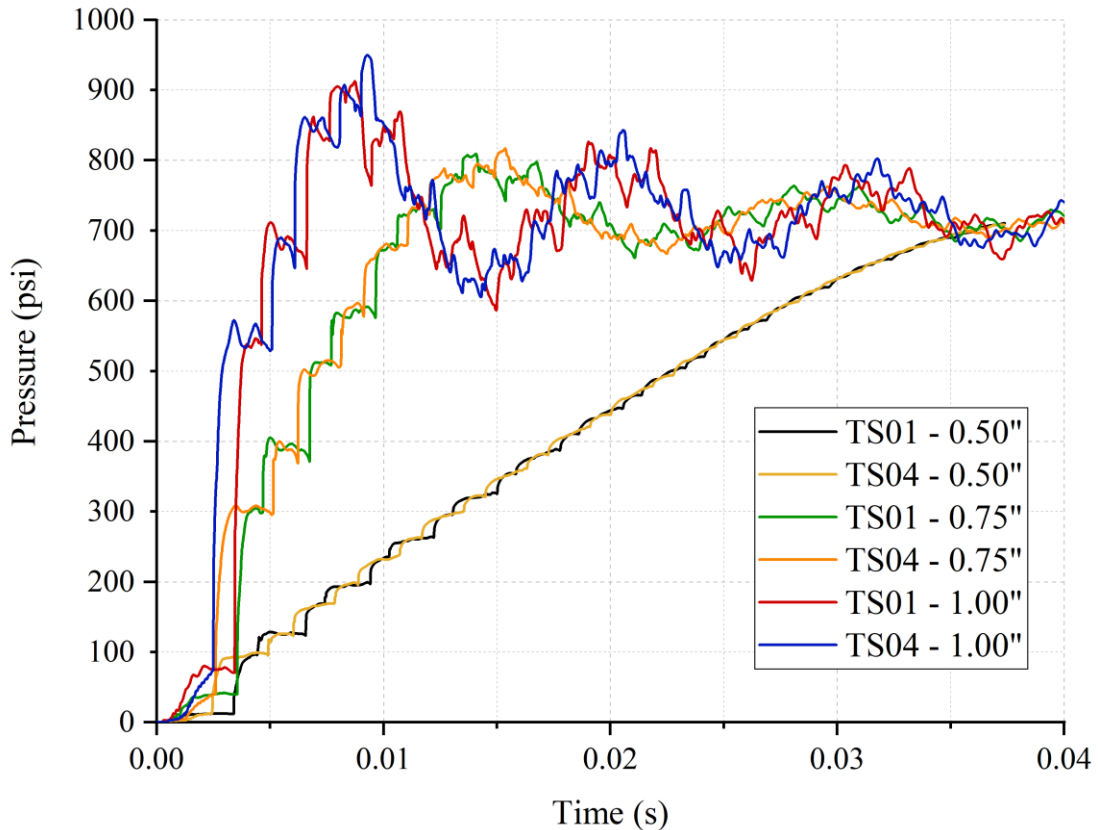


Figure 57. Pressure evolution of the out-of-pile HENRI test facility using different tube sizes for the intermediate section.

From the results shown above, the pressurization of the test section is considerably faster if the out-of-pile HENRI test facility uses a 1" tube diameter instead of the 0.50" one for the intermediate section. However, it is important to keep in mind that the pressure does not necessarily indicate that the test section reached the desired atomic density. The density can indirectly be calculated using the pressure and temperature measurements, but as mentioned earlier the thermocouples have a very slow response time. An indirect calculation of the density evolution will yield results with low accuracy. Thus, the importance of the CFD model.

Since the data presented above was calculated using the CFD model developed in this study, a more accurate density evolution inside of the test section can be obtained, which is shown in Figure 58.

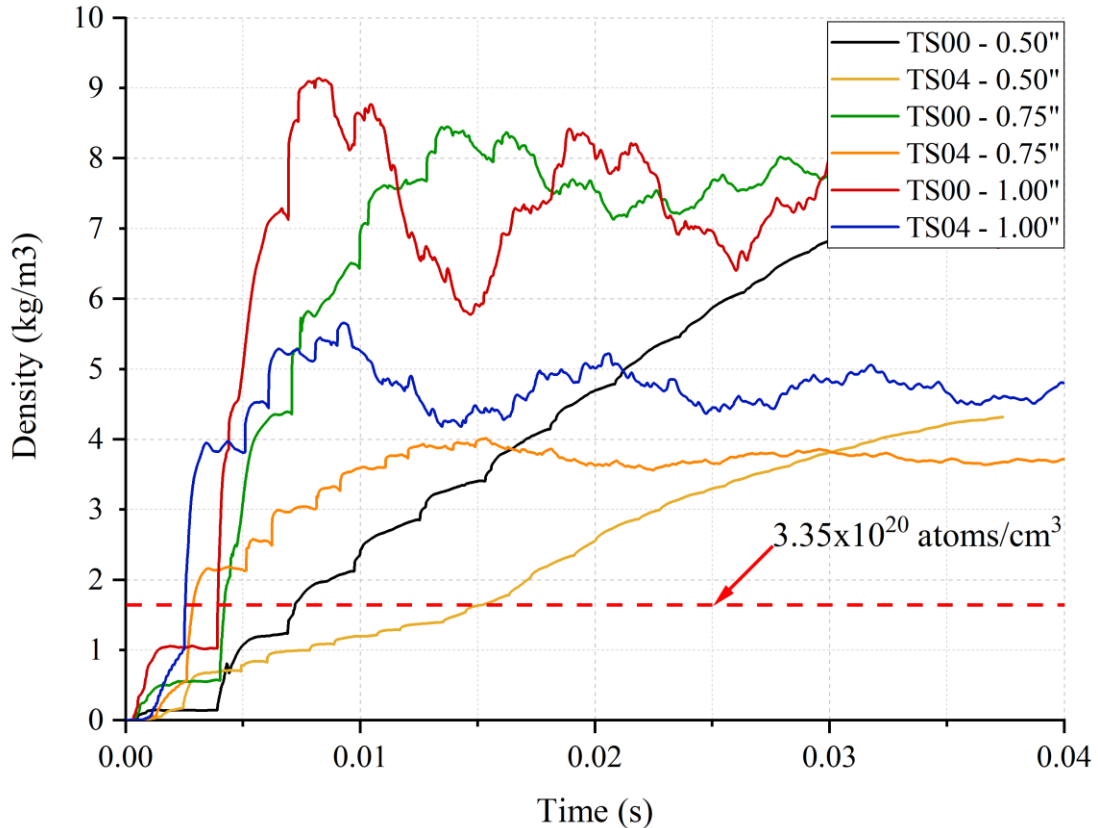


Figure 58. Density evolution inside of the cylindrical test section for the out-of-pile HENRI test facility with different intermediate tube sizes.

From Figure 58, the desired density level is reached in the test section within the first 15 milliseconds using a tube diameter of 0.50" for the intermediate section. Since it is desired to reach an atomic density of  $3.35 \times 10^{20}$  atoms/cm<sup>3</sup> within 5 milliseconds, it is not advised to use a half inch tube. This atomic density level is achieved within the timeframe of interest if the out-of-pile HENRI test facility employs an intermediate section tube diameter of 0.75" or 1". Since the 1" tube diameter configuration reaches the minimum atomic density level slightly faster than the 0.75" tube, it is recommended to use this tube size for better performance.

#### 6.4.2 Driver Tank Pressure Analysis

To identify a relationship that can be used for future preliminary calculations, three simulations were ran for a total simulation time of 10 milliseconds. From this analysis, the following pressure and temperature plots of the annular test section were obtained.

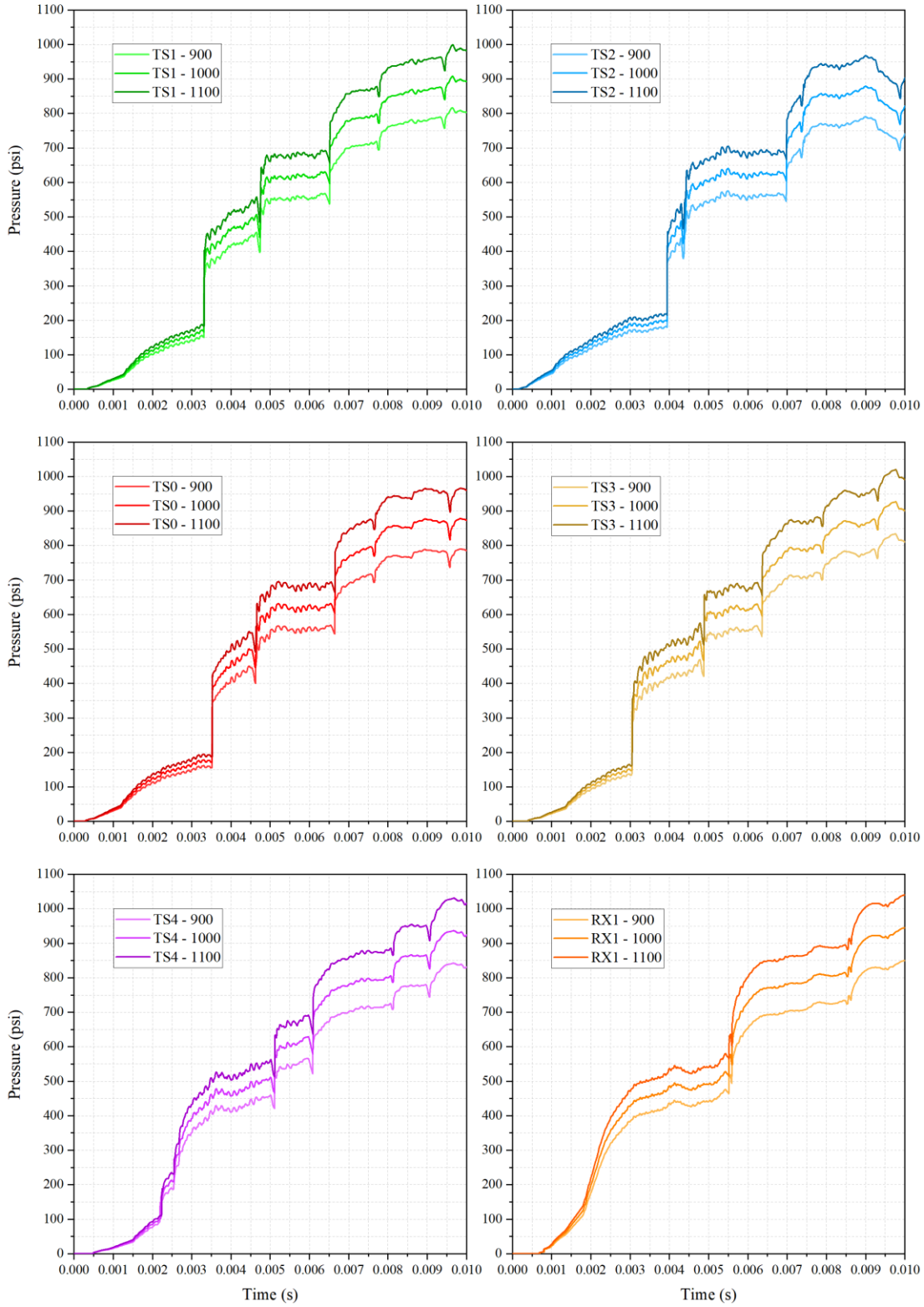


Figure 59. Calculated pressure evolution within annular test section.

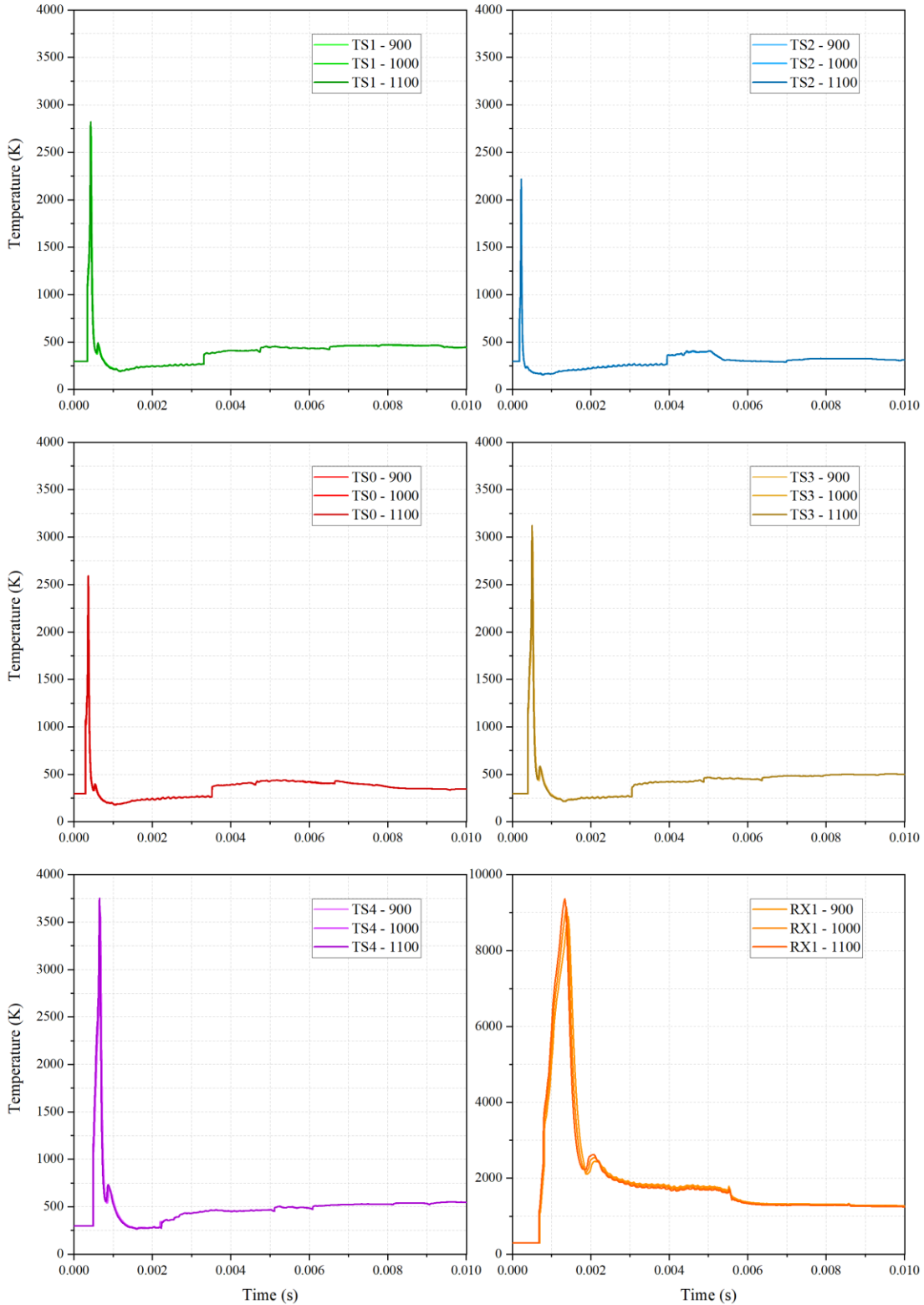


Figure 60. Calculated temperature evolution within annular test section.

Figure 59 show the pressure evolution inside of the annular test section at different locations. As expected, a driver tank with an initial pressure of 1100 psi pressurizes faster than the 1000- and 900-psi scenarios. If all the pressures from Figure 59 are plotted in the same figure and then normalized, the trend of the pressure evolution of the three different simulations are identical to each other, as shown in Figure 61.

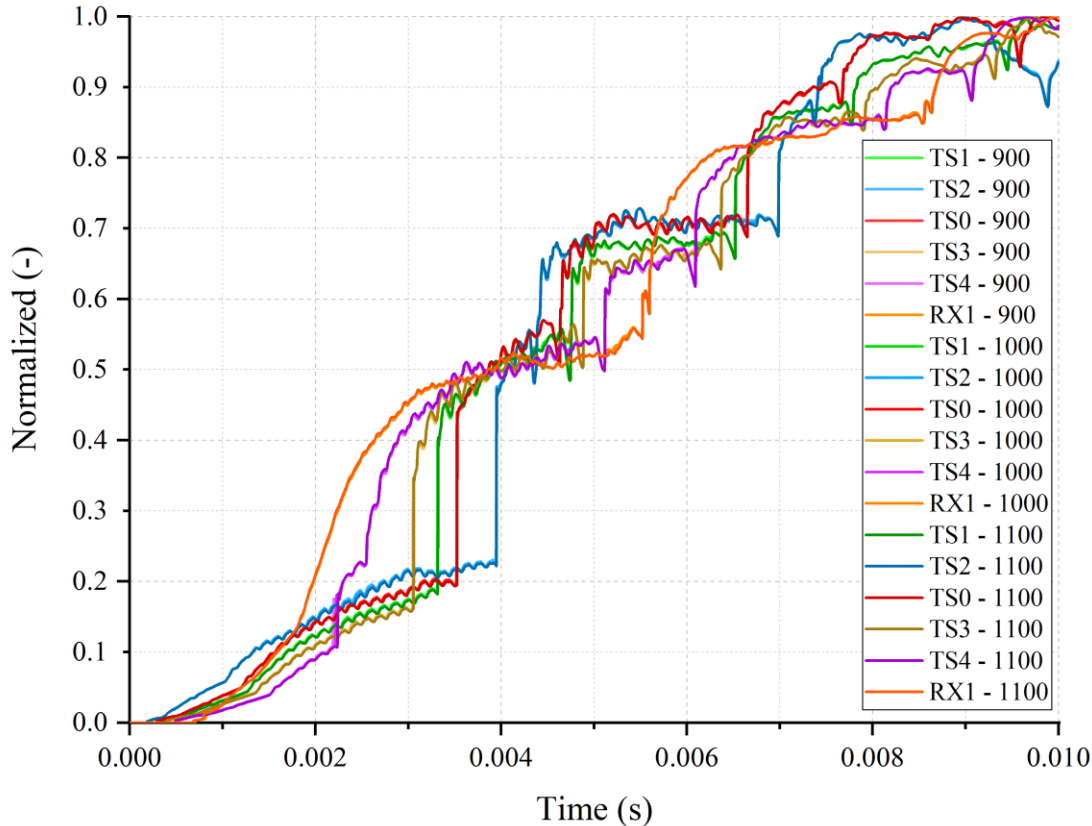


Figure 61. Normalized pressure evolution of the annular test section for the different driver tank pressure scenarios.

For the driver tank, the same approach as the one used for the annular test section was implemented. The pressure profiles of the driver tank for the three different scenarios are displayed in .

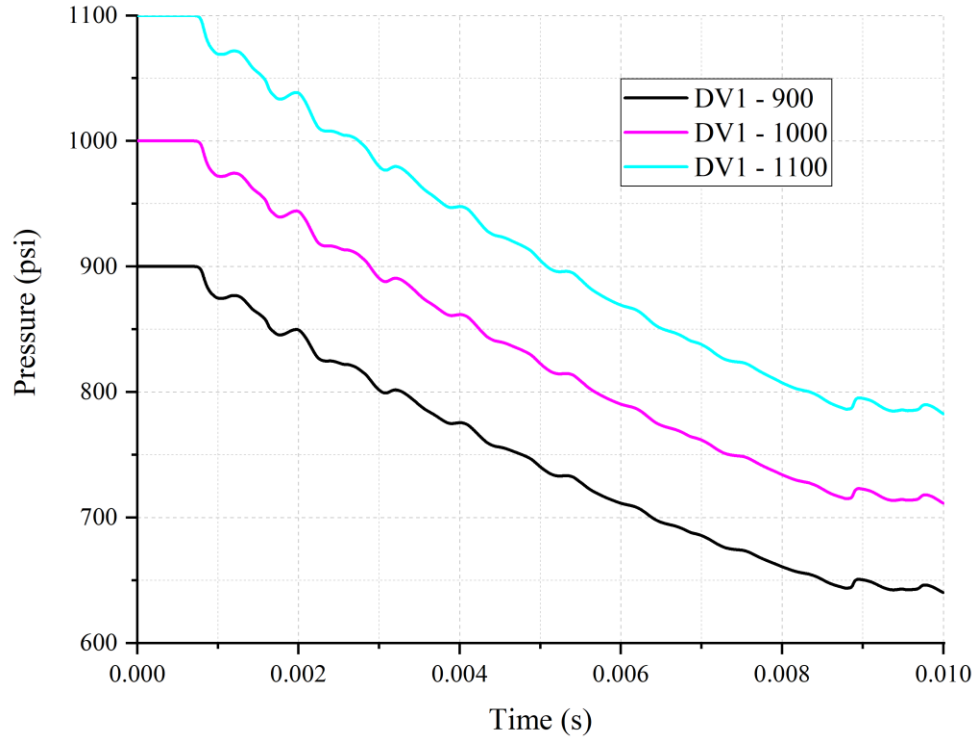


Figure 62. Depressurization of the driver tank at different initial pressures.

As shown above, the pressure evolution for the three simulations are almost identical, but their pressure amplitude is different. This means that if the driver tank pressure of the three simulations is normalized, an identical pressure profile can be obtained.

Another aspect that needs to be analyzed is the temperature evolution in the annular test section, which is shown in Figure 63. As it can be seen, the temperature plots of the three different scenarios are on top of each other.

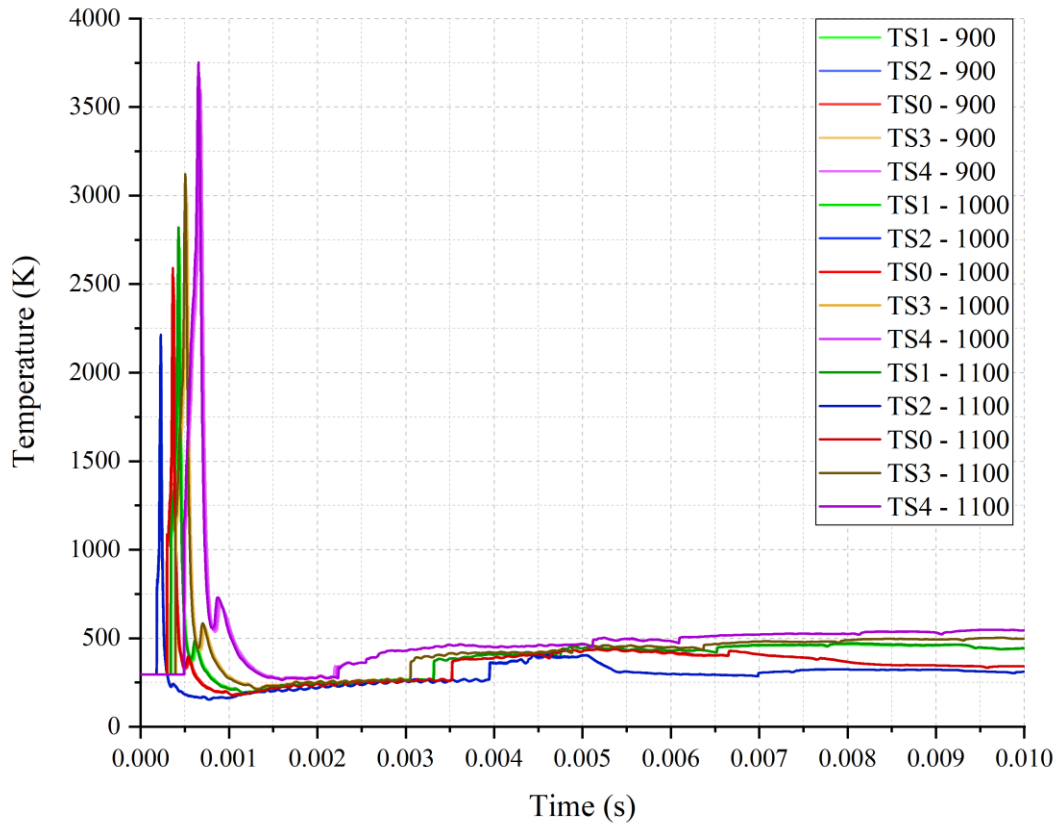


Figure 63. Temperature evolution along the annular test section with different driver tank pressures.

For the temperature evolution, a normalization process is not needed since the temperatures are almost the same. In addition to the pressure and temperature evolution, the density inside of the annular test section was calculated again. The following plots show the density evolution of the annular test section.

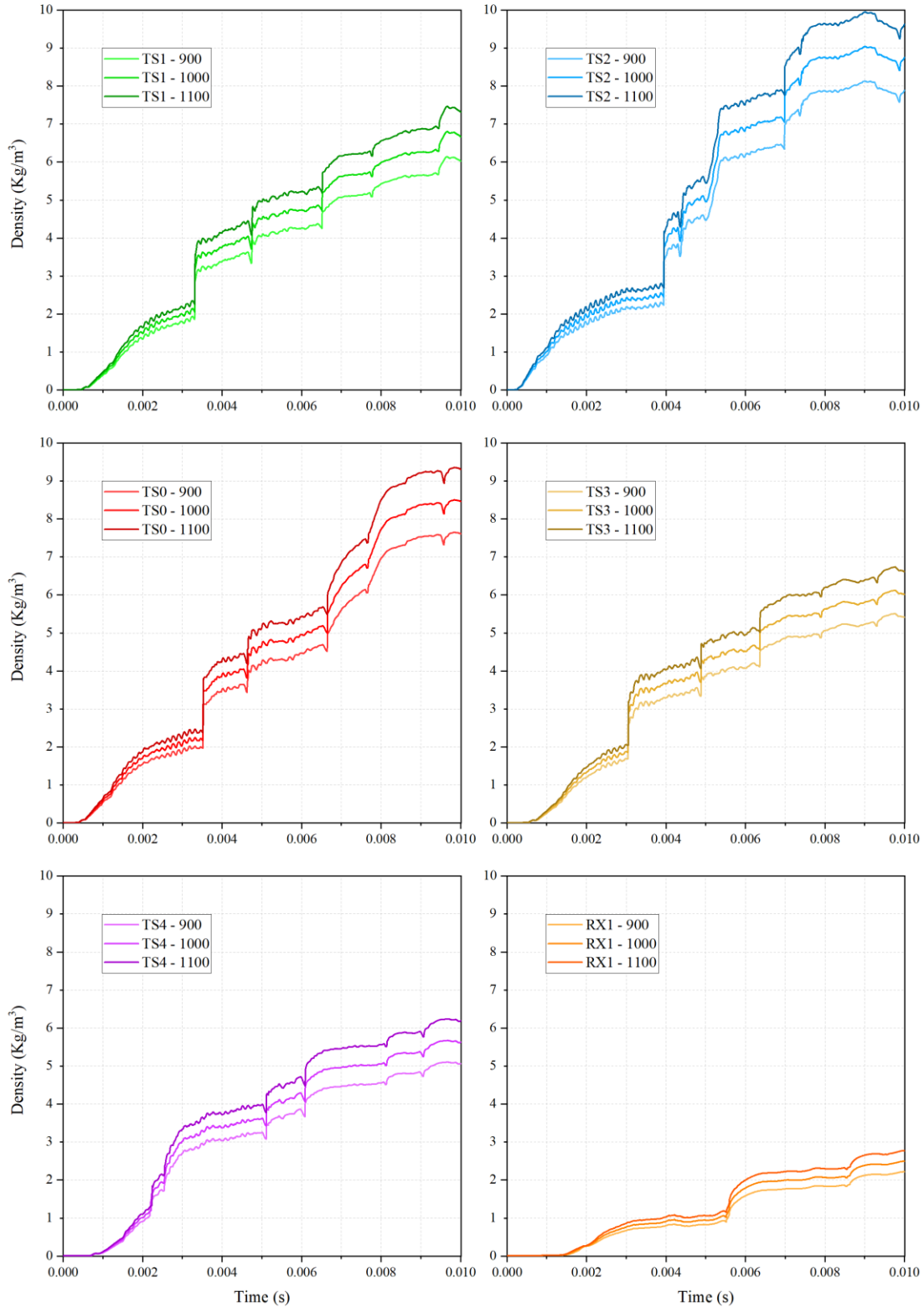


Figure 64. Calculated density evolution within the annular test section.

Similarly to the pressure, the trend of the density evolution for the three simulations are identical to each other, but their density level is different. This means that density evolution can also be normalized, and thus scaled for future analyses.

Since TS4 and TS1 represent the top and bottom, respectively, of the section of interest, the density level between these two points represent the density stratification. Therefore, it is of upmost importance to ensure that the minimum atomic density level is reached at these two points within 5 milliseconds. To determine if this goal is achieved using the initial driver tank pressures of 900, 1000 and 1100, the density calculated at TS4 and TS1 is plotted below.

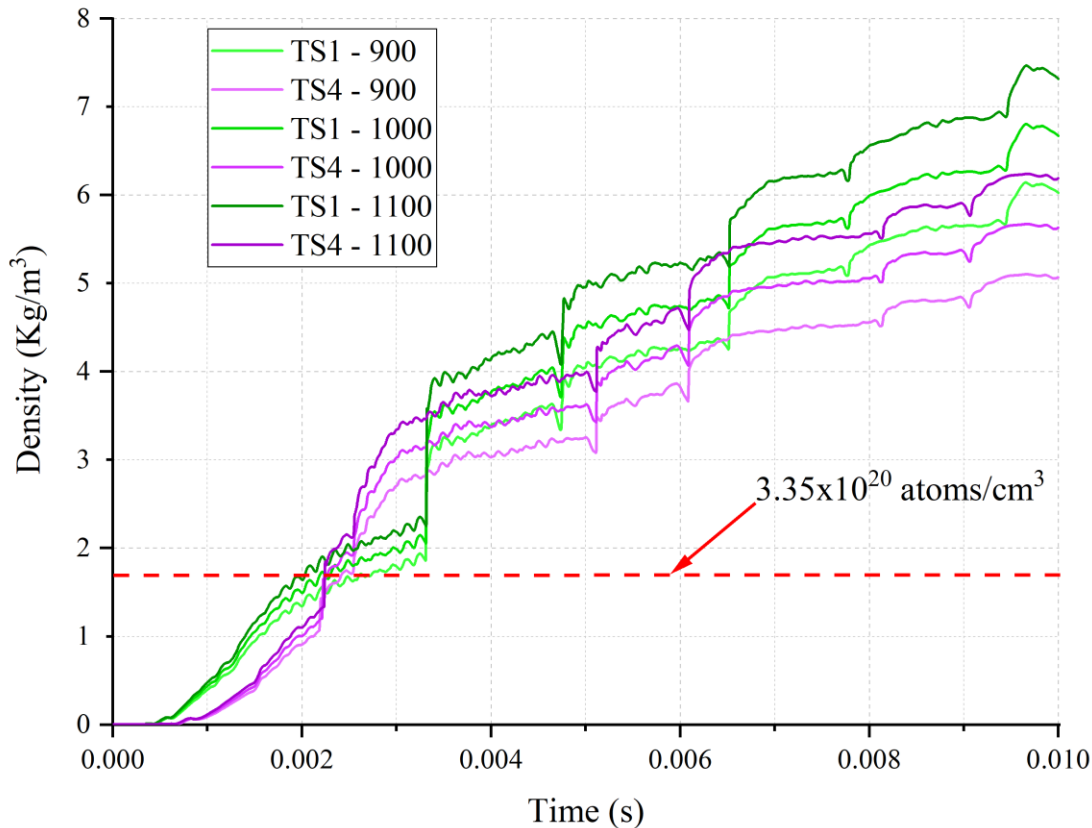


Figure 65. Overall density evolution along annular test section for different initial pressures.

Based on the figure shown above, the desired density level is reached within less than 3 milliseconds for the three different initial conditions.

By knowing that the pressure and density of the driver tank and annular test section can be normalized, it is possible to calculate the initial pressure of the driver tank needed to achieve the desired atomic density level in the annular test section. As stated in the conference paper “Experiments On Helium-3 Negative Reactivity Insertion -HENRI- Prototype”, if the pressure evolution of the test section is normalized to the initial pressure of the driver tank, it is possible to calculate the minimum initial pressure needed for the driver tank [31]. This approach can be implemented for both configurations, the cylindrical and annular. The minimum initial pressure requirement for the driver tank can be obtained by implementing the following equation:

$$P_{Normalized} = \frac{P_{ATS}}{P_{DV1}}, \quad (73)$$

where P is the absolute pressure and the subscripts ATS and DV1 represent the annular test section and driver tank, respectively. At 25°C with an atomic density of  $3.35 \times 10^{20}$  atoms/cm<sup>3</sup> of helium-3, the required pressure inside of the annular test section,  $P_{ATS}$ , is 200 psi. At  $t = 5$  ms.,  $P_{Normalized}$  is about 0.51 at point TS4. Based on these values,

$$P_{Normalized} = \frac{P_{ATS}}{P_{DV1}} \rightarrow P_{DV1} = \frac{200 \text{ psi}}{\sim 0.51} \approx 392.16 \text{ psi}. \quad (74)$$

From the result shown above, the minimum initial pressure of the driver tank needs to be 392.16 psi in order to reach the minimum atomic density level in 5 milliseconds using an annular test section configuration for the HENRI facility.

## 7 CONCLUSION

The testing of prototypical and currently deployed nuclear fuel for LWRs under RIA accident conditions is paramount to better understand the fuel behavior under this transient accident scenario and to ensure the safe operation of nuclear power plants. It is anticipated to perform such tests in the TREAT facility; however, the pulse width is longer than desired. To mimic the neutronic boundary conditions representative of a RIA accident event, it is required to clip the pulse of the TREAT as fast as possible. INL proposed to clip the pulse by inserting helium-3, which is a strong neutron absorber, into an annular gas chamber located in the core of the TREAT facility. In order to clip the pulse of the TREAT, an atomic density level of  $3.35 \times 10^{20}$  atoms/cm<sup>3</sup> needs to be reached in the annular test section within 5 milliseconds. To assess the feasibility of this idea, Oregon State University was tasked to design and build an out-of-pile test facility known as HENRI to evaluate the feasibility and repeatability of the system. This system employs several pressure transducers and thermocouples; however, existing instrumentation is unable to measure directly the density evolution of helium-3 with high accuracy. The density evolution in the annular test section can be calculated indirectly by using the measured pressure and temperature values. However, since the response time of the instrumentation is not fast enough for this system, as demonstrated in Section 6.3 of this document, it is not possible to obtain an accurate density value for this fast transient process. Therefore, a CFD model is needed since it can calculate the pressure, temperature, and density with higher accuracy than an indirect approach.

The main objective of this study is to develop a CFD model that can simulate the temporal and spatial density evolution inside of the HENRI system with high confidence. The observations gathered in this study are presented below.

### 7.1 Observations

From the benchmark or validation process, the measured and calculated pressure and temperature evolution inside of the out-of-pile HENRI test facility were compared

against each other. From this analysis, it was observed that the CFD model slightly underestimates the pressure inside of the cylindrical test section, but the calculated values differ from the measured values within a 10% difference. In addition, it was identified that the measured pressure of the driver tank differs from the calculated. This discrepancy was not seen in the test section. This discrepancy can be attributed to the assumed heat transfer coefficient. This observation is supported by the idea that the velocity of helium in the driver tank is considerably slower than the velocity of helium in the low-pressure section. Since the velocity of helium in the driver tank is slower, heat transfer due convection can have a significant impact on the system.

Another observation made in this study is regarding to the response time of the instrumentation. The time difference between the experimental and numerical results is more noticeable when comparing the temperature and pressure of the driver tank. From the results covered before, the response time of the pressure transducers was the major contributor to the timing difference between the measured and calculated pressures. The calculated and measured temperature evolution in the driver tank and low-pressure section could not be compared on the same plots due to the slow response time of the thermocouples. Also, the thermocouples were unable to properly capture the temperature evolution of the low-pressure section with high accuracy. However, the calculated temperature stratification was consistent with the measured data.

In the parametric study done on the annular test section, two observations were made. The first one consists of the system's performance using different tube diameters for the intermediate section. Based on the results obtained in this study, it is recommended to use a tube diameter of 1" instead of a 0.75" and 0.50" tubes. A 0.75" tube diameter can still be used, but the pressurization of the annular test section will be slower. The 0.50" tube is not recommended to be used in the HENRI system as the minimum density level was reached within 15 milliseconds.

The second observation consists of the pressure, temperature and density evolution along the driver tank and test section with different initial driver tank pressures. For the

pressure and density, it was identified that the pattern is the same for the three scenarios analyzed. The only difference was their amplitude. This means that the pressure and density can scaled for future analyses. In addition, the minimum initial pressure needed for the driver tank can be calculated by using Equation (73). A preliminary analysis was performed, and it was identified that the driver tank pressure must be 392.16 psi or higher in order to reach the desired minimum atomic density in the section of interest.

Another observation made in the parametric study was regarding the ability to reach the desired atomic density,  $3.35 \times 10^{20}$  atoms/cm<sup>3</sup>, within 5 ms using a initial driver tank pressure of 900, 1000 and 1100 psi. Based on the results shown in Figure 65, the desired atomic density was reached in a shorter time-frame for all three scenarios.

## 7.2 Relevance of Work

Since the testing of advanced nuclear fuels and materials under RIA events is anticipated to take place in the TREAT facility, the proper setup of the experiment is important. This includes the reproduction of the neutronic and thermal-hydraulic boundary conditions. Through the use of the HENRI facility, the TREAT will be able to recreate the RIA conditions without exceeding its license threshold. As stated earlier, the proper shortening or clipping of the pulse can be achieved through the use of helium-3. Due to the fact that helium-3 has a large neutron absorption cross-section, the fast insertion of many helium-3 atoms into gas chambers, which will be located in the reactor core, will lead to a decrease of neutron population and therefore clip the pulse of the nuclear reactor. That being said, the most important parameter to measure is the atomic density of helium in the annular gas chamber. This measurement can be obtained through the use of a CFD model. This model needs to be verified and validated against analytical and experimental results in order to assess the model's ability to reproduce real-world phenomena. Therefore, this study was conducted in order to create a CFD model that can accurately simulate the density evolution of the HENRI facility. This CFD model is anticipated to be coupled with a reactor physics code in order to analyze the system's capability to clip the pulse of the TREAT properly prior testing the in-pile system.

### 7.3 Assumptions and Limitations

Throughout the course of this study, several assumptions were made in order to obtain the results presented in this document. One of the main assumptions made for the simulations is the pressure for the low-pressure section. Several pressure values were tested and considered, but significant numerical stability issues were encountered. It was identified that a low-pressure of 0.25 psi or higher provides adequate results. Based on this, a pressure of 0.25 psi was chosen for the simulations covered in this study.

The second major assumption made in this study is the heat transfer through the walls. The major heat transfer mechanism that could take place inside the HENRI system is convection on the inner walls. Since the fluid in the test section has a considerably fast velocity, the Biot number was calculated in order to determine if the heat transfer on the walls of the test section within the timeframe of interest can be neglected. It was determined that the transient process is considerably fast that heat lost due to convection can be neglected for the test section. Initially, an adiabatic boundary condition was assumed, but it led to high residual levels. Thus, a low heat transfer coefficient value of  $5 \text{ W/m}^2\text{-K}$  was assumed. However, it was later found out that this assumption is not adequate.

The main limitation encountered in this study was the computational resources available. As stated previously, the results from the simulations can be improved if the mesh can be refined even further, and/or the time-step can be reduced as well. The computational resources available for this study were limited, so the time-step and the mesh size were not reduced any further in order to obtain acceptable results in a timely manner.

### 7.4 Future Work

There are two major areas on this study that require further analysis. One of them is the computational cost of the simulation. Even though the results obtained from the low-pressure section from the cylindrical test section were very close to the experimentally

measured, the time that it required to run the simulations were longer than desired. Several attempts were made to reduce the computational cost, but there was not sufficient time to further reduce the computational cost.

The second area that requires further study is regarding the heat transfer coefficient of the simulation. For the test section, the heat transfer due to convection can be neglected for the timeframe of interest. However, results showed that the assumed heat transfer coefficient was not adequate for sections where the helium moves at a lower velocity, such as in the driver tank and end of extension section. The results presented in this study can be further improved if a heat transfer analysis on the system is done so the temperature and pressure of the system can be better simulated.

## 8 REFERENCES

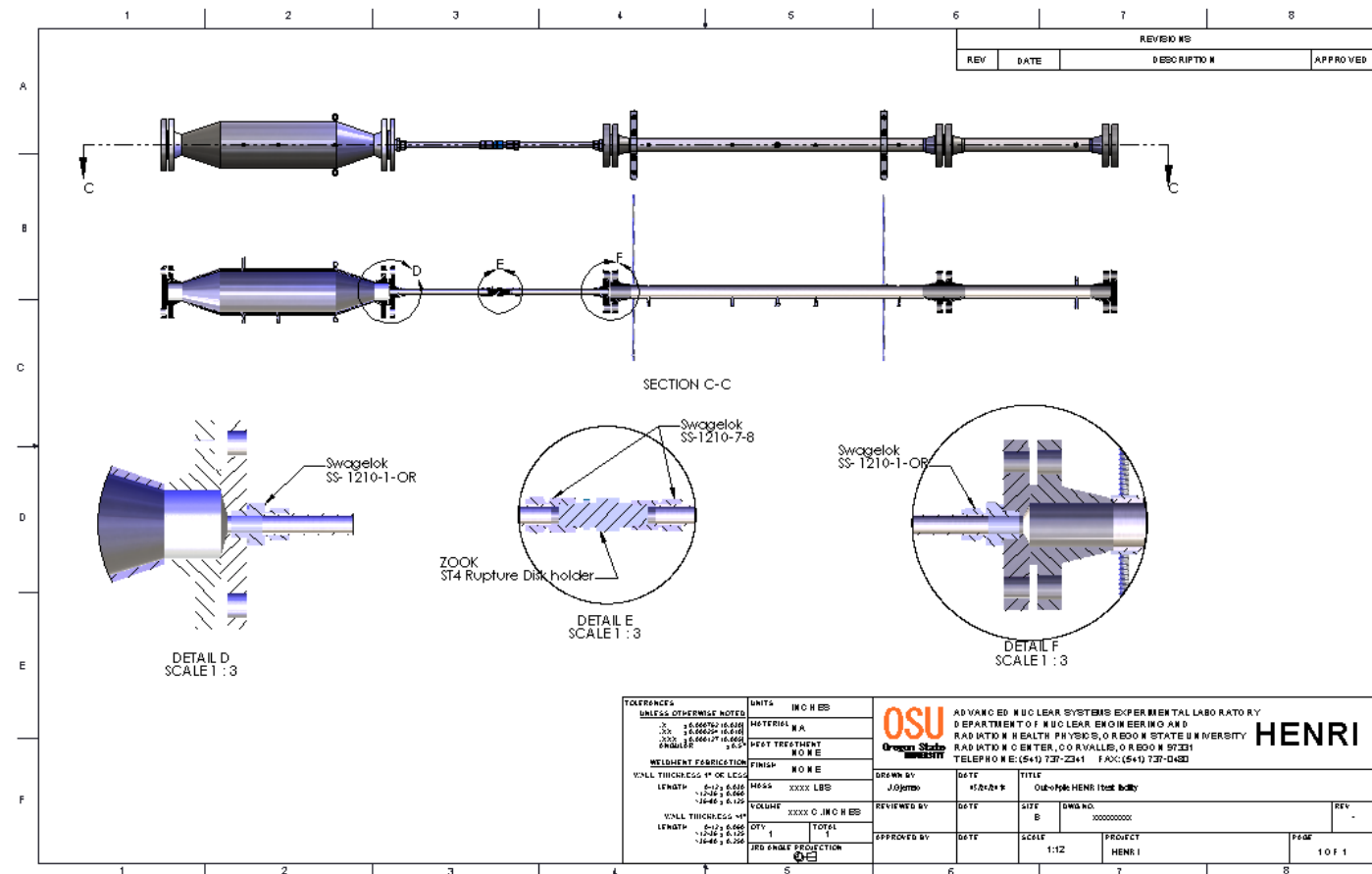
- [1] N. E. Woolstenhulme and J. D. Wiest, "ATF Transient Testing Pre-Conceptual Engineering Status Summary," Idaho National Laboratory, Idaho Falls, 2013.
- [2] N. E. Institute, "Accident Tolerant Fuel," [Online]. Available: <https://www.nei.org/advocacy/make-regulations-smarter/accident-tolerant-fuel>. [Accessed 15 08 2019].
- [3] T. Holschuh, N. Woolstenhulme, B. Baker, J. Bess, C. Davis and J. Parry, "Transient Reactor Test Facility Advanced Transient Shapes," *Nuclear Technology*, 2019.
- [4] D. C. Crawford, R. W. Swanson, A. E. Wright and R. E. Holtz, "RIA Testing Capability of the Transient Teactor Test Facility," IAEA-TECDOC-1122, Victoria, 1998.
- [5] J. D. Bess, N. E. Woolstenhulme, C. B. Davis, L. M. Dusander, C. P. Folsom, J. R. Parry, T. H. Shorthill and H. Zhao, "Narrowing transient testing pulse widths to enhance LWR RIA experiment design in the TREAT facility," *Annals of Nuclear Energy*, vol. 124, pp. 548-571, 2019.

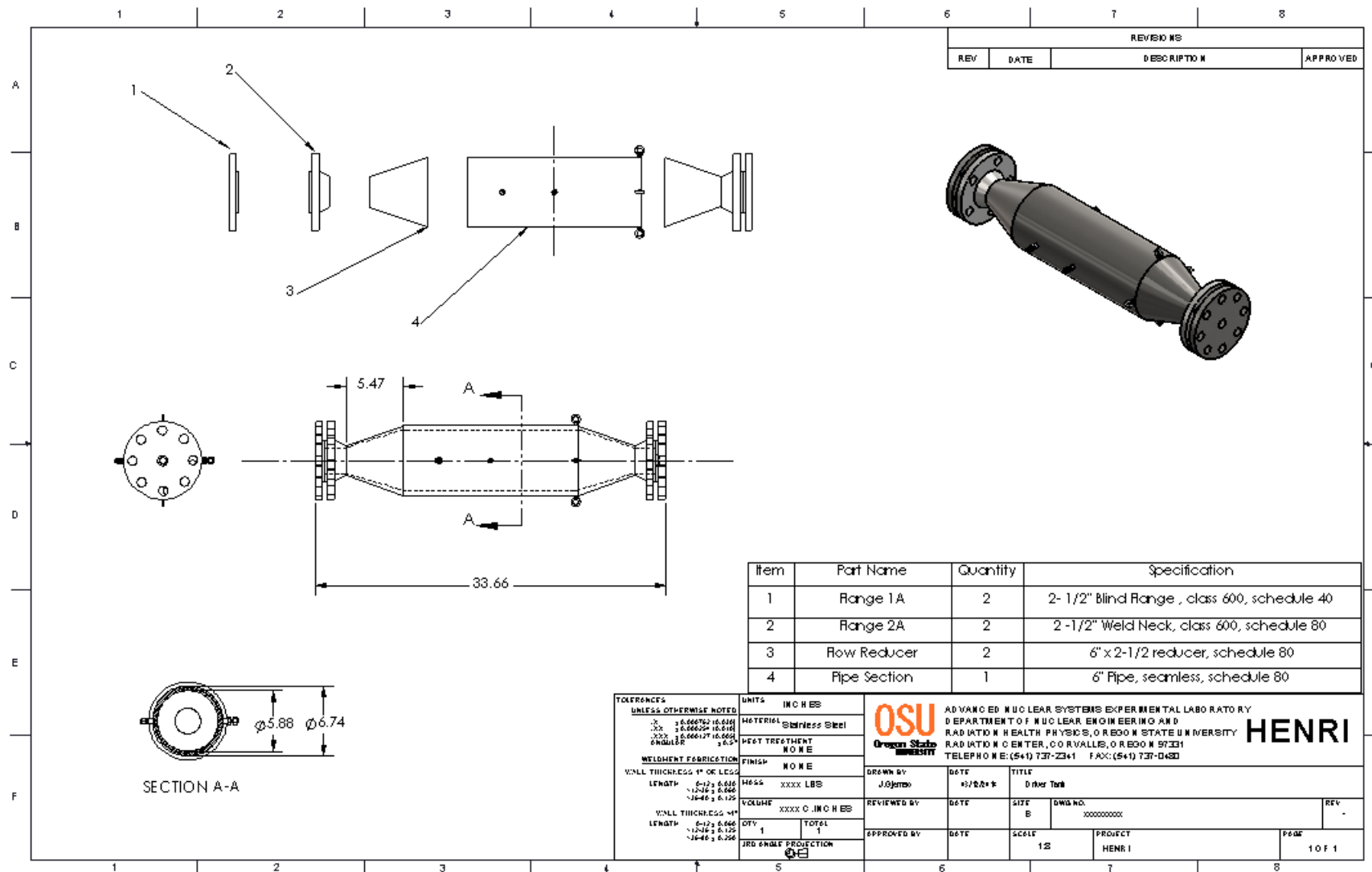
- [6] A. S. o. M. Engineers, "Standard for Verification and Validation in Computational Fluid Dynamics and Heat Transfer," American Society of Mechanical Engineers, New York, 2009.
- [7] J. D. Anderson, Modern Compressible Flow, College Park: McGraw-Hill, 2012.
- [8] V. Babu, Fundamentals of Gas Dynamics, Chennai: Wiley, 2015.
- [9] J. D. Anderson, Fundamentals of Aerodynamics, College Park: McGraw-Hill, 1991.
- [10] M. Maillot, G. Truchet, J. P. Hudelot and J. Lecerf, "Analysis of the Rod-drop Experiments Performed During the CABRI Commissioning Tests," in *European Research Reactor Conference*, Munich, 2018.
- [11] B. Duc, B. Biard, P. Debias, L. Pantera, J. P. Hudelot and F. Rodiac, "Renovation, Improvement and Experimental Validation of the Helium-3 Transient Rods System for the Reactivity Injection in the CABRI Reactor," in *Advancements in Nuclear Instrumentation Measurement Methods and their Applications*, Liege, 2017.
- [12] O. Clamens, J. Lecerf, J.-P. Hudelot, B. Duc, T. Cadiou, P. Blaise and B. Biard, "Assessment of the He-3 Pressure Inside the CABRI Transient Rods - Development of a Surrogate Model Based on Measurements and Complementary CFD Calculations," in *Advancements in Nuclear Instrumentation Measurement Methods and their Applications*, Liege, 2017.
- [13] CD-adapco, "User Guide STAR-CCM+," Siemens Product Lifecycle Management Software Inc., 2014.
- [14] N. E. Todreas and M. S. Kazimi, Nuclear Systems, 2 ed., vol. 1, Boca Raton: CRC Press, 2012.
- [15] N. Hall, "Boundary Layer," National Aeronautics and Space Administration, 05 May 2015. [Online]. Available: <https://www.grc.nasa.gov/WWW/k-12/airplane/boundlay.html>. [Accessed 3 August 2019].
- [16] J. M. Saleh, Fluid Flow Handbook, New York: McGraw-Hill, 2002.

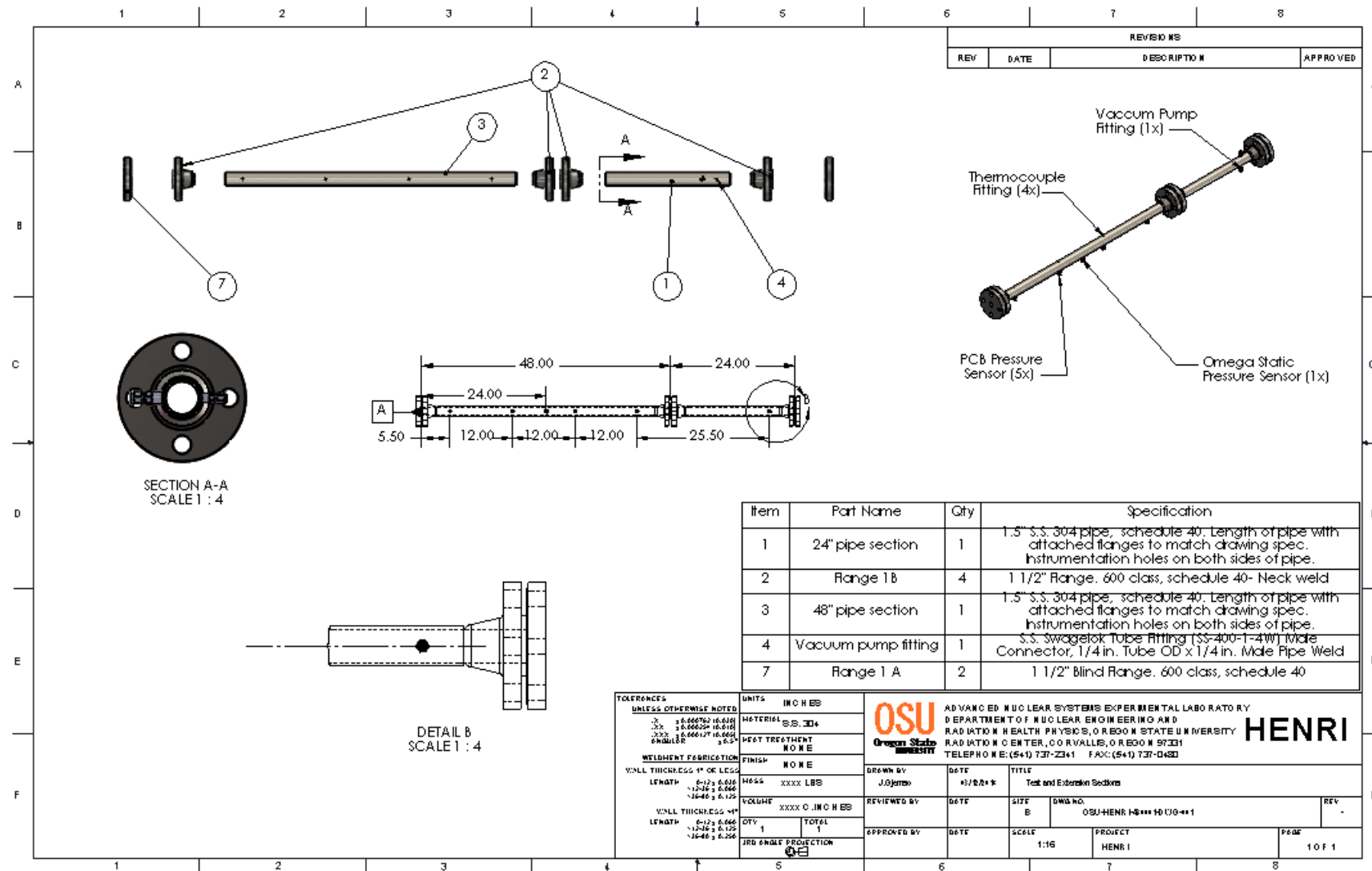
- [17] P. R. Spalart, "Detached-Eddy Simulation," *Annual Review of Fluid Mechanics*, vol. 41, pp. 181-202, 2009.
- [18] C. Rumsey, "Turbulence Modeling Resource," NASA, 30 06 2015. [Online]. Available: <https://turbmodels.larc.nasa.gov/sst.html>. [Accessed 28 05 2019].
- [19] O. Clamens, J. Lecerf, B. Duc and J. P. Hudelot, "Assessment of the CABRI Transients Power Shape by Using CFD and Point Kinetics Codes," in *ANIMMA*, Liege, 2017.
- [20] S. A. Balderrama Prieto, G. Mignot, N. Woolstenhulme and M. Wade, "CFD Modeling of the Gas Injection System for the Out-of-pile HENRI Facility," in *18th International Topical Meeting on Nuclear Reactor Thermal Hydraulics*, Portland, 2019.
- [21] J. Dow, A Unified Approach to the Finite Element Method and Error Analysis Procedures, San Diego: Academic Press, 1998.
- [22] J. Tu, G. H. Yeoh and C. Liu, Computational Fluid Dynamics, Waltham: Butterworth-Heinemann, 2008.
- [23] I. B. Celik, U. Ghia, P. J. Roache, C. J. Freitas, H. Coleman and P. E. Raad, "Procedure for Estimation and Reporting of Uncertainty Due to Discretization in CFD Applications," *Journal of Fluids Engineering*, vol. 130, no. 7, 2008.
- [24] F. P. Incropera, D. P. Dewitt, T. L. Bergman and A. S. Lavine, Fundamentals of Heat and Mass Transfer, New Jersey: John Wiley & Sons, 2007.
- [25] T.-T. Nguyen, "The Characterisation of a Shock Tube System for Blast Injury Studies," Imperial College London, London, 2016.
- [26] F. X. Giraldo, "Time-integrators," [Online]. Available: [http://faculty.nps.edu/fxgirald/projects/nseam/nps/new\\_section4.pdf](http://faculty.nps.edu/fxgirald/projects/nseam/nps/new_section4.pdf). [Accessed 08 May 2019].
- [27] S. B. Pope, Turbulent Flows, Cambridge: Cambridge University Press, 2000.
- [28] N. J. Georgiadis and D. A. Yoder, "Recalibration of the Shear Stress Transport Model to Improve Calculation of Shock Separate Flows," National Aeronautics and Space Administration, Grapevine, 2013.

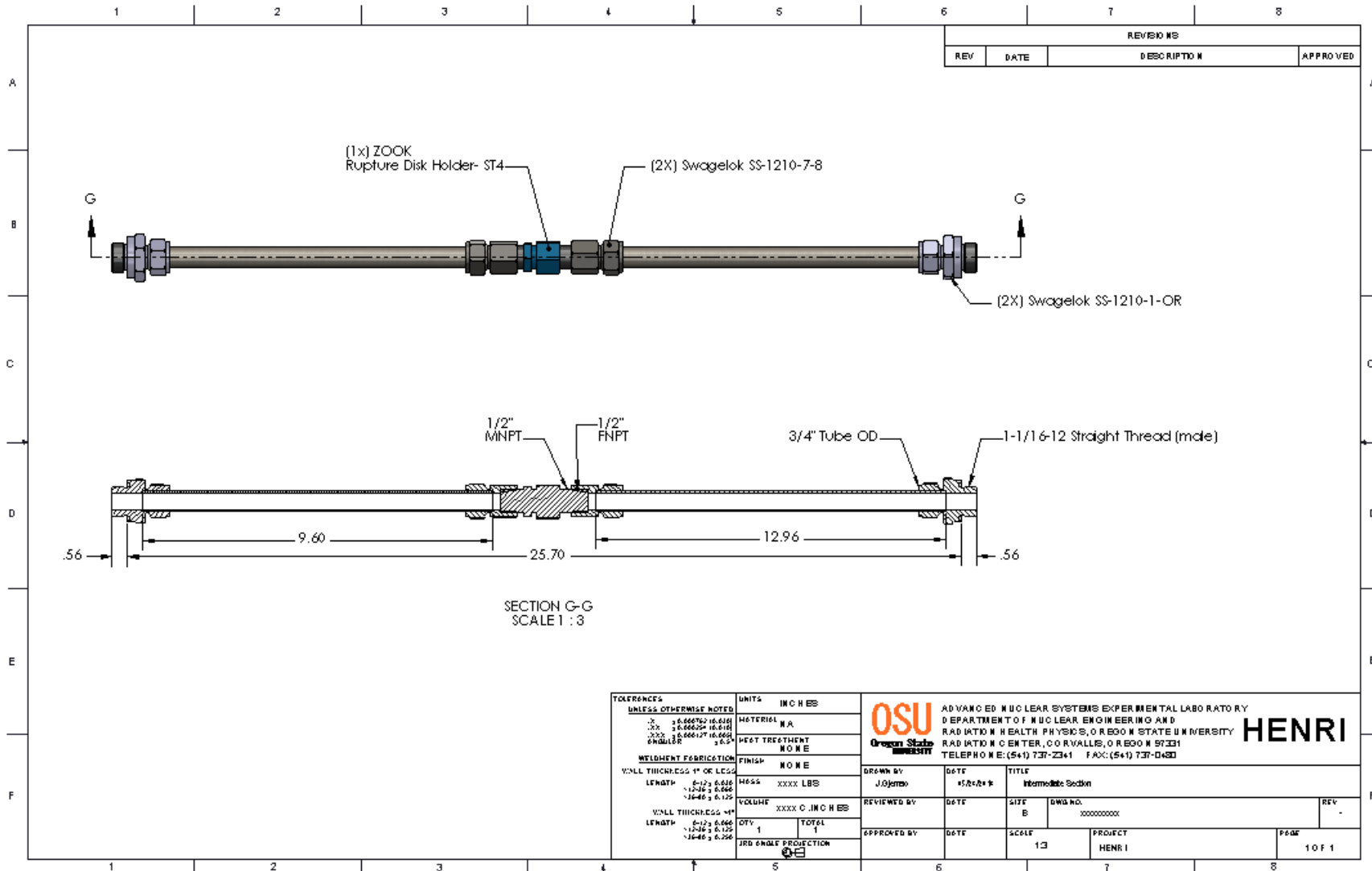
- [29] "Omega," [Online]. Available: <https://www.omega.com/en-us/sensors-and-sensing-equipment/pressure-and-strain/pressure-transducers/p/PX409-Series>. [Accessed 06 07 2019].
- [30] "PCB Piezotronics," [Online]. Available: <http://wwwpcb.com/Products.aspx?m=113B24>. [Accessed 06 07 2019].
- [31] G. Mignot, A. Warren, S. A. Balderrama Prieto and W. Marcum, "Experiments on Helium-3 Negative Reactivity Insertion - HENRI - Prototype," in *NURETH-18*, Portland, 2019.
- [32] F. R. Menter, "Two-equation Eddy-viscosity Turbulence Models for Engineering Applications," *AIAA*, vol. 32, no. 8, pp. 1598-1605, 1994.

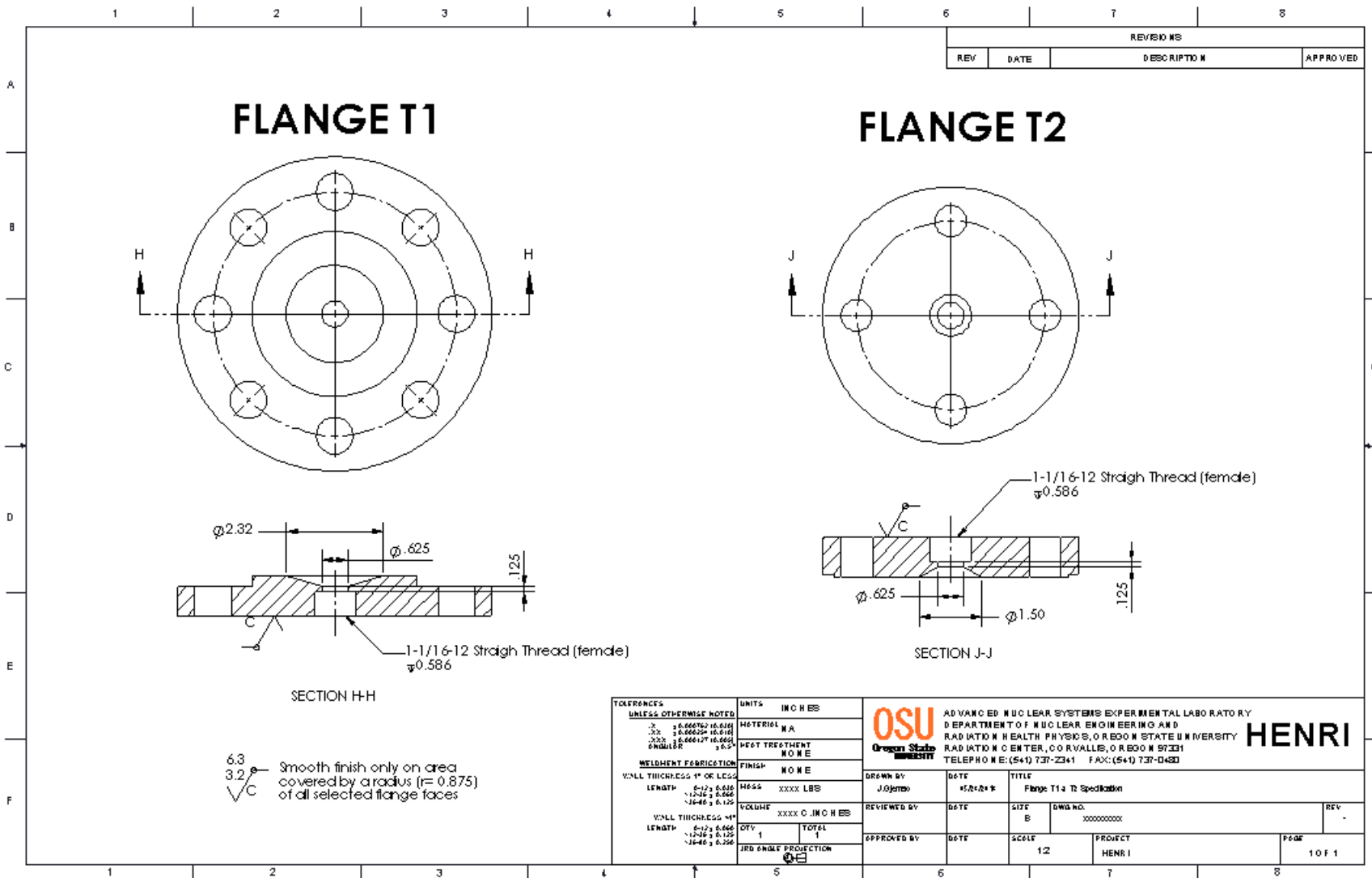
## 9 APPENDIX A: OUT-OF-PILE HENRI TEST FACILITY DRAWINGS











## 10 APPENDIX B: OUT-OF-PILE HENRI TEST FACILITY MATRIX TEST

Test no.	Rupture disk diameter [in]	Test section configuration	Surface roughness	Fast response device	Pressure [psia]	Temperature [K]
15	11/16	Cylindrical geometry w/ extension	N/A	Fragmenting rupture disk	500	~295
16	11/16	Cylindrical geometry w/ extension	N/A	Fragmenting rupture disk	800	~295
17	11/16	Cylindrical geometry w/ extension	N/A	Fragmenting rupture disk	1000	~295
12-13	1/2	Cylindrical geometry w/ extension	N/A	Non-fragmenting rupture disk	1000	~295
10-11	3/4	Cylindrical geometry w/ extension	N/A	Non-fragmenting rupture disk	1000	~295
14	3/4	Cylindrical geometry w/o extension	N/A	Non-fragmenting rupture disk	1000	~295
14	1	Cylindrical geometry w/ extension	N/A	Non-fragmenting rupture disk	1000	~295
14	1	Annular geometry	Rough	Non-fragmenting rupture disk	1000	~295
	1	Annular geometry	Smooth	Non-fragmenting rupture disk	1000	~295

## 11 APPENDIX C: GCI MATLAB CODE

```
%% ##########
% The following code is used to quantify the error introduced by the mesh
% used ofr a CFD model using the GCI method approach
%% #####
clear
clc
% Values
h=[2;3;4]; % Grid size
phi=[0.25    0.25    2.30027;
3.33457 3.36993 3.65492;
3.96498 3.76722 3.99627;
4.78728 4.68978 4.59425;
5.06946 5.41533 5.34787;
5.62229 5.99973 5.96724;
6.04072 6.59139 6.6136;
6.42359 6.91248 7.26179;
6.64784 7.11565 7.43536;
7.07342 7.4352  7.64665
];
% Solutions
% Calculations
for i=1:length(phi)
    r(i,:)=[h(2)/h(1); h(3)/h(2)]; % Refinement factor
```

```

epsilon(i,:)=[phi(i,2)-phi(i,1);phi(i,3)-phi(i,2)]; % Difference between solutions
p_old=-2; % Initial guess for order of method
while i>0
    s=1*sign(epsilon(i,2)/epsilon(i,1));
    q=log((r(i,1)^p_old-s)/(r(i,2)^p_old-s));
    p(i)=abs(log(epsilon(i,2)/epsilon(i,1))+q)/log(r(i,1)); % Order of method
    if abs(p(i)-p_old)<=1E-5 % Convergence criteria
        phi_ext(i,1)=(r(i,1)^p(i)*phi(i,1)-phi(i,2))/(r(i,1)^p(i)-1); % Extrapolated values
        phi_ext(i,2)=(r(i,2)^p(i)*phi(i,2)-phi(i,3))/(r(i,2)^p(i)-1); % Extrapolated values
        e_a(i)=abs((phi(i,1)-phi(i,2))/phi(i,1));% Approximate relative error
        e_ext(i)=abs((phi_ext(i,1)-phi(i,1))/phi_ext(i,1));% Extrapolated relative error
        gci(i)=(1.25*e_a(i))/(r(i,1)^p(i)-1);
        break
    else
        p_old=p_old+1E-6; % Update initial guess for p
    end
end

```